Investigation of Structural Stability and Phase Transition behavior of Uranium based Compounds under Pressure

by

Balmukund Shukla

Enrolment No: PHY-02-2012-04017

Indira Gandhi Centre for Atomic Research,

Kalpakkam, India

A thesis submitted to the

Board of Studies in Physical Sciences

In partial fulfillment of requirements

for the Degree of

DOCTOR OF PHILOSOPHY
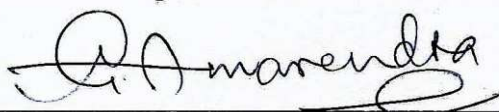
of

HOMI BHABHA NATIONAL INSTITUTE

November, 2017

Homi Bhabha National Institute[1]

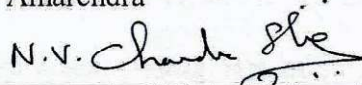## Recommendations of the Viva Voce Committee

As members of the Viva Voce Committee, we certify that we have read the dissertation prepared by Balmukund Shukla entitled "Compressibility Study of Uranium Intermetallics and Oxides" and recommend that it may be accepted as fulfilling the thesis requirement for the award of Degree of Doctor of Philosophy.

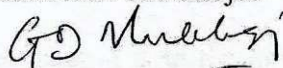Chairman – Dr. G. Amarendra   Date: May 18, 2018
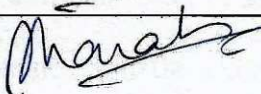
Guide / Convener - Dr. N.V. Chandra Shekar   Date: 18|5|18

Examiner – Dr. Goutam Dev Mukherjee   Date: 18/5/2018

Member 1- Dr. Sharat Chandra   Date: 18|5|2018

Member 2- Dr. A. K. Sinha   Date: 18|5|18

for N.V. Chandra Shekar
(Dean A)

Final approval and acceptance of this thesis is contingent upon the candidate's submission of the final copies of the thesis to HBNI.

I/We hereby certify that I/we have read this thesis prepared under my/our direction and recommend that it may be accepted as fulfilling the thesis requirement.

Date: 18|5|18

Place: Kalpakkam

N.V. Chandra Shekar

Guide

---

[1] This page is to be included only for final submission after successful completion of viva voce.

ACKNOWLEDGEMENTS

Dedicated to my parents

"Sri Vishnu Prasad Shukla"

&

"Smt. Phool Mati Devi"

List of Publications arising from the thesis

Journal

1. "Phase Transitions and Structural Stability of Binary Uranium Intermetallics Under High Pressure: A Review", N. V. Chandra Shekar, V. Kathirvel, **Balmukund Shukla**, P. Ch. Sahu, *Proc. Natl. Acad. Sci., India, Sect. A Phys.Sci.*, **2012**, *82*, 163-177

2. "A novel Micro-Focus High Pressure High Temperature X-ray Diffraction Technique", **Balmukund Shukla**, N. R. Sanjay Kumar, M. Sekar, N. V. Chandra Shekar, *J. Instrum. Soc. India*, **2016**, *46*, 75-77

3. "Compressibility study of UIr_2", **Balmukund Shukla**, N.R. Sanjay Kumar, Sharat Chandra, N.V. Chandra Shekar, A.K. Sinha, Anuj Upadhyay, M.N. Singh, *Intermetallics.*, **2016**, *83*, 110-114

4. "Structural stability of URh_3 at high pressure", **Balmukund Shukla**, V. Kathirvel, N.V. Chandra Shekar, S. Chandra, P.Ch. Sahu, *Physica B*, **2013**, *413*, 64–68

5. "Stability of Dy_6UO_{12} under high pressure and high temperature", **Balmukund Shukla**, N.R. Sanjay Kumar, M. Sekar, N.V. Chandra Shekar, H. Jena, R. Asuvathraman, *J. of Alloy and Compds.*, **2016**, *672*, 393-396

Conferences

1. "Twin chamber sample assembly in DAC and HPHT studies on GaN nano-particles", **Balmukund Shukla**, N. V. Chandra Shekar, N. R. Sanjay Kumar, T. R. Ravindran, P. Sahoo, S. Dhara, and P. Ch. Sahu, *J. Phys: Conf. Series*, **2012**, *377*, 012014

2. "High pressure X-ray diffraction study of URh_3", **Balmukund Shukla**, N. V. Chandra Shekar, N. R. Sanjay Kumar, and P. Ch Sahu, *AIP Conf. Proc.*, **2012**, *1447*,111

3. "Compressibility study of RE_6UO_{12} at elevated Pressure and temperature", **Balmukund Shukla**, N. R. Sanjay Kumar, N. V. Chandra Shekar, H. Jena, S. Kalavathi, NCTP Conference (2017)

Balmukund Shukla

DECLARATION

I, hereby declare that the investigation presented in the thesis has been carried out by me. The work is original and has not been submitted earlier as a whole or in part for a degree/diploma at this or any other Institution / University.

Balmukund Shukla

STATEMENT BY AUTHOR

This dissertation has been submitted in partial fulfillment of requirements for an advanced degree at Homi Bhabha National Institute (HBNI) and is deposited in the Library to be made available to borrowers under rules of the HBNI.

Brief quotations from this dissertation are allowable without special permission, provided that accurate acknowledgment of source is made. Requests for permission for extended quotation from or reproduction of this manuscript in whole or in part may be granted by the Competent Authority of HBNI when in his or her judgment the proposed use of the material is in the interests of scholarship. In all other instances, however, permission must be obtained from the author.

Balmukund Shukla

TABLE OF CONTENTS

(Metallurgical Society of AIME, New York, 1970).

[7]   D. D. Koelling, B. D. Dunlap, and G. W. Crabtree, Phys. Rev. B **31**, 4966 (1985).

[8]   T. Oguchi and A. J. Freeman, J. Magn. Magn. Mater. **61**, 233 (1986).

[9]   H. G. Diehl and C. Keller, J. Solid State Chem. **3**, 621 (1971).

[10]   E. A. Aitken, S. F. Bartram, and E. F. Juenke, Inorg. Chem. **3**, 949 (1964).

[11]   M. Zinkevich, Prog. Mater. Sci. **52**, 597 (2007).

[12]   B. Shukla, N. R. Sanjay Kumar, M. Sekar, and N. V. Chandra Shekar, J. Instrumentation Soc. India **46**, 75 (2016).

[13]   N. Subramanian, N. V. Chandra Shekar, N. R. Sanjay Kumar, and P. C. Sahu, Curr. Sci. **91**, 175 (2006).

[14]   B. Shukla, N. R. Sanjay Kumar, S. Chandra, N. V. Chandra Shekar, A. K. Sinha, A. Upadhyay, and M. N. Singh, Intermetallics **83**, 110 (2017).

[15]   B. Shukla, V. Kathirvel, N. V. Chandra Shekar, S. Chandra, and P. C. Sahu, Phys. B Condens. Matter **413**, 64 (2013).

[16]   B. Shukla, N. R. Sanjay Kumar, M. Sekar, N. V. Chandra Shekar, H. Jena, and R. Asuvathraman, J. Alloys Compd. **672**, 393 (2016).

[17]   R. Venkata Krishnan, R. Babu, G. Panneerselvam, K. Ananthasivan, M. P. Antony, and K. Nagarajan, Ceram. Int. **38**, 5277 (2012).

UX$_2$ type compounds such as UOs$_2$, UIr$_2$ resembling with MgCu$_2$ type structure and UZr$_2$ having AlB$_2$ type structure has been studied under high pressure. UOs$_2$ and UIr$_2$ have been found to under phase transition to probable hexagonal and tetragonal structures. DFT computation is required for UOs$_2$ to find out the reason for the phase transition at very low pressures. HP study on UZr$_2$ shows the stability of the compounds up to the highest pressure studied.

HP studies on URh$_3$ and UIr$_3$ are stable up to 25GPa but shows a large difference in their bulk modulus.

Among rare-earth uranates, the anomalous behavior of Gd$_6$UO$_{12}$ has been ascribed to the localization of the 4-f electrons of gadolinium. For the first time, Pressure-Induced Amorphization have been seen in such systems which is caused by anions followed by cations.

References:

[1] J. Hafner, F. Hulliger, W. B. Jensen, J. A. Majewski, and K. Mathis, *The Structures of Binary Compounds* (1989).

[2] J. P. Itié, J. Staun Olsen, L. Gerward, U. Benedict, and J. C. Spirlet, Phys. B+C **139–140**, 330 (1986).

[3] A. P. Gonçalves, M. S. Henriques, J. C. Waerenborgh, L. C. J. Pereira, E. B. Lopes, M. Almeida, S. Mašková, L. Havela, A. Shick, Z. Arnold, D. Berthebaud, O. Tougait, and H. Noël, IOP Conf. Ser. Mater. Sci. Eng. **9**, 12090 (2010).

[4] N. V. Chandra Shekar and P. C. Sahu, J. Mater. Sci. **41**, 3207 (2006).

[5] N. V. Chandra Shekar, P. C. Sahu, V. Kathirvel, and S. Chandra, Indian J. Phys. **86**, 971 (2012).

[6] H. H. Hill., *Plutonium 1970 and Other Actinides, W.N. Miner, Ed.,*

are estimated to be 157.7 GPa, 134.1 GPa, and 144 GPa respectively. An abrupt softening in Gd_6UO_{12} has been observed which can be ascribed to the localization of 4-f electrons of Gd. As the pressure is increased the peaks broaden due to the anion (oxygen) disorder. With increasing pressure cations (RE^{3+}) also starts moving leading to increase in the (300) peak intensity and sharp decrease in the (211) and (122) intensity simultaneously. The movement of cation leads to a possible unknown high-pressure disorder phase. At very high pressures the compound is found to amorphize when both the anion and cation disorder appear simultaneously. For the first-time pressure-induced amorphization has been seen in rare earth uranates. It is seen that disorder in the system originates at lower pressure in more compressible system.

HP-HT studies were carried out on RE_6UO_{12} (RE=Sm, Gd, Dy) and the materials were found to be stable in rhombohedral structure up to (5.6 GPa, 673 K) for Sm_6UO_{12}, (5.0 GPa, 673 K) for Gd_6UO_{12} and (11.3 GPa, 673 K) for Dy_6UO_{12}. Bulk modulus at various temperatures was estimated and all the compounds are found to be more compressible at high temperature rendering the usual character under temperature. However, more softening is seen in Gd_6UO_{12} as compared to other RE_6UO_{12} (RE=Sm, Dy) in the same temperature range. Gd_6UO_{12} has the largest volume thermal expansion coefficient at ambient pressure because of its weaker bonding in the lattice and a large drop in the thermal expansion coefficient was observed at 1 GPa. However, Sm_6UO_{12} and Dy_6UO_{12} don't show any such sharp change and their thermal expansion coefficient fall linearly with respect to pressure.

Chapter 7. Summary and Future Directions

A novel twin chamber technique for laser-heated diamond anvil cell has been developed. A unique micro-XRD (Laboratory based 50 W X-ray generator) based HP-HT technique has been demonstrated and used for various studies.

decrease in the thermal expansion coefficient is observed which are 4.6×10^{-5} K^{-1}, 3.7×10^{-5} K^{-1}, 2.7×10^{-5} K^{-1} at 1.2 GPa, 4.8 GPa and 6.6 GPa respectively in the temperature range 300 K-473 K.

Chapter 5: High-Pressure Structural Stability of UX$_3$ (X=Rh, Ir) Compounds

High-Pressure experiments on UX$_3$ (X= Rh, Ir) type compounds were performed up to 25 GPa and the material is found to be stable up to the highest pressure studied [15]. For URh$_3$, the high-pressure structural stability has also been proved using electronic structural calculation up to 40 GPa. Beyond 40 GPa, 2-D structural stability map predicts a possible Ni$_3$Sn type structure in URh$_3$. However, total energy vs equilibrium volume for the cubic AuCu$_3$ and hexagonal Ni$_3$Sn type structures do not intersect up to 360 GPa thereby predicting a large structural stability of ambient cubic phase in URh$_3$.

Using pressure-volume data the bulk modulus of the compounds URh$_3$ and UIr$_3$ were estimated to be 133.0 GPa and 262.5 GPa respectively. A large difference in the bulk modulus of the similar compounds is very surprising. The reason for such a drastic increase in the bulk modulus can be attributed to the increased hybridization between uranium site and iridium site in UIr$_3$. Also, U-f states participation in the total density of state are found to be 61.3% more in UIr$_3$ at Fermi level as compared with URh$_3$ [8]. Therefore, U-f states are solely responsible for such a large change in compressibility of the compound.

Chapter 6: Studies on Rare-Earth Uranates at HP & HP-HT

Synchrotron HPXRD study on Sm$_6$UO$_{12}$, Gd$_6$UO$_{12}$, and Dy$_6$UO$_{12}$ at ambient temperature reveal that the compounds are stable at lower pressures. a-axis of the lattice is found to be more rigid as compared to c-axis under pressure because of it corner sharing polyhedra along a-axis [16], however, temperature studies suggest c-axis to be more rigid [17]. The bulk modulus of the compound Sm$_6$UO$_{12}$, Gd$_6$UO$_{12}$ and Dy$_6$UO$_{12}$

parameter a = 6.460 Å and c = 10.313 Å. Computation reveals that the iridium tetrahedral network in the lattice to be more stable because of short Ir-Ir bonds. However, U-Ir has mixed metallic and covalent nature of bonding. Therefore, application of pressure directly affects uranium tetrahedra. The distortions in uranium tetrahedra are responsible for the observed phase transition. Total density of state plot shows a dip at Fermi energy. Origin of pseudogap in the calculated DOS indicates new structure to be more favorable and stable at higher pressures.

High-pressure study on UOs_2 up to 35.5 GPa reveals the compound to be stable up to 12 GPa. The bulk modulus of the compound is estimated to be 261 GPa. A structural phase transition has been observed between 12.0 GPa and 20.1 GPa wherein the compound transforms to the hexagonal structure with one formula unit in the cell. The bulk modulus of the high-pressure phase has been found to be 365.7 GPa which is the highest bulk modulus known till now, among all the UX_2 type compounds.

Rietveld refinement on the powdered UZr_2 at ambient pressure and temperature gives the occupancy factor of Zr at positions (1/3,2/3,1/2) (2/3,1/3,1/2) to be 0.84. High-pressure study at ambient temperature on δ-UZr_2 reveals that δ phase of UZr_2 is stable up to 20.0 GPa. Up to a pressure of 10 GPa, the c/a ratio was found to decrease slowly, after which a reduction rate increases sharply. It may be attributed to the strengthening of U(1/3,2/3,1,2)→ Zr(2/3,1/3,1,2) covalent bond, which is along the 'a' axis, at higher pressures. The localization of charge density leads to the drop in the metallization of the material which can be clearly seen from the charge density plots.

High-pressure and high-temperature study on UZr_2 shows that material is stable up to 6 GPa and 473 K simultaneously. The bulk modulus of 101.6 GPa at 473 K indicates a softening in the material at high temperature. Both the 'a' and 'c' axes decrease with pressure at high temperature, however, c/a is found to increase. A usual

6

Chapter 3: Development of Experimental Facilities

This chapter consists of four Sections dealing with the development of novel experimental techniques. First Section deals with the development of electric discharge machine for drilling holes of various sizes ranging from 70 μm to 300 μm in stainless steel and rhenium gaskets. Second Section consists of the development of a novel twin chamber Laser-Heated Diamond Anvil Cell (LHDAC) experimental technique which is useful in high pressure and high-temperature experiments. Third Section describes a novel combination of high flux micro-focus x-ray generator and Helios membrane Diamond Anvil Cell (DAC) for carrying out HP-HT experiments. Using this unique set up we have carried out several HP-HT experiments which will be discussed in the subsequent chapters. Fourth Section comprises of an indigenous development of a resistive heater for the membrane cell DAC. The motivation to develop an indigenous heater was an effort to make it cost effective and maneuverable to access and control.

Chapter 4: Compressibility Study of UX_2 (X= Ir, Os & Zr) Type Compounds

With the aim to find out the high bulk modulus compound among binary uranium intermetallics and study their structural properties under pressure and temperature, UOs_2 and UIr_2 have been studied. UZr_2, an AlB_2 type UX_2 compound, exhibits ω phase at ambient. Therefore, its 5-f characteristics becomes important at HP-HT from the physics and nuclear industry point of view.

High-pressure experiment on UOs_2, UIr_2 and UZr_2 have been carried out up to 35.5 GPa, 55 GPa, and 20 GPa respectively. The bulk modulus of the compounds are found to be 261GPa, 284 GPa, and 108.3 GPa at ambient pressure respectively.

In UIr_2 uranium 5-f electrons are participating in the bonding, giving rise to higher bulk modulus [14]. At 40 GPa several new peaks appear indicating a phase transition. The high-pressure phase is found to have a tetragonal lattice with lattice

thermophysical properties with temperature, therefore, their properties under high pressure are expected to be interesting for understanding the role of *f*-electrons in such ionic compounds. However, such studies are not available in the literature and the role of uranium in the compound is not properly understood. In the present thesis, we report *in-situ* HP& (HP-HT) structural stability studies on Rare-Earth Uranates (RE=Sm, Gd, Dy).

Chapter 2: Experimental and computational techniques

This chapter describes the sample preparation methods, description of the equipment used, experimental techniques and procedures used for carrying out in-situ High Pressure-High Temperature X-ray diffraction experiment. Uranium intermetallic samples were prepared using vacuum arc-melting techniques and further annealed using a high-temperature furnace in an inert atmosphere, however, rare-earth uranates were prepared using sol-gel urea combustion method.

Mao-Bell type Diamond Anvil Cell (DAC), designed and fabricated at IGCAR, has been used to achieve static high pressure. Laboratory-based and synchrotron x-ray sources have been employed for high-pressure XRD studies. The pressure inside the DAC has been measured using Ruby fluorescence/EOS techniques. HP-HT studies have been carried out using Diacell Helios Membrane DAC wherein pressure and temperature were estimated using NaCl peaks and a thermocouple respectively [12]. Laser heated diamond anvil cell facility, developed at IGCAR [13], has been employed to heat the sample in one of the SS gasket chamber in DAC to carry out a novel twin chamber experiment.

The chapter also describes the various computational techniques used to perform the density functional theory computations.

4

structure) [1]. *nu2* type AlB_2 structure resembles the omega (ω) phase (ideal *c/a*=0.612) which have improved mechanical properties, and hence become technologically important. One of the AlB_2 type compound, δ-UZr_2 is studied in this thesis whose structure is akin to the ω structure at ambient pressure and temperature.

AX_3 (A=rare-earth, X=*p* or *d* block element) compounds stabilize in $AuCu_3$ type Laves cubic structure and very few studies are available for such compounds. Hill developed successful criteria for deciding the nature of *f*-electrons through the mechanism of actinide-actinide separation [6]. However, there are few exceptions to the Hill limit criteria e.g. UIr_3, URh_3, UGe_3 etc. which were further attributed to the U-X distance and character of the hybridization between *f* and *d* (non-actinide site) orbital [7]. This study experimentally supports the theoretically predicated trend in UX_3 type compounds with isoelectronic pairs (same column X element in the periodic table) like URh_3 - UIr_3. These compounds have $4d$ and $5d$ orbitals in Rh and Ir respectively. The $5d$ band has more width as compared to the $4f$ band in the same column. Therefore, the hybridization between U-*f* and X-$5d$ orbitals is more than the respective X-$4d$ orbitals [8].

Additionally, uranium rare earth (RE) oxides - RE_6UO_{12} compounds are found to exist in the rhombohedral structure at ambient [9,10]. The high-temperature XRD studies show positive thermal expansion coefficient for all RE_6UO_{12} (RE: La, Gd, Nd, Sm, Eu, Tb, and Dy). A general trend of decrease in the thermal expansion coefficient is seen as a function of cation's (RE^{3+}) atomic number which it is due to the smaller unit cell size of the lattice from La to Dy. However, Gd_6UO_{12} shows an exception in the RE_6UO_{12} series and displays anomalous behavior in thermal expansion coefficients. In rare-rarth sesquioxides, the anomalous behavior was ascribed to the half-filled 4f states [11]. As these rare-earth uranates show very interesting changes in their

3

compounds and there are large number of compounds which are not yet studied under high pressure.

This thesis deals with the investigation of the effect of pressure and temperature on the structural stability and phase transition behavior of Uranium based intermetallics & oxides. The correlations with their electronic structure have also been carried out wherever necessary. The work described in the thesis is briefly outlined here.

Chapter 1: Introduction

Most of the AX_2 type compounds are found to stabilize in $MgCu_2$ type Laves phase (UX_2, X=Fe, Co, Ir, Os; AX_2, A=rare earth and X=Ru, Os, Fe, Co, Ni etc.) at ambient because of very low electronegativity value, Zunger pseudo potential radii and higher valence electron. It shows that the $MgCu_2$ type structure is stable over a large range of band electrons in such compounds. The main factors contributing to the stability of the Laves phases (including $MgZn_2$ and $MgNi_2$ phase) is geometrical in origin [1]. Also, the stability of $MgCu_2$ type Laves phase compounds have been established theoretically using Density Functional Theory DFT calculations and also confirmed experimentally [2,3]. However, at very high pressure the following structural sequence for UX_2 compounds is observed and established: Laves phase $\rightarrow$ $MoSi_2$ type (Tetragonal) $\rightarrow$ $CeCd_2$ type (hexagonal) $\rightarrow$ $CeCu_2$ type (orthorhombic) $\rightarrow$ $CaIn_2$ type (hexagonal) $\rightarrow$ AlB_2 type (hexagonal) $\rightarrow$ $ZrSi_2$ type (orthorhombic) $\rightarrow$ $ThSi_2$ type (tetragonal) $\rightarrow$ $SmSb_2$ type (orthorhombic) $\rightarrow$ Cu_2Sb type (tetragonal) [4].

Some of the AX_2 type compounds e.g. rare-earth digallides, UZr_2 etc., exhibit AlB_2 type structure at ambient and show a variety of phase transitions due to Fermi energy positioned very close to the *f-d* hybridized peak in DOS vs Energy plot [5]. There are two kinds of AlB_2 type structures which are characterized according to their *c/a* ratio, one with *c/a*=0.95-1.27 (*kz1* structure) another one with *c/a*=0.59-0.88 (*nu2*

SYNOPSIS

Uranium intermetallic compounds (IMC) are important from the point of view of future metallic fuel reactors while oxides of uranium and rare earth elements are either used as a neutron poison in the fuel matrix or formed during the operation of a nuclear reactor. Also, due to the nature of f-electrons, these compounds often show exotic and anomalous properties which are interesting from the view of fundamental understanding. Localization and itinerancy of the 5-f electrons play very important role in deciding the properties of these materials. Localized electrons show local magnetism, however, itinerant 5-f electrons participate in the bonding leading to a stronger material. To systemize and generalize the nature of actinide compounds several approaches such as Hill criteria, Mott-Hubbard criterion, empirical methods like Ratio of radii- $R_{(RE\ or\ An)}/R_B$ of two atoms for binary compounds and number of free electrons per atom (e/a) have been proposed. Pressure is one of the important parameters which can bring several changes in the material, like structural phase transitions, broadening of the bandwidths, modification, and shifting of the Fermi surface. These alterations modify the role of the f-electrons, thence, the characteristics of the material property. Therefore, the study of uranium intermetallics under high pressure becomes important. Binary f-IMCs are the A_mX_n type compounds where A belongs to rare earth or actinide and X belong to p or d block metal. The nature of the bonding in these compounds are mostly metallic. Among all the A_mX_n compounds, AX type compounds have been studied to a large extent after several decades of intensive research and a systematic trend for their high-pressure behavior have emerged. In spite of all the studies in uranium binary compounds no clear systematics have been observed in AX_2 and AX_3 type intermetallic

1

List of Tables

13

12

List of Figures

[98] U. Berndt, R. Tanamas, and C. Keller, J. Solid State Chem. **17**, 113 (1976).

[99] H. G. Diehl and C. Keller, J. Solid State Chem. **3**, 621 (1971).

[100] E. A. Aitken, S. F. Bartram, and E. F. Juenke, Inorg. Chem. **3**, 949 (1964).

[101] H. Jena, R. Asuvathraman, and K. V. Govindan Kutty, J. Nucl. Mater. **280**, 312 (2000).

[102] R. V. Krishnan, P. Manikandan, H. Jena, and K. Nagarajan, Thermochim. Acta **472**, 95 (2008).

[103] R. Venkata Krishnan, H. Jena, K. V. Govindan Kutty, and K. Nagarajan, J. Therm. Anal. Calorim. **101**, 371 (2010).

[104] H. Jena, R. Asuvathraman, M. V. Krishnaiah, and K. V. G. Kutty, Powder Diffr. **16**, 220 (2001).

[105] R. Venkata Krishnan, R. Babu, G. Panneerselvam, K. Ananthasivan, M. P. Antony, and K. Nagarajan, Ceram. Int. **38**, 5277 (2012).

[106] I. Barin, editor , *Thermochemical Data of Pure Substances* (Wiley-VCH Verlag GmbH, Weinheim, Germany, 1995).

[107] D. Taylor, Trans. Br. Ceram. Soc. **83**, 92 (1984).

[108] H. Lehmann, D. Pitzer, G. Pracht, R. Vassen, and D. Stöver, J. Am. Ceram. Soc. **86**, 1338 (2003).

Int. J. Mod. Phys. B **25**, 551 (2011).

[86] V. Kathirvel, S. Chandra, N. V. Chandra Shekar, P. C. Sahu, and S. M. Babu, J. Phys. Conf. Ser. **215**, 12115 (2010).

[87] B. Shukla, V. Kathirvel, N. V. Chandra Shekar, S. Chandra, and P. C. Sahu, Phys. B Condens. Matter **413**, 64 (2013).

[88] P. Villars, J. Less Common Met. **99**, 33 (1984).

[89] P. Villars, J. Less Common Met. **109**, 93 (1985).

[90] P. Villars, J. Less Common Met. **102**, 199 (1984).

[91] P. Villars, J. Less Common Met. **110**, 11 (1985).

[92] M. C. Zhang Shichao, Qiu Xueliang, *Impacts of Electricity Market Reforms on the Choice of Nuclear and Other Generation Technologies.* (International Atomic Energy Agency, 2016).

[93] Y. Hinatsu, N. Masaki, and T. Fujino, J. Solid State Chem. **73**, 567 (1988).

[94] P. C. Sahu, D. Lonappan, and N. V Chandra Shekar, J. Phys. Conf. Ser. **377**, 12015 (2012).

[95] M. Zinkevich, Prog. Mater. Sci. **52**, 597 (2007).

[96] M. Sahu, K. Krishnan, M. Saxena, and K. Ramakumar, J. Alloys Compd. **482**, 141 (2009).

[97] M. Sahu, K. Krishnan, M. K. Saxena, and S. Dash, J. Therm. Anal. Calorim. **112**, 165 (2013).

[72] V. E. Antonov, M. Baier, B. Dorner, A. Breidi, M. Andasmas, J. C. Crivello, O. Degtyareva, V. F. Degtyareva, M. Christensen, W. Wolf, C. Freeman, M. Akabori, T. Ogawa, A. Itoh, and Y. Morii, J. Phys. Condens. Matter **7**, 8249 (1995).

[73] B. S. Hickman, J. Mater. Sci. **4**, 554 (1969).

[74] Y. K. Vohra, S. K. Sikka, and R. Chidambaram, J. Phys. F Met. Phys. **9**, 1771 (2001).

[75] S. K. Sikka, Y. K. Vohra, and R. Chidambaram, Prog. Mater. Sci. **27**, 245 (1982).

[76] H. Xia, A. L. Ruoff, and Y. K. Vohra, Phys. Rev. B **44**, 10374 (1991).

[77] E. R. Boyko, Acta Crystallogr. **10**, 712 (1957).

[78] A. N. Holden and W. E. Seymour, J. Met. **9**, 521 (1956).

[79] M. Akabori, T. Ogawa, A. Itoh, and Y. Morii, J. Phys. Condens. Matter **7**, 8249 (1995).

[80] D. D. Koelling, B. D. Dunlap, and G. W. Crabtree, Phys. Rev. B **31**, 4966 (1985).

[81] G. R. Stewart, Rev. Mod. Phys. **56**, 755 (1984).

[82] T. Oguchi and A. J. Freeman, J. Magn. Magn. Mater. **61**, 233 (1986).

[83] N. V. Chandra Shekar, P. C. Sahu, M. Rajagopalan, and M. Yousuf, J. Phys. Condens. Matter **9**, 5867 (1997).

[84] U. Benedict, S. Dabos, L. Gerward, J. S. Olsen, J. Beuers, J. C. Spirlet, and C. Dufour, J. Magn. Magn. Mater. **63–64**, 403 (1987).

[85] V. Kathirvel, S. Chandra, N. V. Chandra Shekar, P. C. Sahu, and M. Rajagopalan,

104–107, 697 (1992).

[60] T. Nishioka, K. Kimura, H. Matsui, and M. Kontani, J. Phys. Soc. Japan **63**, 2722 (1994).

[61] J. F. Cannon, D. L. Robertson, H. T. Hall, and A. C. Lawson, J. Less Common Met. **31**, 174 (1973).

[62] A. E. Dwight, Trans. Amer. Soc. Met. **53**, 479 (1961).

[63] N. V. Chandra Shekar, P. C. Sahu, V. Kathirvel, and S. Chandra, Indian J. Phys. **86**, 971 (2012).

[64] K. Devan, A. Bachchan, A. Riyas, T. Sathiyasheela, P. Mohanakrishnan, and S. C. Chetal, Nucl. Eng. Des. **241**, 3058 (2011).

[65] T. Ogawa, T. Iwai, and M. Kurata, J. Less-Common Met. **175**, 59 (1991).

[66] A. Landa, P. Söderlind, and P. E. A. Turchi, J. Alloys Compd. **478**, 103 (2009).

[67] C. B. Basak, N. Prabhu, and M. Krishnan, Intermetallics **18**, 1707 (2010).

[68] M. Akabori, A. Itoh, T. Ogawa, F. Kobayashi, and Y. Suzuki, J. Nucl. Mater. **188**, 249 (1992).

[69] J. T. Mckeown, S. Irukuvarghula, S. Ahn, M. Wall, L. L. Hsiung, S. Mcdeavitt, and P. E. A. Turchi, J. Nucl. Mater. **436**, 100 (2013).

[70] T. Ogawa, J. K. Gibson, R. G. Haire, M. M. Gensini, and M. Akabori, J. Nucl. Mater. **223**, 67 (1995).

[71] H. Xia, S. J. Duclos, A. L. Ruoff, and Y. K. Vohra, Phys. Rev. Lett. **64**, 204 (1990).

Berlin, Heidelberg, 1985), pp. 127–196.

[49] N. V. Chandra Shekar, P. C. Sahu, N. R. Sanjay Kumar, M. Sekar, N. Subramanian, V. Kathirvel, S. Chandra, and M. Rajagopalan, Solid State Phenom. **150**, 123 (2009).

[50] U. Benedict and W. B. Holzapfel, in *Handb. Phys. Chem. Rare Earths, Vol 17* (1993), p. 245.

[51] P. Villars, J. Less-Common Met. **92**, 215 (1983).

[52] J. Hafner, F. Hulliger, W. B. Jensen, J. A. Majewski, and K. Mathis, *The Structures of Binary Compounds* (1989).

[53] F. Laves and H. White, Met. Met. Met. **15**, 840 (1936).

[54] R. P. Elliot and W. Rostoker, Trans. Am. Soc. Met **50**, 617 (1958).

[55] B. Shukla, N. R. Sanjay Kumar, S. Chandra, N. V. Chandra Shekar, A. K. Sinha, A. Upadhyay, and M. N. Singh, Intermetallics **83**, 110 (2017).

[56] J. P. Itié, J. Staun Olsen, L. Gerward, U. Benedict, and J. C. Spirlet, Phys. B+C **139–140**, 330 (1986).

[57] M. Rajagopalan, N. V. Chandra Shekar, and P. C. Sahu, Philos. Mag. Lett. **85**, 27 (2005).

[58] A. P. Gonçalves, M. S. Henriques, J. C. Waerenborgh, L. C. J. Pereira, E. B. Lopes, M. Almeida, S. Mašková, L. Havela, A. Shick, Z. Arnold, D. Berthebaud, O. Tougait, and H. Noël, IOP Conf. Ser. Mater. Sci. Eng. **9**, 12090 (2010).

[59] S. A. M. Mentink, G. J. Nieuwenhuys, and J. A. Mydosh, J. Magn. Magn. Mater.

New York, 1970), p. 2.

[37]   M. S. Henriques, O. Tougait, H. Noel, L. C. J. Pereira, J. C. Waerenborgh, A. P. Gonçalves, and F. De La Cruz, Solid State Commun. **148**, 159 (2008).

[38]   M. J. Winiarski, J.-C. Griveau, E. Colineau, K. Wochowski, P. Wiśniewski, D. Kaczorowski, R. Caciuffo, and T. Klimczuk, J. Alloys Compd. **696**, 1113 (2017).

[39]   N. V. Chandra Shekar, V. Kathirvel, B. Shukla, and P. C. Sahu, Proc. Natl. Acad. Sci. India Sect. A - Phys. Sci. **82**, 163 (2012).

[40]   J. Hubbard, Proc. R. Soc. A Math. Phys. Eng. Sci. **281**, 401 (1964).

[41]   B. Johansson, Phys. Rev. B **11**, 2740 (1975).

[42]   L. Manes, *Actinides — Chemistry and Physical Properties* (Springer Berlin Heidelberg, 1985).

[43]   P. C. Sahu and N. V. Chandra Shekar, Pramana - J. Phys. **54**, 685 (2000).

[44]   A. Lindbaum, S. Heathman, T. Le Bihan, R. G. Haire, M. Idiri, and G. H. Lander, J. Phys. Condens. Matter **15**, S2297 (2003).

[45]   Y. Komura, K. Tokunaga, and IUCr, Acta Crystallogr. Sect. B Struct. Crystallogr. Cryst. Chem. **36**, 1548 (1980).

[46]   A. Ślebarski, J. Magn. Magn. Mater. **66**, 107 (1987).

[47]   R. M. White, *Quantum Theory of Magnetism : Magnetic Properties of Materials* (Springer, 2007).

[48]   J. M. Fournier, in *Actinides — Chem. Phys. Prop.* (Springer Berlin Heidelberg,

32 (2007).

[27] D. L. Decker, J. Appl. Phys. **42**, 3239 (1971).

[28] B. Shukla, N. R. Sanjay Kumar, M. Sekar, N. V. Chandra Shekar, H. Jena, and R. Asuvathraman, J. Alloys Compd. **672**, 393 (2016).

[29] T. Tsuchiya and K. Kawamura, Phys. Rev. B **66**, 94115 (2002).

[30] E. Guziewicz, T. Durakiewicz, M. T. Butterfield, C. G. Olson, J. J. Joyce, A. J. Arko, J. L. Sarrao, D. P. Moore, and L. Morales, Phys. Rev. B **69**, 45102 (2004).

[31] T. Durakiewicz, C. D. Batista, J. D. Thompson, C. G. Olson, J. J. Joyce, G. H. Lander, J. E. Gubernatis, E. Guziewicz, M. T. Butterfield, A. J. Arko, J. Bonča, K. Mattenberger, and O. Vogt, Phys. Rev. Lett. **93**, 267205 (2004).

[32] J. J. Joyce, J. M. Wills, T. Durakiewicz, M. T. Butterfield, E. Guziewicz, J. L. Sarrao, L. A. Morales, A. J. Arko, and O. Eriksson, Phys. Rev. Lett. **91**, 176401 (2003).

[33] J. M. Wills, O. Eriksson, A. Delin, P. H. Andersson, J. J. Joyce, T. Durakiewicz, M. T. Butterfield, A. J. Arko, D. P. Moore, and L. A. Morales, J. Electron Spectros. Relat. Phenomena **135**, 163 (2004).

[34] T. Durakiewicz, J. J. Joyce, J. M. Wills, and C. D. Batista, J. Phys. Soc. Japan **75**, 39 (2006).

[35] G. Zwicknagl, Int. J. Mod. Phys. B **21**, 2232 (2007).

[36] H. H. Hill, in *Plutonium 1970 Other Actinides, W.N. Miner, ed.,The Metall. Soc. AIME, New York*, edited by Miner and W. N. (ed.) (Metallurgical Society of AIME,

[13] A. P. Wilkinson, B. K. Greve, C. J. Ruschman, K. W. Chapman, and P. J. Chupas, J. Appl. Phys. **112**, (2012).

[14] D. R. Rittman, K. M. Turner, S. Park, A. F. Fuentes, J. Yan, R. C. Ewing, and W. L. Mao, J. Appl. Phys. **121**, 45902 (2017).

[15] F. X. Zhang, M. Lang, Z. Liu, and R. C. Ewing, Phys. Rev. Lett. **105**, 15503 (2010).

[16] H. Li, N. Li, Y. Li, Q. Tao, Y. Zhao, H. Zhu, Y. Ma, P. Zhu, and X. Wang, High Press. Res. **37**, 256 (2017).

[17] Q. Williams, E. Knittle, R. Reichlin, S. Martin, and R. Jeanloz, J. Geophys. Res. **95**, 21549 (1990).

[18] M. Imada, A. Fujimori, and Y. Tokura, Rev. Mod. Phys. **70**, 1039 (1998).

[19] W. M. Temmerman, A. Svane, L. Petit, M. Lüders, P. Strange, and Z. Szotek, Phase Transitions **80**, 415 (2007).

[20] B. K. Godwal, S. Meenakshi, P. Modak, R. S. Rao, S. K. Sikka, V. Vijayakumar, E. Bussetto, and A. Lausi, Phys. Rev. B **65**, 140101 (2002).

[21] O. L. Anderson, Oxford Monogr. Geol. Geophys. **31**, 405 (1995).

[22] M. Matsui and Masanori, J. Phys. Conf. Ser. **215**, 12197 (2010).

[23] F. Birch, Phys. Rev. **71**, 809 (1947).

[24] P. Vinet, J. R. Smith, J. Ferrante, and J. H. Rose, Phys. Rev. B **35**, 1945 (1987).

[25] R. S. Chauhan and C. P. Singh, Phys. B Condens. Matter **387**, 352 (2007).

[26] K. Vinod, V. S. Malik, S. K. Sharma, and S. K. Srivastava, J. Phys. Chem. Solids **68**,

References

[1]   A. Jayaraman, Rev. Mod. Phys. **55**, 65 (1983).

[2]   U. Benedict, Le J. Phys. Colloq. **45**, C8 (1984).

[3]   J. X. Boucherle, *Proceedings of the International Conference on Anomalous Rare Earths and Actinides : Valence Fluctuation and Heavy Fermions : 7-11 July 1986, Grenoble, France* (Elsevier Science, 2013).

[4]   A. Tröster, W. Schranz, F. Karsai, and P. Blaha, Phys. Rev. X **4**, 31010 (2014).

[5]   Y. Peng, F. Wang, Z. Wang, A. M. Alsayed, Z. Zhang, A. G. Yodh, and Y. Han, Nat. Mater. **14**, 101 (2014).

[6]   L. H. Brixner, Mater. Res. Bull. **7**, 879 (1972).

[7]   H. Zhu, X. Han, P. Zhu, X. Wu, Y. Chen, M. Li, X. Li, and Q. Cui, J. Phys. Chem. C **120**, 12423 (2016).

[8]   S. K. Deb, M. Wilding, M. Somayazulu, and P. F. McMillan, Nature **414**, 528 (2001).

[9]   L. Wang, X. Huang, D. Li, F. Li, Z. Zhao, W. Li, Y. Huang, G. Wu, Q. Zhou, B. Liu, and T. Cui, J. Phys. Chem. C **119**, 19312 (2015).

[10]   S. Bustingorry and E. A. Jagla, Phys. Rev. B **71**, 224119 (2005).

[11]   P. Gillet, J. Badro, B. Varrel, and P. F. McMillan, Phys. Rev. B **51**, 11262 (1995).

[12]   F. X. Zhang, J. Lian, U. Becker, R. C. Ewing, J. Hu, and S. K. Saxena, Phys. Rev. B **76**, 214104 (2007).

probe the behavior of these ionic compounds and to understand the systematic behavior of Rare-Earth uranates, they have been chosen to study in this thesis under the simultaneous application of pressure and temperature.

1.5 Motivation for the thesis

Uranium and its compounds have been under intense investigation for their usefulness to the nuclear industry. The nature of $5f$ electrons in uranium dramatically varies in various compounds as well as with external pressure and temperature. It has been a challenge for decades as to how to generate a systematic trend in uranium compounds. The nature of $5f$ electrons has been found to dictate the bonding nature in the compounds which can be altered by changing external thermodynamic parameters. This thesis is an effort to study the HP & HP-HT behavior of compounds with metallic, covalent and ionic bonding at ambient pressure.

Among all the uranium intermetallic compounds UX_2 type compounds show both the metallic and covalent character of bonding. This type of compounds are also known to show a variety of phase transitions with pressure and temperature. Therefore, UX_2 type systems with $MgCu_2$ type structure and X belonging to a group of the periodic table (X=Os, Ir), have been selected for HP study. Choice of such compounds are also motivated by the need for the least compressible materials that have been in demand for decades in various applications.

Presence of ω-phase, with enhanced mechanical properties, is of interest and importance. Therefore, UZr_2 compound with AlB_2 type structure (X=Zr) has been studied as a part of the thesis.

Rare-Earth Uranates have ionic bonding and their preferential expansion as a function of temperature have already been reported [96,103,105]. Gd_6UO_{12} has been found to have the largest thermal expansion coefficient among all the uranates. Therefore, to

axis [96,97,101,103,105]. It is attributed to lesser density of atoms along the a-axis. It is also reported that the heat capacity increases with increasing temperature [96,97,102,103,105].

As these rare-earth uranates show very interesting changes in their thermo-physical properties, their high-pressure properties are expected to bring forward hitherto unknown changes. Also, the role of uranium in the compound is not understood. In this thesis, we report *in-situ* HP & (HP-HT) structural stability studies on Rare-Earth Uranates (RE=Sm, Gd, Dy). The results of the studies are described in chapter 6.

Table 1.2 indicates the decreasing trend in lattice parameters of RE_6UO_{12} with increasing atomic number of the Rare-Earth (RE) cation. This is due to the fact that the radius of the cation decreases along lanthanides (cation) leading to the reduced unit cell size.

1.4.3 Physical properties of the compounds

High-temperature XRD studies show positive thermal expansion coefficient for all RE_6UO_{12} (RE- La, Gd, Nd, Sm, Eu, Tb, and Dy). Table 1.2 shows a general trend of decrease in the thermal expansion coefficient as a function of atomic number of the cation (RE^{3+}), again it is due to the smaller unit cell size of the lattice from La to Dy. However, Gd_6UO_{12} shows an exception in the RE_6UO_{12} series and displays an erratic behavior. The thermal expansion coefficient of the compound is found to be maximum, whereas its heat capacity is minimum in the RE cation series of RE_6UO_{12} compounds. Other rare earth oxide compounds such as RE_2O_3 (Rare-Earth Sesquioxides) [106,107] and $RE_2Zr_2O_7$ (Rare-Earth Zirconates) [108], too, show similar behavior in their physical properties e.g. thermal expansion coefficient, heat capacity. In Rare-Earth Sesquioxides, the anomalous behavior is ascribed to the half-filled $4f$ states [95]. Rare earth uranates also show the same behavior. Thermal expansion coefficient is always more along a-axis than c-axis, except, in Gd_6UO_{12}. H. Jena et $al.$ accredits the effect to the rigidity of the crystal along c-axis [105]. M Sahu et $al.$ reported a much higher thermal expansion coefficient along c-axis in Gd_6UO_{12} and attributed it to increased coulombic repulsion between two adjacent cations (Gd^{3+}) due to small cationic radii [96]. The same effect of increased coulombic repulsion doesn't appear in Dy_6UO_{12} where α_a is again found to be more than α_c and it remains an open question to be explained. The lattice thermal expansion coefficients increase with increasing temperature and expansion is more along the a-axis compared to the c-

separate two U polyhedra along the *c*-axis in the hexagonal representation of rhombohedral lattice. In these compounds, the bonding is conceived to be mostly ionic. The positions of the various atoms in the unit cell are given in table 1.1.

Table 1.1- *Atom coordinates for RE$_6$UO$_{12}$ compound* [93].

Constituent\Coordinates	X	Y	Z
U	0	0	0
RE	0.1254 ±0.0004	0.4150 ±0.0004	0.0205 ±0.0004
O(1)	0.200 ±0.006	0.026 ±0.006	0.126 ±0.006
O(2)	0.145 ±0.006	0.453 ±0.006	0.270 ±0.006

Table 1.2- *Lattice parameter, thermal expansion coefficient parameter and heat capacity of various Rare-Earth Uranates*

Compounds	Lattice Parameters- Hex. Parameter (Å)	Thermal expansion coefficient (10^{-6} K^{-1})	Heat capacity (J mol^{-1} K^{-1})
La$_6$UO$_{12}$	a =10.487(4) c =9.963(3) [101]	α_a=9.78±1.11 α_c=8.28±1.00 at 298K [101]	407 [102]
Nd$_6$UO$_{12}$	a =10.255(6) c =9.748(1) [101]	α_a=10.14±0.89 α_c=7.95±0.36 at 298K [101]	433 [103]
Sm$_6$UO$_{12}$	a =10.163 [101] c =9.641	α_a=10.79±0.85 α_c=8.51±0.49 at 298K [101]	439 [102]
Eu$_6$UO$_{12}$	a =10.126 [104] c =9.601	α_a=10.5±1.0 α_c=7.3±1.0 at 298K [102]	461 [102]
Gd$_6$UO$_{12}$	a =10.0878(6) c =9.5424(7) [104]	α_v=6.616 [96] α_v=19.593 at 373K	386.04 [96]
Tb$_6$UO$_{12}$	a =10.006(12) c =9.458(3) [97]	α_a=2.67 α_c=1.38 at 298K [97]	422.04 [97]
Dy$_6$UO$_{12}$	a =9.9806(7) c =9.4403(8) [104]	α_a=3.02 α_c=2.68 at 298K [105]	462 [105]

systems, many RE_6UO_{12} type compounds are synthesized and their crystal structures are determined [93].

Another interesting aspect of these compounds is their high-pressure study. It is well known that rare earth sesquioxides show various phase transitions: cubic $\rightarrow$ hexagonal $\rightarrow$ monoclinic $\rightarrow$ hexagonal at different pressures [94]. As both the rare earth sesquioxides and rare earth uranates show similar trend in thermal expansion behavior at high temperatures, therefore, it is well expected to follow a similar phase transition trend under high pressure [95–97]. In view of this, HP & HP-HT studies have been carried out to explore the physical properties of rare-earth uranates.

1.4.2 Structure of Rare-Earth Uranates:

Uranate compounds are ternary oxides where the element uranium is in any one of the following oxidation states of +4, +5 or +6. The typical chemical formula of uranate is $RE_xU_yO_z$, where RE represents a cation. RE-U-O phase diagram has been reported long back in the literature [98]. In the phase diagram RE_6UO_{12} (RE=Rare Earth elements) type of compounds, called Rare-earth Uranates, form by heating a mixture of Uranium oxide and rare earth oxides (in a ratio of 1:6 respectively) above 1273 K. Rare earth Uranates - RE_6UO_{12} type of compounds exist in the rhombohedral structure at ambient [99,100].

The unit cell of the rhombohedral phase of RE_6UO_{12} is large with 3 formula units $i.e.$ 57 atoms in a cell. Six oxygen atoms surround each uranium and RE^{3+} forming two distorted octahedra with uranium and RE^{3+} at the center. All the U-O distances are same in the structure. The structure can be visualized in the form of distorted octahedra with U and RE at the center and surrounded by six oxygen atoms. The two edge sharing RE octahedra

Figure 2 shows 2-D plot of Zunger-pseudo potential radii (ΔR) vs average electronegativity (ΔX) for UX_2 and UX_3 compounds constructed by Villars *et al.* More than 15 compounds were considered for each domains. It is evident from the figure 2 (a) that most of the compounds stabilize in $MgCu_2$ type structure because of low ΔX, ΔR values and higher VE. The structural maps also pave the way to identify new probable high-pressure phases as the application of high pressure causes an increase in VE and decrease in ΔR values. The domain in the 2-D structural map corresponding to the values of VE and ΔR for high-pressure phase suggests a new structure type at high pressure. These maps have been extensively used for this thesis to predict the new structures at high pressure.

1.4 HP & HT studies on RE_6UO_{12} compounds

1.4.1 Rare-Earth Uranates

Uranates are compounds that are likely to be formed during UO_2 irradiation as a decay product in nuclear reactors as a result of fuel-fission product interaction. Initial fuel enrichment in the reactor leads to the high reactivity of the fuel, hence reactivity is to be controlled by introducing neutron absorbers. The use of Gadolinium, as neutron absorbers, in uranium-oxide fuel matrix of BWR reactors is practiced since the mid-1960s. Since gadolinium has high neutron absorption coefficient and is a burnable absorber, gadolinia-doped Urania is progressively used in reactors [92]. It also prevents further oxidation of uranium oxide fuel (UO_2) to U_3O_8 at high temperatures. UO_2 shows substantial solubility with the rare earth oxides due to their similar ionic radii leading to increased probability of formation of such compounds in the oxide fuel matrix [92]. Due to interest in these

calculation for URh$_3$ shows a small peak of f-band located at the Fermi energy which remains pinned at the same position even up to 40 GPa [86].

1.3.3 Structural Stability Maps

In order to systemize the experimentally available structures of uranium intermetallics and predict their possible high-pressure phases, structural stability maps were generated using semi-empirical methods. These maps provide a connecting link between the structure type and the electronic configuration of the constituents. The earliest and the most accurate structural stability map was from Villars (1989) who has used the geometric criteria such as Zunger-pseudo potential radii (ΔR), average electronegativity (ΔX) and average number of valence electrons per atom (VE) as physical coordinates to generate 3-D plots which gave 97% accuracy for AX, AX$_2$ and AX$_3$ type intermetallics, later, these maps were extended to more than 8000 compounds [51,88–91].
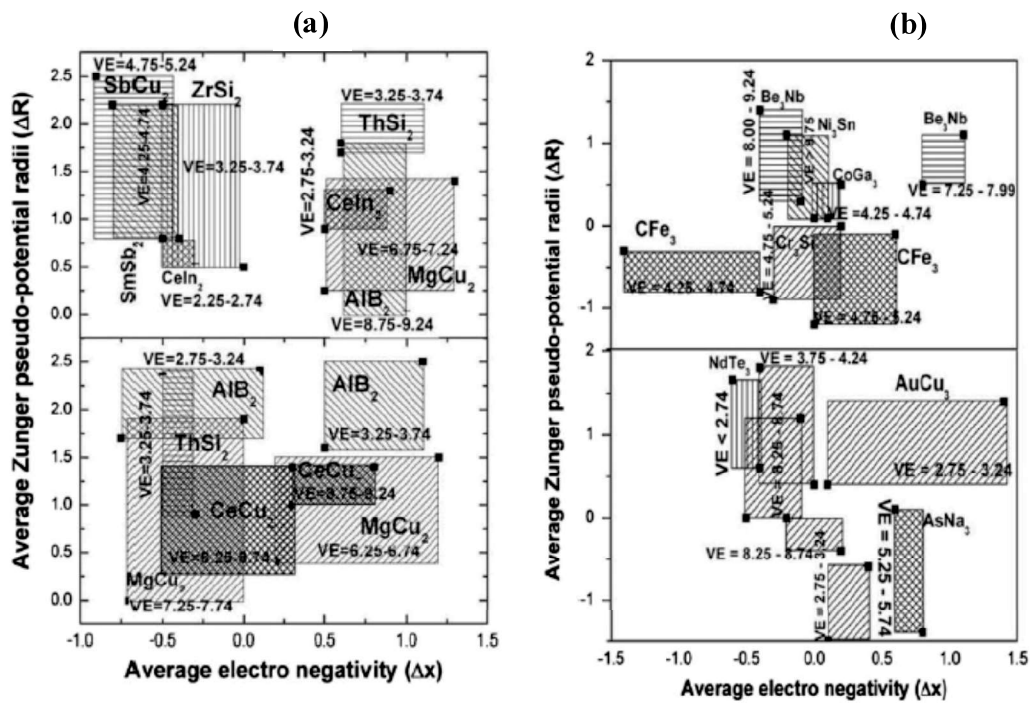
Figure 1.2- *2-D Structural Stability Maps for **(a)** UX$_2$ intermetallics **(b)** UX$_3$ intermetallics*

and d (non-actinide site) orbital [80]. Compounds like UPd_3 and UPt_3 have weak hybridization as compared to URh_3 and UIr_3, while URu_3 shows very strong hybridization. UPt_3 stabilizes in $MgCd_3$ (hexagonal) type structure and shows heavy fermion behavior [81] due to s-wave cooper pairing induced by electron-phonon interaction. The hybridization is found to decrease with increasing ionic size as X-d band moves away from the U-f band with increasing valency of X element, hence increasing the separation between the two bands. Koelling et $al.$ tried to systemize the properties of the AX_3 type compounds on the basis of hybridization of f-state with the s, p and d states of transition metals [80]. Mostly the position of the d band with respect to f band at Fermi energy is found to be important for hybridization strength [82].

Another interesting trend in UX_3 type compounds with isoelectronic pairs (same column X element in the periodic table) like URh_3 - UIr_3 is observed. URh_3 and UIr_3 have $4d$ and $5d$ orbitals, respectively. The $5d$ band has more width as compared to the $4f$ band in the same column. Therefore, the hybridization between U-f and X-$5d$ orbitals is more than the respective X-$4d$ orbitals [82]. This effect is clearly seen in compounds like URh_3 and UIr_3 which has been discussed in this thesis chapter 5.

A UX_3 compound-UAl_3 was studied by Chandra Shekar et $al.$ under high pressure and an anomaly in the P-V compression curve was reported [83]. Further, it was attributed to the f-d electron transfer. UPt_3, UPd_3, UGa_3, URh_3 and URh_3 has been studied earlier [39,84–86]. The electronic structure calculation shows the materials to be stable over a large range of pressure and does not undergo any phase transition to its probable high-pressure structure (Ni_3Sn type hexagonal structure) [87]. The density of state

The daughter bcc phase has higher unit cell volume which leads to expansion [71]. It has also been reported that the transition pressure from ω to bcc phase decreases with increasing temperature, and the decrease is quite significant such that bcc phase appears at 6 GPa and 973 K [70]. The omega phase of the material is interesting to study because of its phase transition mechanism and better mechanical properties [72–76].

In UZr_2, AlB_2 type hexagonal unit cell, Zr occupies corner (000) position. Further U and Zr randomly occupy (1/3, 2/3, 1/2) and (2/3, 1/3, 1/2) positions [77,78]. X-ray diffraction study by Boyko *et al.* brought out the intensity differences between the observed and calculated pattern which can be attributed to the randomness in the uranium and zirconium positions at (1/3, 2/3, 1/2) and (2/3, 1/3, 1/2) [77]. In this thesis, we have carried out the X-ray diffraction study of UZr_2 at synchrotron source and Rietveld refinement to estimate the randomness.

Earlier, neutron diffraction study on δ-UZr_2 describes the variation of lattice parameter at high temperatures [79]. In this work, we have carried out *in-situ* HP & HP-HT study on δ-UZr_2 using the high-resolution X-ray diffraction technique and are discussed in chapter 4.

1.3.2 AX_3 type compounds

Similar to AX_2 type compounds, AX_3 (A=rare-earth, X=p or d block element) compounds stabilize in $AuCu_3$ type Laves cubic structure and not much information is available about these compounds. As described earlier, the Hill criterion decides the nature of f-electrons through the mechanism of actinide-actinide separation. However, there are few compounds which are exceptions to the Hill limit criteria e.g. UIr_3, URh_3, UGe_3 etc. The reason for this was further attributed to the U-X distance and the character of the hybridization between f

The *nu2* type AlB_2 structure resembles omega (ω) phase (ideal c/a =0.612) which has better mechanical properties, hence becomes technologically important.

One of the AlB_2 type compound, UZr_2 has been studied in this thesis. Structurally it is alike to omega structure at ambient pressure and temperature. The compound is important from the nuclear industry point of view. U-Pu-Zr alloy is a candidate fuel material for metallic fuel based fast reactors [64]. A typical fuel contains 23% of zirconium. Due to thermal gradient generated in the fuel pin during the burn-up, redistribution of uranium and zirconium takes place. Zirconium is enriched at the center of the fuel pin and uranium concentration decreases at the center [65,66]. At higher burnup of the fuel, gamma and δ phase of UZr_2 may form inside the fuel pin at homogeneity range ~63-78% Zr [66]. Therefore, it becomes interesting to study its behavior under various temperatures and pressures.

U-Zr binary phase diagram clearly shows the existence of only δ phase in the homogeneity range 63.2-78.2% Zr [67–69]. The phase forms on cooling below 908 K from the high-temperature bcc U-Zr solid solution. *Basak et al.* maintained various quenching rates and observed the formation of the compound, and established that cooling/quenching must be done below 823 K to arrive at the δ phase, failing which a mixture of δ and bcc phase would be obtained [67]. High-temperature gamma phase transforms to metastable-δ phase by ω phase transformation mechanism where alternate *(111)* planes of gamma phase collapse and form AlB_2 type (C32) hexagonal crystal structure which is related to the ω structure [67]. T. Ogawa *et al.* explained that δ structure stabilizes due to increase in the *d* band occupancy of zirconium wherein a significant mixing of uranium valence shell with zirconium *d* band is seen [70]. Moreover, Zr metal goes to the bcc structure at ~33 GPa.

transformations are known to exist for $REOs_2$ (RE=Rare Earth) compounds [61] and was attributed to different stacking sequences of atomic layers [62]. Since pressure transfers more energy to the material as compared to temperature, the transformation is expected to happen at low pressures. Also, to explore the possibility of high bulk modulus compound with uranium, compressibility study of UOs_2 is desirable. Therefore, the X-ray diffraction study on the high-temperature metastable $MgCu_2$ type phase was performed to check the stability of the lattice under high pressure and the results are discussed in chapter 4.

At ambient, UIr_2 stabilizes in $MgCu_2$ type cubic Laves phase. High-Pressure X-ray diffraction (HP-XRD) of UIr_2 has been reported earlier wherein Syassen-Holzapfel type DAC was used to achieve static high pressure. In the report, HP-XRD was carried out in energy dispersive mode using laboratory source and UIr_2 was reported to be stable up to 50 GPa [56]. In contrast, our high-resolution work in this thesis reports a phase transition at 25 GPa [55] and is discussed in detail in chapter 4.

1.3.1.2 AlB_2 type compounds.

These compounds show a variety of phase transitions due to its Fermi energy being positioned very close to the *f-d* hybridized peak in DOS vs Energy plot [63]. Although the position of Fermi energy with respect to the *f-d* hybridized DOS is important, *f* band DOS alone plays an important role from the point of structural stability. There are two kinds of AlB_2 type structures seen in AX_2 type compounds which are characterized according to their *c/a* ratio. One with *c/a* =0.95-1.27 is called *kzl* structure (coordination number 9) and another one with *c/a* =0.59-0.88 (coordination number 11) is called *nu2* type structure [52]. *kzl* structures in AX_2 compounds like Rare-earth digallides, are also found to transform to *nu2* type structures at high pressures due to its lower *c/a* and higher coordination number.

32

pseudo-gap at Fermi level, therefore, the probability of any significant changes in the DOS at Fermi level becomes imperceptible as a function of pressure. Hence, $MgCu_2$ type Laves phase remains stable up to high pressures. It was confirmed by the HP-XRD experiments on various AX_2 type systems [55–57]. At very high pressures the following structural sequence for UX_2 compounds is established: Laves phase $\rightarrow$ $MoSi_2$ (Tetragonal) $\rightarrow$ $CeCd_2$(hexagonal) $\rightarrow$ $CeCu_2$ (orthorhombic) $\rightarrow$ $CaIn_2$ (hexagonal) $\rightarrow$ AlB_2 (hexagonal) $\rightarrow$ $ZrSi_2$ (orthorhombic) $\rightarrow$ $ThSi_2$ (tetragonal) $\rightarrow$ $SmSb_2$ (orthorhombic) $\rightarrow$ Cu_2Sb (tetragonal).

Among actinides, uranium is one element which can be handled with relative ease and its compounds show variety of behaviors like Kondo lattice, heavy fermion, superconductivity and so on [48,58]. Hence, uranium intermetallics were identified to study as a part of this thesis and the compounds- UOs_2, UIr_2, and UZr_2 were chosen for this purpose. Among $MgCu_2$ type UX_2 compounds, the compound UOs_2 has been studied in this thesis to explore its high bulk modulus aspect. UIr_2 has been studied in order to observe the high-pressure systematics along the period of the periodic table. UZr_2 is another compound among AlB_2 type compounds which is interesting because of its ambient ω phase structure. As ω phase of Zr shows very interesting phase transitions with pressure and temperature, the exploration of HP & HP-HT properties of UZr_2 are desirable. The literature reports on these compounds are described here in detail-

UOs_2 has two allotropic forms, namely a high-temperature cubic $MgCu_2$ type Laves phase [59] similar to UIr_2 and another low-temperature hexagonal $MgZn_2$ type Laves phase which can be obtained by heating the $MgCu_2$ type cubic phase at 1073 K [60]. The same structural transformation with temperature was also observed in URe_2 which has low temperature orthorhombic and high-temperature hexagonal phase. Such type of

31

1.3.1.1 Laves compounds in AX_2

Most of the AX_2 compounds stabilize in $MgCu_2$ structure because of very low electronegativity value, Zunger pseudo potential radii and higher valence electron [51]. $MgCu_2$ type Laves phase compounds do not undergo any phase transition even up to fairly high pressure and show high bulk modulus, except some exceptions like UAl_2 and UMn_2. The main factor contributing to the stability of the Laves phases (including $MgZn_2$ and $MgNi_2$ phase) is geometrical in origin. For maximum space-filling, close contact in A-A and X-X pairs is required and it turns out that this is possible only for a radius ratio of $R_A/R_X = 1.225$. The Laves phase structures have been found for radii ratio between 1.06-1.68 [52], explaining the stability of the structure.

Another stabilization criterion is from the electronic structure point of view. $MgCu_2$ type structure stabilizes when free electron concentration per atom is less than 1.8 and more than 2.3 [51,53,54], and for $1.8 < e/a < 2.3$ $MgZn_2$ and $MgNi_2$ structure exist. It was further validated [46] by pseudo-binary alloys in $RE(Al_{1-x} X)$, X=Co, Fe, Ni etc. when the concentration of Al increases; the structure changes from $MgCu_2 \rightarrow MgZn_2 \rightarrow MgCu_2$. In addition to this, UAl_2 with $e/a=1.66$, shows a phase transformation to $MgNi_2$ structure at high pressure when e/a increases more than 1.8 and it is proposed that it may further transform back to $MgCu_2$ structure when e/a exceeds 2.3 [51]. REO_2 (RE=Rare Earth) also shows a structural phase transition to $MgZn_2$ under pressure due to increased delocalization of f-electron states under pressure. Therefore, according to the free electron concentration, the structural phase transitions can be predicted.

The stability of $MgCu_2$ type Laves phase can also be proved theoretically using density of state (DOS) calculations. The density of state of $MgCu_2$ type systems lies in a

the nuclear energy, also, they provide a testing ground for the theory of electron correlation in magnetism such as Hubbard and Anderson model [47,48].

Among all the A_mX_n compounds, AX type compounds have been studied to a large extent after several decades of intensive research and a systematic tread for their high-pressure behavior have emerged. Most of these compounds stabilize in NaCl (B_1) type crystal structure at ambient and a B_1 to B_2 (CsCl) type structural phase transition is observed under pressure. The phase transition and stability of the AX type compounds have been described in the literature [39,49]. The stability range of various AX type compounds also suggests that the transition pressure decreases with increasing atomic number of the anion in a column of the periodic table and the transition pressure increases with increasing atomic number of the actinide [50]. In spite of all the studies in actinide binary compounds, no systematics have been observed in AX_2 and AX_3 type intermetallic compounds and there are large number of compounds which are not yet studied under pressure. The search for less compressible actinide intermetallic compound has been underway for decades because of its various applications.

1.3.1 AX_2 type f-IMCs

Most of the AX_2 type compounds are found to stabilize in $MgCu_2$ type Laves phase (UX_2, X=Fe, Co, Ir, Os; AX_2, A=rare earth and X=Ru, Os, Fe, Co, Ni etc.) at ambient. It shows that $MgCu_2$ type structure is stable over a large range of band electrons in such compounds. Some of the AX_2 type compounds e.g. rare-earth digallides, HT-URe_2, UZr_2 etc. exhibit AlB_2 type structure at ambient.

Intra-atomic coulomb correlation energy- U:

$$U = K.E. + P.E \propto \frac{A}{V^{\frac{2}{3}}} + \frac{B}{V^{\frac{1}{3}}} \propto n - l - 1 \qquad (1.7)$$

Where d is the inter-atomic distance, l is the orbital quantum number, V is the volume which can be altered by the application of pressure and temperature.

The localized $5d$ electrons i.e. BW<U (according to Mott-Hubbard criterion) may become itinerant i.e. BW>U by changing external thermodynamic parameters. Itinerancy so introduced may lead to phase transition to low symmetry structures having higher bulk modulus [41–43]. Lindbaum *et al* have studied the crystal structure of actinide elements under pressure and shown that itinerant $5f$ electrons lead to more complex structures and relatively large bulk moduli) [44].

Some of the empirical methods like Ratio of radii R_A/R_B (A= RE or An and B= transition metals) of two atoms for binary compounds [45,46] and number of free electrons per atom (e/a) also have been used to decide upon the nature of f-electrons. In general, a decrease in the R_A (in one of the approach) and an increase in the e/a ratio (in another approach) are indications of the delocalization of the f-electrons. The increase in the number of free electrons causes an increase in Fermi energy and transition happens when Fermi energy crosses Brillouin zone as it is energetically favorable.

1.3 HP Investigation on f-electron Intermetallics (f-IMCs)

f-IMCs are the A_mX_n type compounds, where A belongs to rare earth or actinide and X belong to p or d block metals. The nature of the bonding in these compounds is mostly metallic. Research in actinide compounds has paved the way for the advancement towards

Figure 1 shows the Hill plot for uranium binary inter-metallic compounds, describing its Hill limit and [39]. Although some of the compounds do not follow the systematic as hybridization of non-f-electron constituent atoms, e.g. f-p, f-d, too play a key role in the electronic and magnetic properties of the compounds, but Hill criterion has been a very useful indicator of itinerancy or localization of f-electrons.

Another theoretical approach to identify the itinerancy and localization of $5f$ electrons is by using Mott-Hubbard criterion [40] which compares the $5f$ state Band Width (BW) and the intra-atomic coulomb correlation energy (U). If BW<U, the $5f$ states would be localized as binding of electrons to nucleus is stronger; and if BW>U, it implies itinerant $5f$ states due to increased $5f$ orbital overlap. The values of BW and U can be altered by varying external thermodynamic variables like pressure, temperature etc. deciding the nature of the f-electrons, hence controlling the properties of actinide compounds. The general observation in uranium intermetallic compounds is that its $5f$ electrons are itinerant in most of the compounds whereas some of the compounds like UPd_3 shows localized behavior.

1.2.1 Effect of pressure on BW and U

Pressure brings several changes in the material apart from the changes in their lattice properties as described in section 1.1.1.4. The bandwidth, BW, is found to increase as a function of pressure and the broadening is different for different orbitals which can be estimated using the relations:

$$BW(P) = BW(P = 0) \left[\frac{d(P)}{d(P=0)} \right]^{-(2l+1)} \rightarrow BW(P) \propto l \qquad (1.6)$$

27

To systemize and generalize the nature of actinide compounds, Hill suggested that actinide-actinide (An-An) distance regulates the properties of f-f electron orbital overlap in the compound through which their magnetic properties can be addressed [36]. Hill plot simply shows the superconducting transition temperatures or magnetic transition temperatures as a function of the actinides inter-atomic distances in pure metals, alloys, and compounds. The plot lists two groups of compounds- one with the localized $5f$ electrons and another with itinerant $5f$ electrons according to their An-An distances. There exists a narrow range of An-An distance, known as Hill transition zone or Hill Limit which separates two regions. For compounds of U, Np, Pu and Am the Hill limit are 3.5 Å, 3.25 Å, 3.4 Å, and 3.26 Å respectively [36–38].
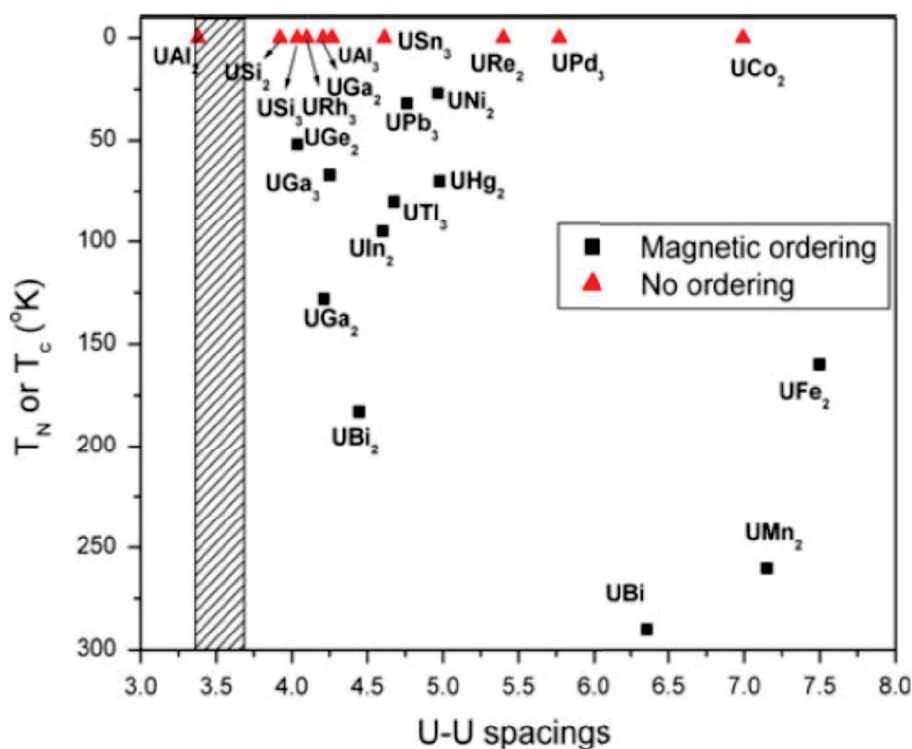
Figure 1.1- Hill Plot for binary compounds of uranium intermetallics [39].

26

using density functional theory [29]. The value of this term is negligible as compared to the first two terms, hence often it is neglected.

1.2 Dual nature of *f*-electrons in actinides

The localization or non-binding character of the 4*f* electrons of the lanthanide elements are well known, hence most of the lanthanides are trivalent and their volumes decrease smoothly from lanthanum to lutetium; except europium and ytterbium which are divalent metals. Localization and itinerancy of the 5*f* electrons play a very important role in deciding the properties of the materials. Localized electrons show local magnetism, however, itinerant 5*f* electrons participate in the bonding leading to the higher strength of the material. In comparison to lanthanides, due to the larger spatial extension of 5*f* wave functions, actinides display two different behaviors- lower actinides mimicking transition metals and higher ones analogous to lanthanides with a crossover at Pu and Am. This crossover greatly influences the phase diagram and hence properties of the actinide materials. Even the compounds of a particular actinide show a variety of behavior from localized to itinerant due to small changes in the number of 5*f* electrons contributing to bonding. Electronic structure band dispersion study results from photoemission experiments in some of the uranium compounds like USb_2 showed the partial hybridization of 5*f* electrons at Fermi level, while other 5*f* electrons remains localized [30,31]. Dual nature approach has been employed to several actinide compounds for their electronic structure determination and it gives very good agreement with the photoemission spectra, corrected volumes, and magnetic configurations [32,33]. Therefore, the ability of 5*f* electrons to participate in the conduction band and remain localized simultaneously makes actinides & its compounds fascinating to study [34,35].

P(V, 300 K) is the pressure at 300 K and can be expressed in terms of 3rd order Birch Murnaghan EOS [23] or Vinet EOS [24]. Both the EOS are given by the following equations,

3rd order BM's EOS:

$$P(V, 300K) = \left(\frac{3Bo}{2}\right)\left[\left(\frac{Vo}{V}\right)^{\frac{7}{3}} - \left(\frac{Vo}{V}\right)^{\frac{5}{3}}\right]\left\{1 + \frac{3}{4}(B' - 4)\left[\left(\frac{Vo}{V}\right)^{\frac{2}{3}} - 1\right]\right\} \qquad (1.4)$$

Vinet EOS:

$$P(V, 300K) = 3B_0\left(\frac{V}{Vo}\right)^{-\frac{2}{3}}\left[1 - \left(\frac{V}{Vo}\right)^{\frac{1}{3}}\right]\exp\left(\frac{3}{2}(B' - 1)\left[1 - \left(\frac{V}{Vo}\right)^{\frac{1}{3}}\right]\right) \qquad (1.5)$$

P_{TH} (V, T) in equation (1.3) is the lattice pressure or thermal pressure caused by heating the material up to temperature T at constant volume. The value of thermal pressure is sample specific and depends on the thermal expansion of the material i.e. higher the thermal expansion coefficient higher would be the thermal pressure contribution [25–27]. Thermal pressure contribution to the total pressure is found to increase at high temperatures but remains independent of the external pressure applied as long as the volume of the sample chamber remains constant [21]. During the HP-HT experiment the volume of the sample assembly remains approximately constant inside the DAC, hence, the amount of thermal pressure is significant. Ignoring thermal pressure values gives erroneous pressure estimation which has also been confirmed during HP-HT experiment of Dy_6UO_{12} contained in the thesis [28].

P_{el} (V, T) in equation (1.3) is the electronic thermal pressure that arises from e^--e^- interaction and can be estimated from the first-principles electronic structure calculations

24

$$\alpha_l = \frac{\Delta L}{L \Delta L} \quad \& \quad \alpha_V = \frac{\Delta V}{V \Delta V} \tag{1.1}$$

Where ΔL and ΔV are change in the length and volume of the material, respectively, under ΔT temperature change. The average linear expansion coefficient $\bar{\alpha}$ can be estimated by the expression,

$$\bar{\alpha} = \frac{\alpha_V}{3} = \frac{\alpha_a + \alpha_b + \alpha_c}{3} \tag{1.2}$$

α_a, α_b and α_c are expansion coefficient along three axes of the bravais lattice.

Grüneisen parameter is another very important thermodynamic parameter which is used to quantify the relationship between thermal and elastic properties of a solid. It describes the effect of change in the volume of a crystal upon its vibrational properties.

1.1.3 High Pressure-High temperature effects

The coefficient of thermal expansion is needed at high pressures (megabar range) for developing an understanding of their equation of state (EOS), for various geophysical calculations and nuclear industry [21]. Homogenous pressure, for instance in DAC, acts as a resistance in the thermal expansion of the material, hence, the expansion coefficient usually decreases as a function of increasing pressure.

To estimate the equation of state at high pressure and high temperature, the pressure can be described as [22],

$$P(V,T) = P(V, 300K) + P_{TH}(V,T) + P_{el}(V,T) \tag{1.3}$$

higher pressures. However, in some materials cations are found to be responsible for the PIA.

1.1.1.4 Electronic Effects

Another effect that may arise due to the application of external pressure on the material is the overlap of outer electronic orbitals which may lead to several changes like:

1. Broadening in the bandwidths, extent of hybridization of the outer electronic orbital
2. Shifting of energy band with respect to the Fermi Energy
3. Shifting in the Fermi energy
4. Modification in the Fermi surface

These electronic effects may cause a metal to insulator transition [18], inter-band electron and valence transitions [19], Lifshitz transitions [20] etc. in the materials which reflect as change in various physical properties e.g. electronic specific heat, susceptibility etc.

1.1.2 High-temperature effects on materials

Temperature affects a material in various ways by redistribution of internal energy in a system. Some of the thermal effects in the materials are: physical effects-basic thermal expansion, phase change, plastic changes; chemical effects-reaction, decomposition, oxidation etc. These changes are material specific i.e. metals, ceramics, polymers, composites behave differently with temperature. Thermal expansion coefficient is a basic physical parameter to assess the material functioning. It can be defined as the response of the material upon heating or cooling. The axial (α_l) and volume (α_v) thermal expansion coefficient of a crystal are defined as:

22

atoms i.e. whether the atoms move together or independently. In displacive transformations, atoms move in an "organized" manner in unison relative to their neighbors which creates a new crystal structure without any compositional change (no diffusion). Whereas, diffusive transition involves the formation of droplets (nucleation) of the daughter phase within the parent phase wherein the atoms diffuse randomly across the boundary of the two phases [5].

1.1.1.3 Pressure-Induced Amorphization

An amorphous (non-crystalline) solid is a solid that lacks the long-range order. Pressure-induced amorphization (PIA) was first reported in 1972 when β-$Gd_2(MoO_4)_3$ was found to amorphize under pressure [6] and subsequently, large number of compounds were found to amorphize under pressure. Though, some of them were ruled out later in the following decade. The phenomenon remained exciting from the point of view of physics since it was essential to understand as to what the driving force and the route of phase transition are? [7–9]. Later, with the advent of new sophisticated characterization techniques (X-ray absorption spectroscopy, Photoluminescence and Raman spectroscopy) and simulations, several mechanisms to explain the transition to amorphous phase have evolved. PIA is a first order transition from crystalline phase to amorphous phase due to the application of external pressure. The first order phase transition (abrupt transition- potentially quenchable) between the two phases opened a new way of synthesis of novel materials. They are found to have anisotropy and memory effects as well [10,11].

Several similar $A_xB_yO_z$ (e.g. pyrochlore) type oxides have already been reported to show PIA at various pressures [12–17]. Distortions in the internal structure (polyhedron) lead to the origin of the disorder in the system and the materials eventually amorphize at

In spite of the usefulness of Ehrenfest theory, it becomes inadequate in explaining the phase transition wherein the derivatives diverge, for instance-divergence of heat capacity in ferromagnetic and superconducting phase transitions. To explain the anomaly, L. Landau formulated a general theory in the 1940s to describe second order phase transition. The theory has been extremely useful in the thermodynamic description of phase transition. It provides an excellent tool to explain the high-pressure induced structural transitions [4].

1.1.1.2 Pressure-induced structural phase transitions

Apart from solid, liquid and gaseous transitions, the material may transform from one crystalline structure of solid to another crystalline or non-crystalline phase of solid due to changes in external thermodynamic variables like pressure, temperature etc. The effect of pressure on crystalline solids can bring two types of changes, most often these two effects are correlated to each other:

    1. Lattice compression

    2. Electronic structural change in the material

The lattice compression brings atoms closer which leads to change in phonon spectra, increase in free energy and so on. The change in the free energy may lead to stabilization of a new phase as lower free energy of daughter structure may be favorable. The rate of change in the free energy depicts the type of phase transition. The discontinuity in the first or second order derivatives of the Gibbs free energy shows first or second order phase transitions, respectively. However, the mechanism that facilitates the solid to solid transition can be described in two ways –displacive (martensitic or reconstructive transformations) and diffusive -in which atoms can rearrange themselves to transform to a new structure. Both the transformation routes depend on the extent of movement of the

at extreme conditions of pressure and temperatures. Some of these compounds are also formed in the fuel matrix during the operation of nuclear reactors. Hence structural stability studies of these compounds at HP-HT become relevant. Also, Uranium Intermetallic Compounds (UIMCs) become important for future metallic fuel reactors.

1.1 Effect of high pressure and temperature on materials

1.1.1 High-Pressure effects on materials

Pressure brings more significant changes in materials than temperature e.g. pressure can bring a maximum of 70 % volume change at 100 GPa as compared to 10 % volume change due to temperature at its melting point. All the materials in this thesis have been studied under pressure and will be discussed in the subsequent chapters. The changes which could arise in the materials due to the application of external pressure are as follows:

1.1.1.1 Phase transitions in general

A phase of a thermodynamic system has uniform physical properties in thermodynamic equilibrium. During a phase transition, certain properties of the medium change because of the change in external conditions, such as- temperature, pressure etc. These changes in the physical properties of the medium may be continuous or discontinuous, depending on which the nature of phase transition is characterized.

Ehrenfest classification is an important aid in classifying the phase transitions on the basis of discontinuity in derivatives of free energy as a function of thermodynamic variables. The first and second order derivatives of free energy with respect to some thermodynamic variables signify the transition to be first or second order phase transition, respectively.

Chapter 1

Introduction

The behavior of materials under extreme conditions has been under intense study for decades. Physics at extreme conditions of pressures & temperatures are very interesting and materials under such conditions are widely studied to explore their physical and mechanical properties. Pressure induces significant changes, as compared to temperature, in the physical and chemical properties of the materials. Also, the advent of advanced High Pressure and High Temperature (HP-HT) Diamond Anvil Cell (DAC) and *in-situ* laser heating tools, contributed to the tremendous increase in research in this field [1]. Actinides, being reactor fuel materials, are among the most studied materials from technological and physics point of view, hence, the study of its compounds are desirable under extreme conditions. The interest in the High Pressure (HP) properties of actinides started with lanthanides- the $4f$ elements- and further extended to other $5f$ elements which showed even more fascinating properties [2]. The nature of f electrons has been probed consistently over time because of its anomalous behavior in its various compounds [3]. As f-electrons are solely responsible for the nature of the compound, the lanthanide & actinide intermetallics and oxide compounds yield fascinating & challenging results which are yet to be understood. Intermetallics have been probed to find out their structural stability in compounds having large bulk moduli and study the properties of ω phase in these materials. Further, rare-earth uranium oxides, having similar characteristics of rare-earth sesquioxides, are studied to find out the structural stability and interesting phase transitions

18

Synchrotron Radiation: The Next Steps (Grenoble, France:ESRF, 1997).

[64]   S. S. Jha and J. W. F. Woo, Nuovo Cim. B **10**, 229 (1972).

[65]   D. A. Arms, R. O. Simmons, M. Schwoerer-Böhning, A. T. Macrander, and T. J. Graber, Phys. Rev. Lett. **87**, 156402 (2001).

[66]   J. P. Hill, C. C. Kao, W. A. C. Caliebe, D. Gibbs, and J. B. Hastings, Phys. Rev. Lett. **77**, 3665 (1996).

[67]   A. Kotani and S. Shin, Rev. Mod. Phys. **73**, 203 (2001).

[68]   J. P. Rueff, S. Raymond, A. Yaresko, D. Braithwaite, P. Leininger, G. Vankó, A. Huxley, J. Rebizant, and N. Sato, Phys. Rev. B **76**, 85113 (2007).

[69]   J. S. Tse, D. D. Klug, D. T. Jiang, C. Sternemann, M. Volmer, S. Huotari, N. Hiraoka, V. Honkimäki, and K. Hämäläinen, Appl. Phys. Lett. **87**, 1 (2005).

[70]   J. R. Patterson, S. A. Catledge, Y. K. Vohra, J. Akella, and S. T. Weir, Phys. Rev. Lett. **85**, 5364 (2000).

[71]   S. T. Weir, J. Akella, C. Aracne-Ruddle, Y. K. Vohra, and S. A. Catledge, Appl. Phys. Lett. **77**, 3400 (2000).

[72]   A. P. Hammersley, J. Appl. Crystallogr. **49**, 646 (2016).

[73]   A. P. Hammersley, S. O. Svensson, M. Hanfland, A. N. Fitch, and D. Hausermann, High Press. Res. **14**, 235 (1996).

[51] W. A. Bassett and M. S. Weathers, Phys. B+C **139–140**, 900 (1986).

[52] D. L. Heinz, J. S. Sweeney, and P. Miller, Rev. Sci. Instrum. **62**, 1568 (1991).

[53] J. F. Lin, W. Sturhahn, J. Zhao, G. Shen, H. K. Mao, and R. J. Hemley, Geophys. Res. Lett. **31**, L14611 (2004).

[54] D. L. Heinz, J. S. Sweeney, and P. Miller, Rev. Sci. Instrum. **62**, 1568 (1991).

[55] G. Shen, M. L. Rivers, Y. Wang, and S. R. Sutton, Rev. Sci. Instrum. **72**, 1273 (2001).

[56] R. J. Hemley, V. V. Struzhkin, and R. E. Cohen, in *Treatise Geophys.* (Elsevier, 2007), pp. 293–337.

[57] M. Kono, *Geomagnetism: Treatise on Geophysics*, 1st ed. (Elsevier, 2009).

[58] J. P. Itié, Phase Transitions **39**, 81 (1992).

[59] X. Hong, M. Newville, V. B. Prakapenka, M. L. Rivers, and S. R. Sutton, Rev. Sci. Instrum. **80**, 73908 (2009).

[60] N. Ishimatsu, K. Matsumoto, H. Maruyama, N. Kawamura, M. Mizumaki, H. Sumiya, and T. Irifune, J. Synchrotron Radiat. **19**, 768 (2012).

[61] V. M. Giordano, M. Krisch, and G. Monaco, J. Synchrotron Radiat. **16**, 707 (2009).

[62] J. F. Lin, H. Fukui, D. Prendergast, T. Okuchi, Y. Q. Cai, N. Hiraoka, C. S. Yoo, A. Trave, P. Eng, M. Y. Hu, and P. Chow, Phys. Rev. B - Condens. Matter Mater. Phys. **75**, 12201 (2007).

[63] F. Baudelet, S. Odin, and J. P. Itie, *Crystallography at High Pressure Using*

[39] M. J. Moore, D. B. Sorensen, and R. C. Devries, Rev. Sci. Instrum. **41**, 1665 (1970).

[40] C. S. Zha and W. A. Bassett, Rev. Sci. Instrum. **74**, 1255 (2003).

[41] S. Pasternak, G. Aquilanti, S. Pascarelli, R. Poloni, B. Canny, M. V. Coulet, and L. Zhang, Rev. Sci. Instrum. **79**, 85103 (2008).

[42] L. C. Ming, M. H. Manghnani, and J. Balogh, in (American Geophysical Union, 1987), pp. 69–74.

[43] L. C. Ming and W. A. Bassett, Rev. Sci. Instrum. **45**, 1115 (1974).

[44] J. F. Lin, M. Santoro, V. V. Struzhkin, H. K. Mao, and R. J. Hemley, Rev. Sci. Instrum. **75**, 3302 (2004).

[45] Q. Zhou, Y. Ma, Q. Cui, T. Cui, J. Zhang, Y. Xie, K. Yang, and G. Zou, Rev. Sci. Instrum. **75**, 2432 (2004).

[46] A. F. Goncharov and J. C. Crowhurst, Rev. Sci. Instrum. **76**, 63905 (2005).

[47] N. Subramanian, N. V. Chandra Shekar, N. R. Sanjay Kumar, and P. C. Sahu, Curr. Sci. **91**, 175 (2006).

[48] N. R. Sanjay Kumar, N. V Chandra Shekar, S. Chandra, J. Basu, R. Divakar, and P. C. Sahu, J. Phys. Condens. Matter **24**, 362202 (2012).

[49] N. R. Sanjay Kumar, S. Chandra, S. Amirthapandian, N. V Chandra Shekar, and P. C. Sahu, Mater. Res. Express **2**, 16503 (2015).

[50] N. V. Chandra Shekar, P. C. Sahu, and K. Govinda Rajan, J. Mater. Sci. Technol. **6**, 518 (2003).

[24]   R. A. Forman, G. J. Piermarini, J. D. Barnett, and S. Block, Science. **176**, 284 (1972).

[25]   J. D. Barnett, S. Block, and G. J. Piermarini, Rev. Sci. Instrum. **44**, 1 (1973).

[26]   F. D. Murnaghan, Proc. Natl. Acad. Sci. **30**, 244 (1944).

[27]   F. Birch, Phys. Rev. **71**, 809 (1947).

[28]   R. Jeanloz, Phys. Rev. B **38**, 805 (1988).

[29]   I. C. Sanchez and J. Cho, Polymer. **36**, 2929 (1995).

[30]   O. L. Anderson, Oxford Monogr. Geol. Geophys. **31**, 405 (1995).

[31]   K. Vinod, V. S. Malik, S. K. Sharma, and S. K. Srivastava, J. Phys. Chem. Solids **68**, 32 (2007).

[32]   D. L. Decker, J. Appl. Phys. **42**, 3239 (1971).

[33]   M. I. Eremets, *High Pressure Experimental Methods* (Oxford University Press, 1996).

[34]   H. K. Mao, P. M. Bell, J. W. Shaner, and D. J. Steinberg, J. Appl. Phys. **49**, 3276 (1978).

[35]   J. Xu, H. K. Mao, and P. M. Bell, Science **232**, 1404 (1986).

[36]   D. L. Heinz, Geophys. Res. Lett. **17**, 1161 (1990).

[37]   A. Dewaele, G. Fiquet, and P. Gillet, Rev. Sci. Instrum. **69**, 2421 (1998).

[38]   W. A. Bassett and T. Takahashi, Am. Mineral. **50**, 1576 (1965).

by A. K. Singh (Tata McGraw-Hill Pub. Co, New Delhi (India), 1995), p. 381.

[12] C. E. Weir, E. R. Lippincott, A. Van Valkenburg, and E. N. Bunting, J. Res. Natl. Bur. Stand. Sect. A Phys. Chem. **63A**, 55 (1959).

[13] J. C. Jamieson, A. W. Lawson, and N. D. Nachtrieb, Rev. Sci. Instrum. **30**, 1016 (1959).

[14] H. K. Mao and P. M. Bell, in *Year B. Carnegie Inst. Wash.*, Vol 77 (Washington, D.C. : Carnegie Institution of Washington, 1978), p. 904.

[15] H. K. Mao, Science **200**, 1145 (1978).

[16] D. M. Adams and S. K. Sharma, J. Phys. E. **10**, 680 (1977).

[17] D. M. Adams, S. J. Payne, and K. Martin, Appl. Spectrosc. **27**, 377 (1973).

[18] R. J. Wijngaarden and I. F. Silvera, *High Pressure Science and Technology : Proceedings of the 7th International AIRAPT Conference : (Organised Jointly with the EHPRG), Le Creusot, France, July 30-August 3, 1979* (Pergamon Press, 1980).

[19] K. R. Hirsch and W. B. Holzapfel, Rev. Sci. Instrum. **52**, 52 (1981).

[20] A. Valkenburg, Van., in (LeCreusot, Saone-Et-Loire, Frace, 1965).

[21] B. Shukla, N. V. Chandra Shekar, N. R. Sanjay Kumar, T. R. Ravindran, P. Sahoo, S. Dhara, and P. C. Sahu, J. Phys. Conf. Ser. **377**, 12014 (2012).

[22] G. J. Piermarini, S. Block, and J. D. Barnett, J. Appl. Phys. **44**, 5377 (1973).

[23] B. Shukla, N. R. Sanjay Kumar, M. Sekar, and N. V. Chandra Shekar, J. Instrum. Soc. India **46**, 75 (2016).

References

[1]   J. J. Moore and H. J. Feng, Prog. Mater. Sci. **39**, 243 (1995).

[2]   J. J. Moore and H. J. Feng, Prog. Mater. Sci. **39**, 275 (1995).

[3]   J. B. Holt and Z. A. Munir, J. Mater. Sci. **21**, 251 (1986).

[4]   H. C. Yi, A. Petric, and J. J. Moore, J. Mater. Sci. **27**, 6797 (1992).

[5]   C. C. Hwang, T. Y. Wu, J. Wan, and J. S. Tsai, Mater. Sci. Eng. B **111**, 49 (2004).

[6]   R. Venkata Krishnan, H. Jena, K. V. Govindan Kutty, and K. Nagarajan, J. Therm. Anal. Calorim. **101**, 371 (2010).

[7]   R. V. Krishnan, P. Manikandan, H. Jena, and K. Nagarajan, Thermochim. Acta **472**, 95 (2008).

[8]   L. Dubrovinsky, N. Dubrovinskaia, V. B. Prakapenka, and A. M. Abakumov, Nat. Commun. **3**, 1163 (2012).

[9]   K. Gopalan, V. K. Gaur, B. L. K. Somayajulu, and J. D. Macdougall, in *From Mantle to Meteorites a Garl. Perspect. a Festschrift Devendra Lal* (Oxford University Press, 1991), p. 322.

[10]   P. C. Sahu, M. Yousuf, N. V. Chandra Shekar, and K. G. Rajan, *Diamond Anvil Cell High Pressure Powder X-Ray Diffraction System for Materials Research* (IGCAR Report No. IGC-153, 1993).

[11]   R. Deivasigamani, N. Gunasegaran, N. Easwaran, M. Yousuf, K. V. Thomaskutty, P. C. Sahu, N. V. Chandra Shekar, N. Subramanian, and K. Govinda Rajan, in edited

Indus-2 synchrotron facility has a beam current of 200 mA at which experiments are carried out. A collimated beam of 100 μm was used to carry out the X-ray diffraction of the materials loaded in the Mao-Bell type DAC. The alignment of the DAC with respect to the incident beam was carried out remotely using area X-ray diode detector. Most of the HP-XRD experiments, discussed in this thesis, were carried out at beamline -11 & 12 in angle dispersive and transmission mode. Diffraction data have been collected on a 2D-mar345 dtb -image plate and analyzed using Fit2D image processing software [72]. The resolution of the detector gives accuracy in the interplanner spacing of the materials up to the third decimal place.

FWHM of the focused beam is ~130 mm and the flux is ~15.5×10^6 photon/sec at 50 kV and 1 mA. The details of this unique experiments are discussed in Chapter 3.

2.4.2 Synchrotron Source XRD technique

The combination of high Flux, high brilliance, high stability, fine vertical collimation of synchrotron radiation along with the advantage of the broad spectrum as compared to conventional laboratory X-ray sources, makes it an ideal source for XRD characterization of materials. Most of the high-pressure studies (at ambient temperature) discussed in this thesis have been studied using synchrotron X-ray source at Indus-2, RRCAT, Indore, India. Indus-2, a 2.5 GeV synchrotron radiation source, is a booster cum storage ring where electrons are injected into it at 550 MeV and accelerated to 2.5 GeV. Figure 2.8 shows a schematic of Indus Accelerator complex.
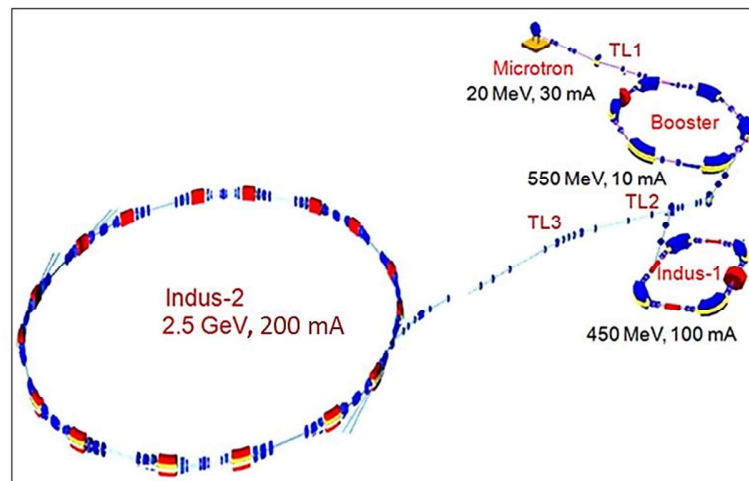
Figure 2.8: *Schematic of the INDUS working. TL represents transfer line through which electron beam is transported to another ring.*

Figure 2.7: *Rigaku ULTRAX18 (18 kW) rotating anode X-ray generator loaded with Mao-Bell type DAC*

During the high-pressure study, the X-ray diffraction pattern is collected on a 2D image plate. mar345 dtb image plate was used for our experiments [72,73]. It gives resolution of 0.001 Å. Part of the high-pressure studies of the materials in the thesis were carried out using this Rigaku ULTRAX18 (18 kW) rotating anode X-ray generator. Methanol: Ethanol: Water (MEW) has been used in the ratio of 16:3:1 as a pressure transmitting medium in all the high-pressure studies at ambient temperature.

High Pressure-High Temperature X-ray diffraction studies have been carried out using a novel custom designed-combination of membrane cell DAC (discussed above) coupled to a high flux micro-focus X-ray machine (of M/s XENOCS, France) [23]. Molybdenum target was used which results in X-ray of wavelength 0.711 Å. The X-ray multilayered mirror optics focuses intense monochromatic beam at the focal spot. The

72

have been in use to study the materials inside the DAC. In this thesis, X-ray Diffraction technique have been used extensively and will be discussed here in detail.

X-ray diffraction study is the best method to probe structurally into the materials inside the DAC as diamonds are fully transparent to the X-ray and unlike neutrons diffraction, very small quantity of sample is enough for X-ray diffraction which can be easily loaded in the DAC. X-ray diffraction study in the DAC has to be carried out in the transmission mode wherein the X-rays pass through the diamond anvils and the sample squeezed between them. The sample between the anvils diffracts the X-ray according to the Bragg's law $2d\ sin\theta = \lambda$. For HP & HP-HT experiments in the thesis, angle dispersive mode has been adopted wherein monochromatic beam of X-ray was used. Two kinds of X-ray sources have been used for HP diffraction study. Both of the X-ray sources have its own merits and demerits and are discussed here.

2.4.1 Laboratory source based X-ray Diffraction technique

X-ray beam obtained from a Rigaku ULTRAX18 (18 kW) laboratory-based rotating anode X-ray generator was monochromatized with a graphite monochromator which gives Mo Kα radiation with wavelength 0.7107Å [figure 2.7].

To allow the X-rays to pass through the sample in the DAC, a collimator of ~100 μm opening (internal-slit) has to be installed in the piston of the DAC through which the X-ray passes. The collimator is to be aligned such that X-ray passes through the center of the culet of the diamond anvil. The alignment is carried out using an X-ray photographic film which when exposed to the X-ray gives the position of the X-ray path in the DAC.

black body that emits black body radiation when heated i.e. assuming the hot surface emissivity to be 1. The measurement of the temperature is mainly affected by the wavelength dependent emissivity which is also assumed to be constant (if not known at high P & T conditions) in the calculation. Due to this spectroradiometric approximations and assumptions, a maximum error of 10 % can appear in the temperature estimation [54,55].

2.4 Techniques to probe the material inside the DAC

Diamond being transparent to large portion of electromagnetic spectrum, enables probing the materials inside the DAC. There are several techniques which are discovered to explore the various material properties viz. lattice, electronic and optical properties etc. at high pressures. Higher generation synchrotron facilities at a later stage added to the area of research. X-ray diffraction and Raman Spectroscopy are the major probes to study materials under pressure which give a boost to geophysicists to study minerals [56,57]. Some of the other probing technique such as: X-ray absorption spectroscopy -to determine the local and electronic structure of matter [58–60], Phonon Inelastic X-ray Scattering Spectroscopy-to estimate elastic tensor and dispersion in phonon modes [61], X-ray inelastic near edge spectroscopy –to probe chemical bonding [62], X-ray magnetic circular dichroism- to examine spin resolved conduction band densities and local magnetic structure [63], Electronic inelastic X-ray scattering –to probe band structure and fermi surface [64–66], Resonant inelastic X-ray scattering- to study electronic states in solids and phase transition driven by electron correlation effects that occur in f-electron based intermetallics [67,68], Crompton Scattering – to investigate electron momentum distribution [69], Transport measurement [70,71]–to determine the electrical properties,

70

Sample loading in the DAC for laser heating is very crucial from the point of absorbing the laser beam with lesser dissipation of heat. The choice of pressure transmitting medium is equally important because it may react with the sample and pressure calibrant at high temperatures during laser heating. Also, it should provide the thermal insulation between the sample and the gasket so that heat is contained to the sample only. A novel technique has been discovered in our laboratory which enables heating of the sample without raising the temperature of the pressure calibrant. It will be described in detail in Chapter 3. Various solids (NaCl, KBr), liquids (MEW), inert gases (He, Ne, Ar) have been in use as a pressure transmitting media for the laser heating. Soft solid- NaCl is easiest to load therefore it has been preferred among others for our experiments.

2.3.2 Temperature estimation techniques

There are various ways to measure the temperature inside the DAC during laser heating however, black body radiation technique (spectral radiometry technique) is mostly applicable for very high temperatures [51–53]. The technique is based on Planck's law for thermal radiation which describes the intensity of the emitted radiation as a function of wavelength at various temperatures. Temperature of the hot sample is estimated by fitting the thermal radiation spectrum (generally: 670–830 nm) to the Plank's radiation function. Wein's displacement law ($\lambda_{max} T = 2.89 * 10^{-3} mK$) is an outcome of Planck's law which states that the maxima of emitted wavelength is inversely proportional to the temperature of the black body and can also be used to estimate the temperature inside DAC during LHDAC experiment. The radiation during the experiment is collected by a collector lens and fed to the high-resolution CCD based spectrometer (Triax 500) via optical fiber. The spectrometer resolves the wavelengths. In this method, a hot sample is approximated to a

Collecting lens [figure 2.6 a]. Visible light is used to align the set up for CO_2 laser path. DAC is mounted on a x-y-z nano-mover stage which can be controlled remotely. Using the movable stage DAC can aligned with respect to the position of the focused laser beam. A photograph explaining the focusing guiding path is shown in figure 2.6. Figure 2.6 (b) shows the actual photograph of indigenously developed LHDAC set up in the laboratory.
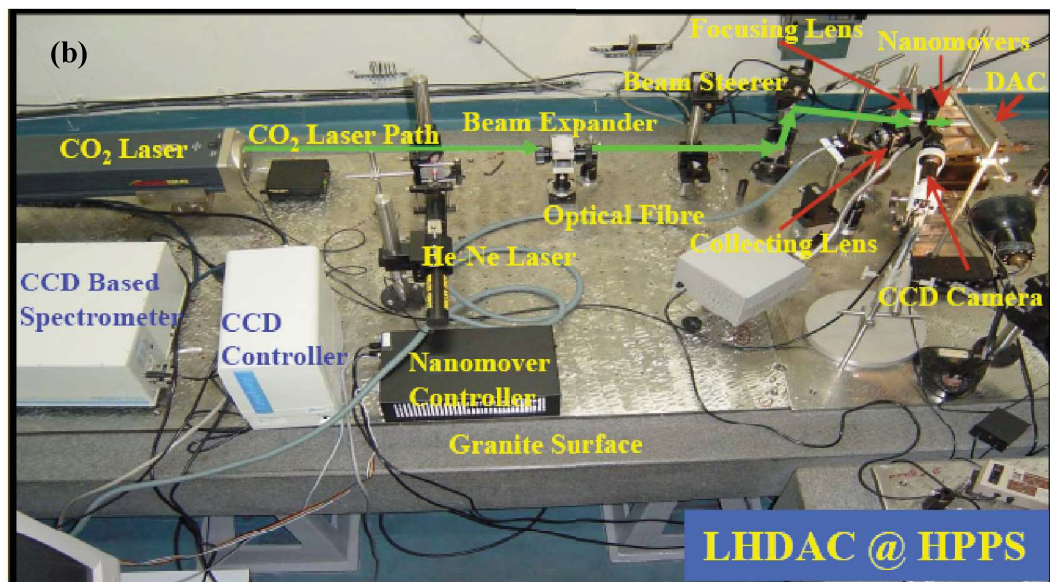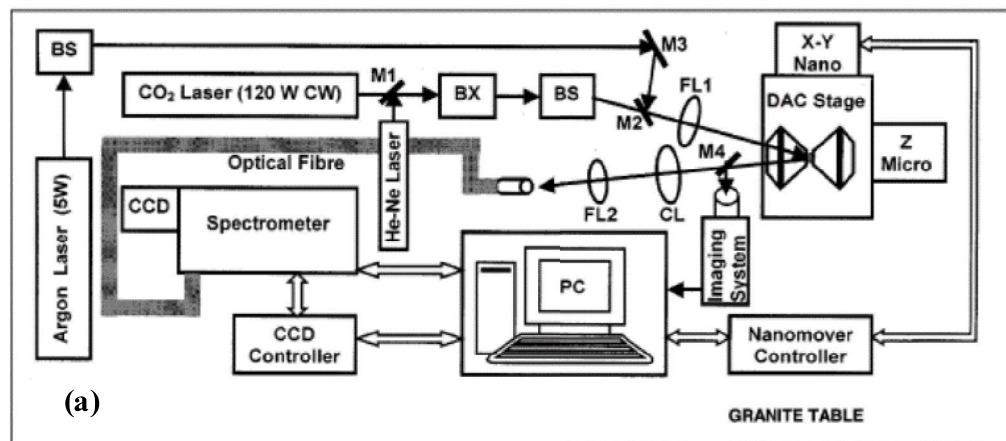
Figure 2.6 (a): *LHDAC set up [47–50] (b) Actual photograph of LHDAC in the laboratory*

K. At a later stage, a heater has also been home-built to make it cost effective and maneuverable for our experiments. The design and testing aspect of the indigenous heater are illustrated in detail in chapter 3.

2.3.1.2 Laser-Heating DAC technique

In order to overcome the achievable temperature limit and unnecessary heating of the DAC components, laser heating method is employed [43–47]. Using this technique enormous heat (temperature up to ~5000 K) can be produced in the sample chamber leaving the anvils and surroundings unaffected. Laser heating involves the heating of materials by the use of electromagnetic radiation. Diamond anvils, being transparent to the electromagnetic waves, enable to probe the sample which is squeezed between the diamond anvils. Lasers have been used as a source of focused and intense electromagnetic radiation. The energy from the laser to the sample is deposited in the form of vibrations of the lattice modes in the sample. As materials have their vibrations in the infrared region, therefore, infrared lasers such as- CO_2, YAG or fiber lasers have been used to excite these vibrations.

The schematic diagram in figure 2.6 (a) illustrates the laser heating of sample in the DAC. A laser heating facility has been developed indigenously in our laboratory [47–50]. 120 W continuous wave TEM_{00} mode CO_2 laser (λ=10.6μm) heating system is capable of generating a temperature of ~5000 K at 100 GPa. The laser beam is focused to ~40 μm (limited by the diffraction spot size $4\lambda f/D$) with the help of several optical components viz. BX-Beam Expander; BS-Beam Steerer; M1, M4 Mirror for visible; M2, M3- SI coated mirrors for CO_2, FL1- ZnSe coated focusing lens; FL2-focusing lens for visible light, CL-

2.3 Temperature generation and estimation techniques

Apart from pressure, temperature provides an additional parameter to study the materials under extreme conditions. DAC is an excellent tool in which both high pressure and high temperature can be achieved simultaneously. In this section, various ways of generating high temperature in the DAC is described.

2.3.1 Temperature generation

There are two ways in which sample can be heated inside the DAC.

2.3.1.1 Resistive heating technique

The resistive method employs a miniature resistive heater placed around the diamond anvils which provides heat to the sample assembly area, including anvils when the current is passed through it [38–42]. Diamond, being a good thermal conductor, deposits the heat directly to the sample assembly. The current supplied to the heater controls the heat produced around the anvils. Constant temperature is maintained at the sample position using a thermocouple feedback. The feedback mechanism from the thermocouple to the heater current controller regulates the temperature at the sample position. The resistive method is found to be good for temperatures up to ~1273 K. In this temperature range, temperature can be easily increased, accurately controlled by the miniature heater and the components of the DAC can withstand it. Since heat loading to the diamond may oxidize it, an inert atmosphere around the diamond anvil must be provided. This helps to prevent any possibility of graphitization of diamonds.

For studies pertaining to this thesis, a heater from M/s Almax easyLab, supplied along with the Diacell-Helios DAC was used. The heater has the capability to reach ~1273

non-linear with pressure. For our experiments, Optiprexx PLS from M/S Almax easyLab was used to measure the pressure inside the DAC. This compact system contains Ar ion laser for excitation and an inbuilt spectrometer inside a box. The spectrometer records ruby spectra from the DAC and can be seen remotely on a computer. A picture of Ruby manometer is shown in figure 2.5.
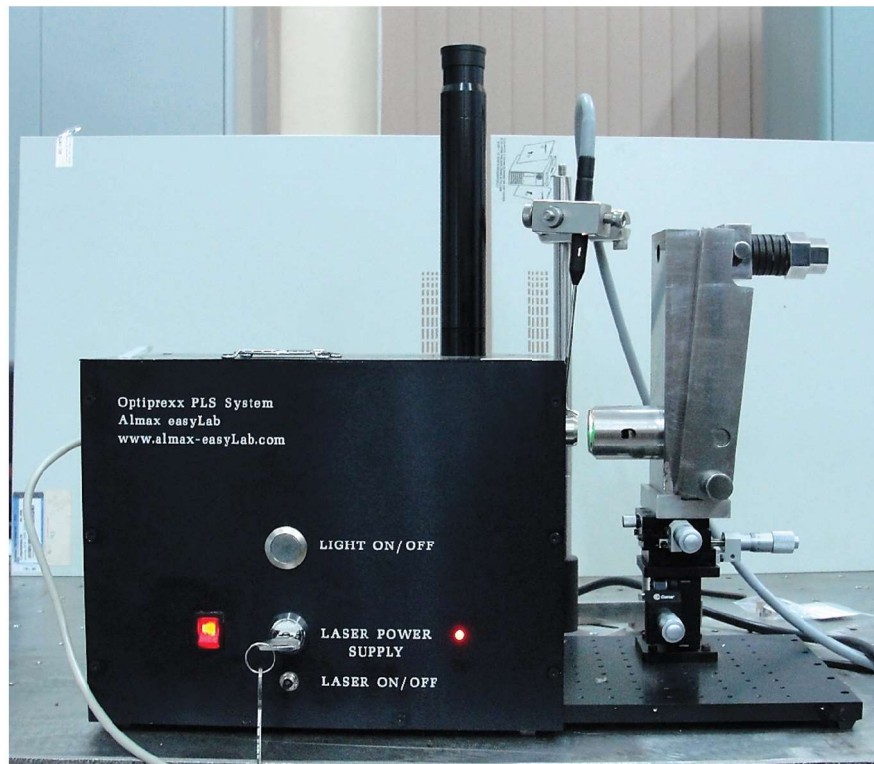
Figure 2.5: Ruby manometer used for ruby fluorescence pressure measurement

Ruby line is quite sensitive to the temperature, too, and it is found to shift linearly (0.068 nm/K) towards higher wavelength with increasing temperature [36,37]. It becomes useful while doing static *in-situ* HP-HT experiment wherein pressure is to be measured at high temperatures.

volume of the NaCl with respect to pressure has been reported by several authors at various pressure and temperatures [31,32] which has been used in HP-HT experiments to estimate pressure inside the DAC at raised temperatures.

2.2.2.2 Ruby fluorescence method

In ruby fluorescence method, a small ruby (Cr^{3+} doped Al_2O_3) chip of dia ~10-15 μm is loaded along with the pressure transmitting medium and sample. To measure the pressure inside the DAC ruby is optically excited by Ar ion laser or any other strong green and blue light source. Upon excitation, ruby emits fluorescence in the form of a doublet with wavelength 692.7 Å (R_1 line) and 694.2 Å (R_2 line). This doublet arises due to crystal field effect. These R lines of the ruby are quite strong and found to shift towards higher wavelength with increasing pressure [33–35]. These lines broaden at higher pressure due to the non-hydrostatic pressure distribution inside the sample chamber. The pressure is estimated using the following equation:

$$P(GPa) = \left(\frac{1904}{B}\right)\left[\left(1 + \frac{\delta\lambda}{694.24}\right)^{\tau} - 1\right]$$

Where τ=5 and 7.665 for non-hydrostatic and quasi-hydrostatic conditions, respectively [33]. $\delta\lambda$ (nm) is the change in the shift of the R_1 line.

R_1 line is more intense than R_2 line hence it gives more accurate pressure measurement. The pressure vs shift in the wavelength (from above equation) reveals that the pressure varies linearly as a function of $\delta\lambda$ up to 20 GPa. Hence, the simplified equation becomes P (GPa) = 2.746 $\delta\lambda$ (nm). Beyond 20 GPa the R line shift becomes

Among all, EOS and Ruby fluorescence technique are widely used for high pressure experiments. However, both the techniques have their own relative merits. Both the techniques have been routinely used in the experiments pertaining to this thesis and are described here in detail.

2.2.2.1 Equation of State (EOS) method

EOS technique works by measuring unit cell volume as a function of pressure. Change in the positions of the XRD reflections with pressure gives the knowledge of unit cell volume as a function of pressure. The reduction in the unit cell volume with pressure, of most of the metals such as Ag, Cu, Pt, Au etc. are well known which can be used to estimate the pressure through several equations of state namely Murnaghan EOS, Birch Murnaghan EOS, Universal EOS [26–30]. Transition metals with cubic structure are generally chosen as a pressure marker as they have lesser number of peaks in the X-ray diffraction pattern, hence, lesser possibility of overlap with any of the sample peaks. Also, if they are noble metals they are less likely to react with the sample and pressure transmitting medium even at high pressures. For most of the high-pressure experiments at ambient temperature, EOS method has been employed.

For high-pressure experiments at elevated temperatures, NaCl has been used to estimate the pressure and temperature in the membrane cell DAC. NaCl being a soft compound and non-reactive, has been used consistently in HP-HT experiments. It acts as a pressure transmitting medium as well as pressure calibrant at elevated temperatures. At high temperatures in the DAC, the contribution of thermal pressure is very significant, hence it must be taken into account during the estimation of pressure. The change in the

membrane. The expanded membrane pushes the piston against the cylinder causing an increase in the pressure between the anvils. Inert gas is supplied through a gas pressure controller which has an accuracy of 0.1 bar. This high accuracy of the gas pressure controller results in greater control over the pressure to be applied on the sample. The DAC is provided with a resistive heater around the cylinder diamond which can heat the sample up to a maximum of 1273 K. A novel *in-situ* HP-HT diffraction experiment using this DAC has been carried out. Details of the experiment like sample loading, pressure & temperature generation-calibration, data analysis are discussed in chapter 3.
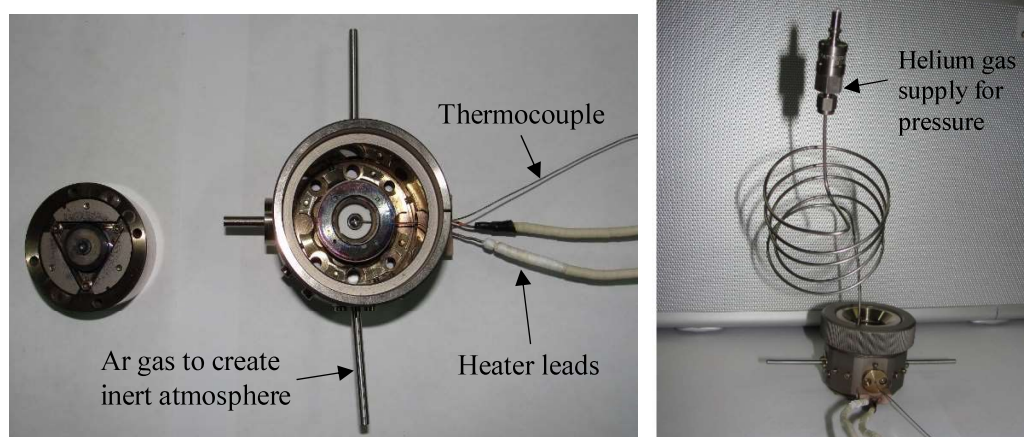
Figure 2.4: Helios Dia-Cell Membrane DAC for in-situ HP-HT studies

2.2.2 Estimation of pressure

Estimation of pressure especially at higher pressures inside DAC, had been a major challenge. There were several ways e.g. force per unit area, fixed point methods, Equation of State (EOS) methods of known compounds etc., with which the pressure was measured before the advent of ruby fluorescence technique by Forman *et al.* in the year 1972 [24,25].

Typically 16 facet-type II diamonds with culet ~500 μm, table ~2500 μm, height ~2.5 mm, and weight ~ 1/3 carat are used for high pressure *in-situ* X-ray/optical studies [16–19]. Hardened Stainless steel (SS) gasket of thickness ~300 μm has been used to contain the sample and hydrostatic pressure transmitting media between the anvils [20]. Also, it reduces the stress around the corners of the diamond. The samples under study are loaded in the holes (dia ~70 μm -300 μm) of SS gasket. To drill the holes of required size, a modified electric discharge machine has been used [21]. The development of the micro-drilling machine is described in detail in chapter 3. The indigenous DAC is designed to achieve a pressure of 100 GPa and a maximum of 80.6 GPa has been tested. Methanol: Ethanol: Water (MEW) mixture in the ratio of 16:3:1 has been used as a pressure transmitting medium in all our high-pressure experiments. It remains hydrostatic up to 14 GPa [22] and freezes beyond that leading to quasi-hydrostatic pressure distribution inside the sample chamber. This can be noticed by increase in the FWHM of the X-ray diffraction peaks.

2.2.1.2 Membrane cell DAC

Membrane cell DAC has become an excellent tool to precisely control the pressure inside the DAC. Another advantage is that the pressure is controlled remotely without disturbing the DAC giving rise to possibility of *in-situ* high-pressure experiments at high temperatures. This membrane cell DAC from M/s Almax easyLab consists of a comparatively smaller piston and cylinder wherein the diamond anvils are mechanically mounted [figure 2.4] [23]. The mounting is in such a way that it gives freedom to align the anvils by translation and tilt movements. The thrust on the piston is applied by a gas membrane. An inert gas is supplied to the membrane which leads to the expansion of

rests on tungsten carbide rocker. The assembly of rocker with diamond anvil is placed on a long detachable piston and cylinder so that the rocker position can be altered by translating and tilting which helps in the alignment of the diamond anvils against each other. The piston and cylinder are moved towards each other by Belleville spring-loaded lever arm mechanism. Application of Belleville spring avoids generation of any sudden thrust which in turn helps in a smooth increase or decrease in pressure. Also, it safeguards the diamond against any impulse. The Mao-Bell type diamond anvil cell was designed and fabricated in our laboratory and have been consistently used for high-pressure X-ray diffraction and Raman experiments [10,11]. The DAC is capable of achieving a maximum pressure of 100 GPa. The schematic and photograph of the DAC are shown in figure 2.3.
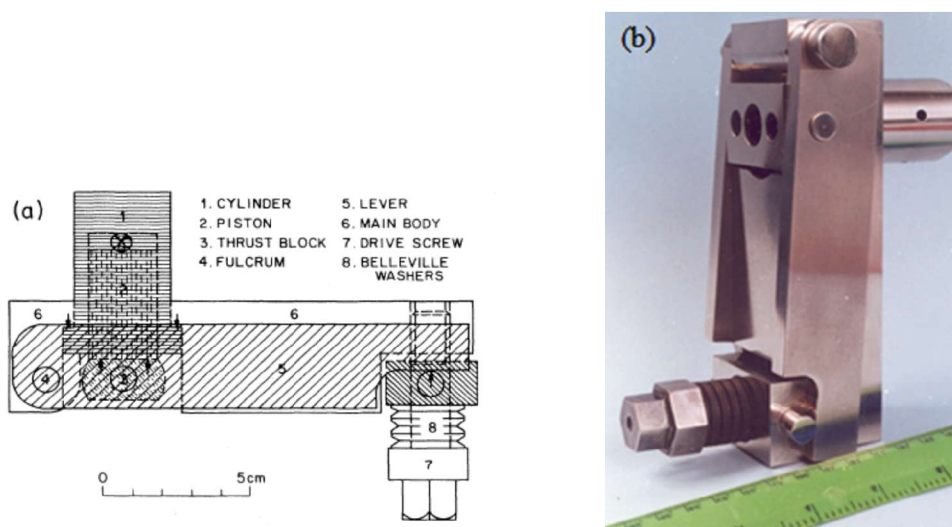
Figure: 2.3 (a) Schematic of Mao-Bell type IGCAR [10,11] cell (b) Photograph of indigenously fabricated DAC.

60

anvils. Diamond, being very hard and transparent to the electromagnetic radiation, opened new areas of study of materials at very extreme conditions.

Figure 2.2 demonstrates the working principle of DAC. A metal gasket is placed between the flat parallel faces of two opposed diamond anvils which acts as a container for the material under study along with the pressure transmitting medium and pressure calibrant.
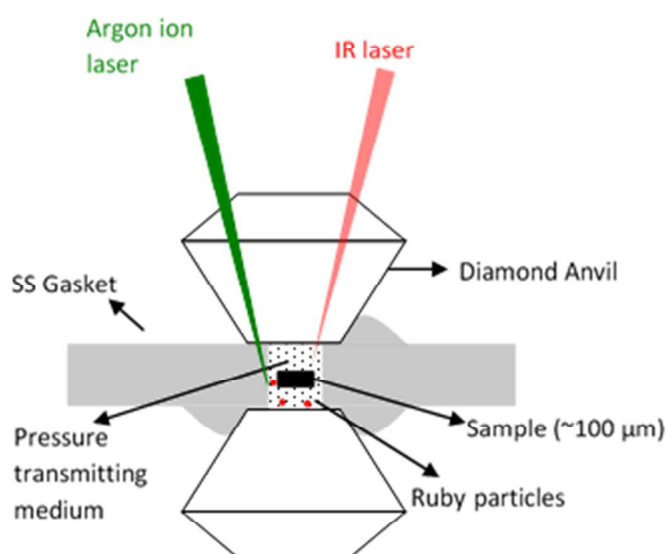
Figure 2.2: Working principle of Diamond anvils

Pressure is applied to the sample when the anvils are pushed against each other. There are various ways in which the diamonds can be pressed against each other and the DAC can be categorized by the methods of exerting pressure. Some of them, which have been used during the present thesis work are discussed here.

2.2.1.1 Mao-Bell type DAC

This kind of DAC was developed by Mao and Bell in the year 1978 [14,15]. The DAC works on the principle of 'massive support'. It employs a pair of diamond anvils which

materials can be studied. Static pressure is generated by opposed anvil technique wherein as the name suggests pressure on the sample can be held for longer duration of time (days to months). However the pressure attainability in static method is lower as compared to dynamic technique. A maximum of 640 GPa has been achieved using nano-diamond anvils [8]. Dynamic pressure can be generated by an implosion or huge impact at the sample, generating enormous pressure up to tera pascal instantly. The huge pressure at the impact point makes this impact driven pressure generation technique advantageous. The pressure generated using this method can't be sustained for more than few microseconds. This time demands that the characterization to be completed within such a short time frame. Also, the nature of dynamic technique is such that apart from generating pressure, high temperature is also realized on the sample, therefore, making it almost impossible to study high pressure properties at ambient or desired temperature.

In the present work, we have carried out experiments using static pressure which is described here in detail. High pressure is generated using the principle of force per unit area i.e. lesser the area, more the pressure. Bridgeman developed the concept of opposed anvils in the early 1900s [9]. Static pressure on the material can be applied by squeezing it between small flat surfaces of two anvils facing in opposite directions that were pressed one against the other with a lever-arm. The anvils work on the principle of massive support wherein the load is transferred from a large area (lesser pressure) to a small area (enhanced pressure) that exert the pressure on the material. However, with the advent of Diamond Anvil Cell (DAC) in the late 1950s, a new impetus originated to the high-pressure X-ray diffraction and spectroscopic research [10–13]. For the first time diamonds were used as

powders of RE_2O_3 (RE=Sm, Gd, Dy) was obtained from M/s. Sd fine chemicals, Mumbai, India. Nuclear grade U_3O_8 powders were obtained from Nuclear Fuel Complex (NFC) Hyderabad, India. These oxides in a proper stoichiometric ratio were heated at 773 K to remove moisture and further dissolved in concentrated HNO_3. Nitrate solutions of Rare Earth (RE=Sm, Gd, Dy) and uranium (U) were mixed in stoichiometric proportion (U: Sm :: 1:6). The solution was heated on a hot plate (~373 K) and urea crystals were added to the hot solution slowly. Urea (NH_2-CO-NH_2) was taken three times the stoichiometric weight of Sm and U oxides, and mixed thoroughly to the solution to enhance the reaction rate during the heating. The chemical equation of the reaction is shown as follows:

$$UO_2(NO_3)_2 \cdot xH_2O + 6RE(NO_3)_3 \cdot xH_2O + 2CO(NH_2) + O_2 \rightarrow RE_6UO_{12} + 12\,N_2\,(g) + 2CO_2\,(g)$$
$$+ 25O_2\,(g) + 2xH_2O\,(g)$$
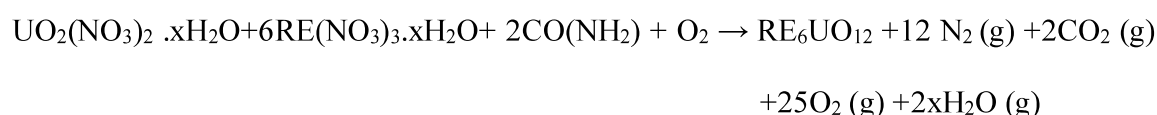
The uranyl-nitrate urea gel burned with flame/smouldered leading to the formation of a floppy mass on heating. Obtained mass was heated at 773 K for 4 h in a silica tube. The heated sample was powdered using pestle & mortar, and again heated at 1273 K for 5 h and subsequently at 1473 K for 8 h. The process of heating in air removes any gaseous or organic matter sticking to the powder.

2.2 Pressure Generation and estimation techniques

2.2.1 Pressure generation techniques

In this section, methods of production and application of high pressure are described. There exists two kinds of pressure generation techniques- static and dynamic- under which the

pump is connected to one side of the chamber which can create a vacuum level up to 10^{-3} bar. The chamber is flushed out with an inert gas then the vacuum is created. This process is repeated several times before the actual arc melting starts. The gas flushing of the chamber removes any air present and creates an inert atmosphere so that any possibility of oxidation or unwanted reaction to the materials can be prevented. The melting of tantalum metal is another precautionary measure to remove oxygen content from the chamber. The tantalum is capable of capturing oxygen and nitrogen by forming nitrides and oxides which helps to meet low oxygen pressure level. Further, the stoichiometric quantities of reactants in the form of pellets are placed in a depression (crucible) in the copper hearth. Electric arc is generated between the tungsten electrode and the metals/reactants placed in the copper hearth. Heat generated by the electric arc struck between the electrode and the metal/reactants serves to melt the metals placed in the crucible to form an alloy/compound. The arc produces a temperature as high as ~4000 K which is sufficient to melt most of the metals and alloys. First tantalum metal is melted and reactants thereafter. Repeated melting is performed to improve the homogeneity of the alloy. The melted ingots are annealed to obtain the desired phase.

2.1.2 Sol-Gel method

Sol-gel is well-known chemical solution method for preparation of a variety of the materials especially oxides. It has an advantage due to its flexible nature. The materials discussed in chapter 6 have been synthesized using this method. In the synthesis procedure, urea combustion technique was followed in which oxide solutions act as a precursor and urea as a reaction rate controller [1–7]. Uranium oxide U_3O_8 and RE_2O_3 were selected as starting materials for the preparation of rare earth uranate. The analytical reagent grade

air or in vacuum depending upon the reactivity of the starting materials with atmospheric gases at high temperatures. Generally, metallurgical samples have high melting points and hence are well suited to be prepared using this method. In the present work, Arc-melting technique has been used to prepare all the samples studied in Chapter 4 and 5.

The method involves melting of the starting reactant material using the heat generated by electric-arc. Sharp tungsten rods and copper hearth are used as electrodes and the whole assembly is placed inside a chamber in such a way that both are accessible from outside through their extended portions [figure 2.1].
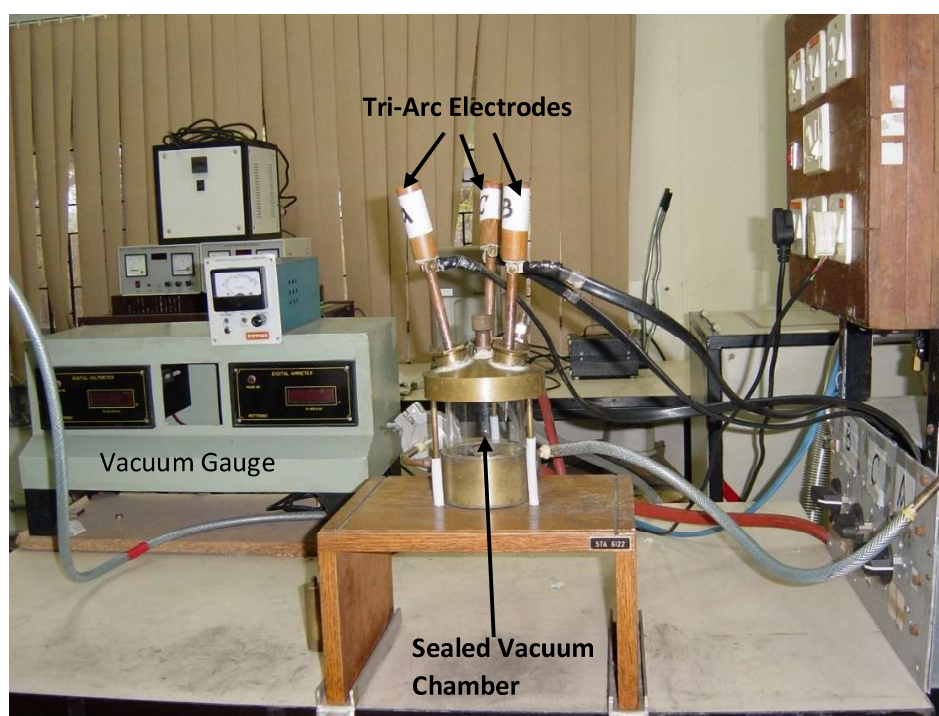
Figure 2.1: *Arc-melting technique*

The electrodes are connected to a high power DC current source which supplies current to the electrodes. A chilled water supply cools down the chamber walls. The rotary vacuum

2.1.1 Solid State reaction method

This is the most widely used method for synthesis of polycrystalline samples. As solids do not react at ambient temperature, high temperature is generated for the reaction to take place. In this method, starting materials react chemically at higher temperatures without any solvent. It can be further divided into two categories: Calcination and vacuum arc-melting technique.

2.1.1.1 Calcination technique

This method can be used to prepare a large number of compounds. Calcination technique is mostly employed for thermally robust non-volatile materials in which bulk solids are prepared using resistive tube furnaces or induction heating furnaces. Modern ovens can achieve temperature as high as 2273 K. In this method, reactants in the form of fine powder are mixed together in proper stoichiometry and pellets are made from the mixture. Fine powder is used to increase the surface area of the reactants. Then pellets are subjected to high temperature which is required to induce diffusion between the reactants. The temperature depends upon the reactivity of the reactants and kinetics of the reaction. Generally, solids are not raised to their melting point, so reactions take place in the sub-solidus state. Since very high-temperature furnaces (>1473 K) are expensive and difficult to handle, therefore, this technique is generally preferred for materials with lower melting points.

2.1.1.2 Vacuum Arc-Melting technique

This method is employed for reactants having high melting points. It involves melting of the reactants together thereby forming the compound or alloy. The melting can be done in

Chapter 2

Experimental techniques

===

This chapter describes various equipment, tools and methods used in this thesis to prepare samples and to carry out high pressure & high pressure-high temperature X-ray diffraction experiments onto them.

2.1 Sample Preparation techniques

Synthesis of high-quality material is of the utmost importance in experimental condensed matter physics. Proper preparation of compound/alloy to determine its content, strain and crystal structure requires that a rigid step-by-step process is followed. In sequence, the steps include purity checking, sectioning, polishing, etching, microscopic examination followed by melting or chemical reaction of the constituents. Specimens must be kept clean and preparation procedure carefully followed in order to obtain accurate phases. Given the diversity of solid state compounds, diverse array of methods are used for their preparation. Several methods like Solid State Reaction (SSR), Co-precipitation, Sol-Gel, Pulsed Laser Deposition (PLD), Chemical Solution Deposition (CSD), Physical Vapor Deposition (PVD), Chemical Vapor Deposition (CVD), Sputtering, Flux Growth Technique etc. are available for synthesis. Solid State Reaction method and Sol-Gel have been employed in this work to prepare the uranium intermetallic and oxide compounds, respectively. These two methods are also popular from solid state chemistry point of view and are described here in detail.

[11]   B. Shukla, N. R. Sanjay Kumar, M. Sekar, N. V. Chandra Shekar, H. Jena, and R. Asuvathraman, J. Alloys Compd. **672**, 393 (2016).

[12]   O. L. Anderson, Oxford Monogr. Geol. Geophys. **31**, 405 (1995).

[13]   B. Shukla, N. R. Sanjay Kumar, M. Sekar, and N. V. Chandra Shekar, J. Instrumentaion Soc. India **46**, 75 (2016).

[14]   Z. Du, L. Miyagi, G. Amulele, and K. K. M. Lee, Rev. Sci. Instrum. **84**, 24502 (2013).

[15]   C. S. Zha and W. A. Bassett, Rev. Sci. Instrum. **74**, 1255 (2003).

References

[1]   D. Lonappan, N. V. Chandra Shekar, L. M. Sundaram, T. Edwin, and P. C. Sahu, in *AIP Conf. Proc.* (2011), pp. 461–462.

[2]   B. Shukla, N. V. Chandra Shekar, N. R. Sanjay Kumar, T. R. Ravindran, P. Sahoo, S. Dhara, and P. C. Sahu, J. Phys. Conf. Ser. **377**, 12014 (2012).

[3]   H. Di Xiao, H. L. Ma, C. S. Xue, H. Z. Zhuang, J. Ma, F. J. Zong, and X. J. Zhang, Mater. Chem. Phys. **101**, 99 (2007).

[4]   A. Khan, S. N. Khan, W. M. Jadwisienczak, and M. E. Kordesch, Sci. Adv. Mater. **1**, 236 (2009).

[5]   H. D. Li, S. L. Zhang, H. B. Yang, G. T. Zou, Y. Y. Yang, K. T. Yue, X. H. Wu, and Y. Yan, J. Appl. Phys. **91**, 4562 (2002).

[6]   N. Subramanian, N. V. Chandra Shekar, N. R. Sanjay Kumar, and P. C. Sahu, Curr. Sci. **91**, 175 (2006).

[7]   A. M. Schaeffer, S. R. Temple, J. K. Bishop, and S. Deemyad, Proc. Natl. Acad. Sci. **112**, 60 (2015).

[8]   P. Toulemonde, L. Laversenne, P. Bordet, M. Legendre, O. Leynaud, and A. Prat, Proc. LIth Eur. High Press. Res. Gr. Meet. London (UK), 1–6 Sept. 2013 **34**, 167 (2014).

[9]   K. Vinod, V. S. Malik, S. K. Sharma, and S. K. Srivastava, J. Phys. Chem. Solids **68**, 32 (2007).

[10]   D. L. Decker, J. Appl. Phys. **42**, 3239 (1971).

The details of the experimental procedure are described in Section 3.3. The temperature vs supplied current plot [figure 3.13] shows higher values of temperatures from the fabricated heater as compared to the imported heater for the same current, which is an indicative of the better performance of the indigenous heater as higher current values lead to the melting of the coils and contacts. Also, no corrosion on the indigenous heater was noticed.

It can be seen from the plot that the kanthal strip heater performs better than the heater made of kanthal wire. No corrosion was found on the heater after several rounds of heating. Therefore, the kanthal strip filament has been considered for testing inside the Helios DAC. To take the leads from the filament stainless steel leads of dia ~ 0.9 mm are welded using a CO_2 laser. The filament is kept between two circular alumina sheets and then squeezed between two pyrophyllite disks. The assembly is locked with the help of two SS locking plates from both bottom and top. Then, the heater assembly has been installed in the Helios DAC. A HP-HT experiment on CdZnTe was carried out up to ~2 GPa and ~1000 K to test the functionality of the Kanthal heater within the DAC. XRD plots using a micro-focus X-ray generator from M/s Xenocs, France, as described earlier, has been recorded at various temperatures inside DAC and are shown in figure 3.13.
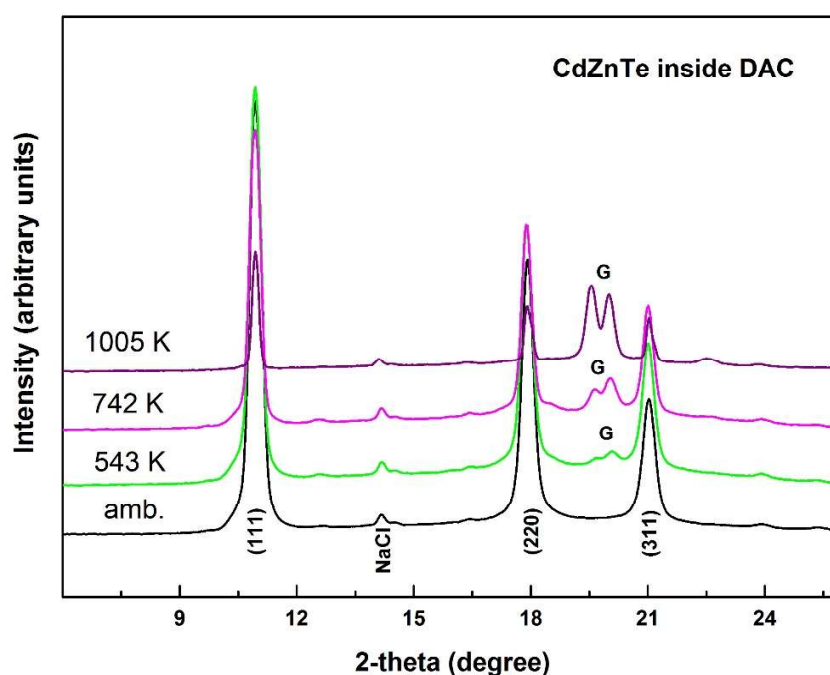
Figure 3.13: *HP-HT XRD plots of CdZnTe at various temperatures. 'G'-represents gasket peak in the diffraction plots*

101

(a) **(b)**
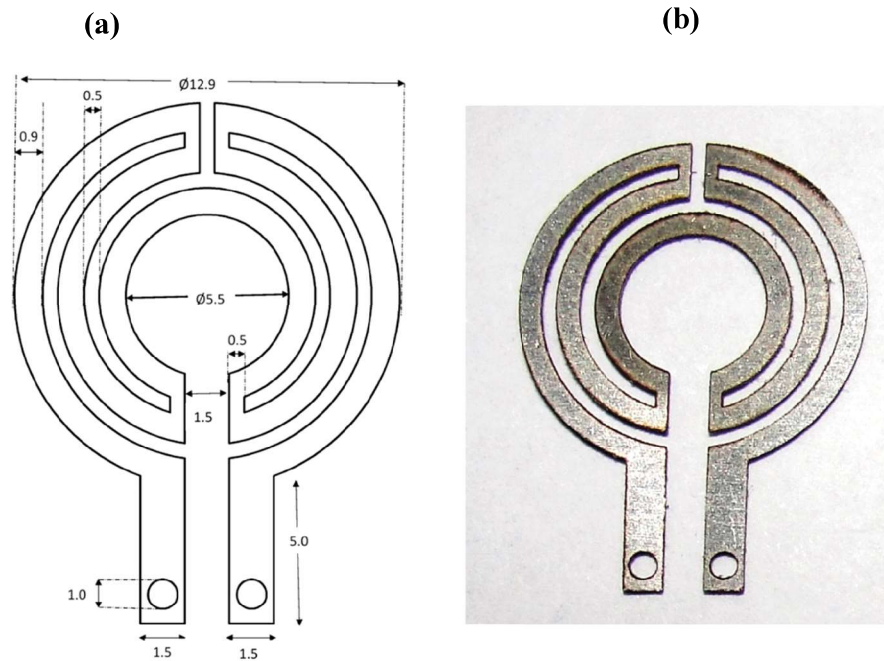
Figure 3.11: *Make 3 Heater assembly (a) Diagram of final filament with dimensions (b) Laser cut kanthal filament*
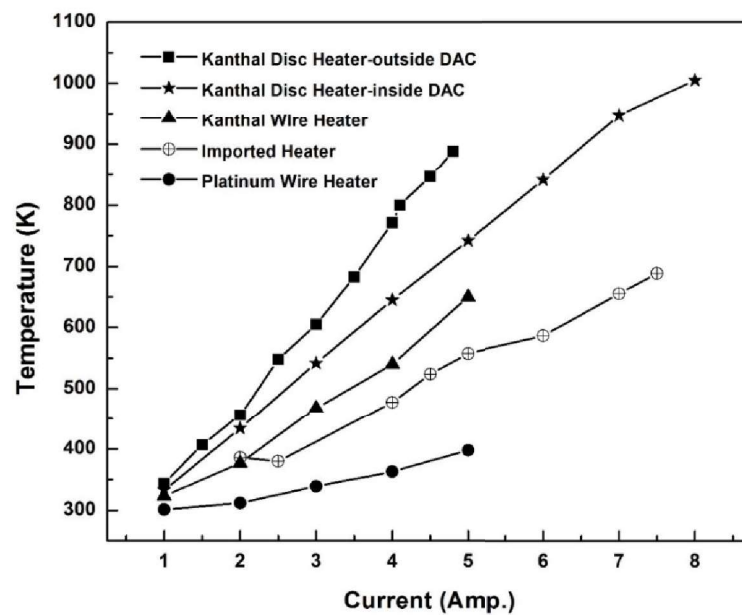
Figure 3.12: *Comparision of performances of various heaters*

100

material as it achieves a higher temperature at lower current due to its high resistivity. Repeated heating test runs were performed using both the materials and are found to be reproducible. Kanthal is known for its corrosion resistant properties during heating. Therefore, it is decided that kanthal material can be used for DAC heating experiments. Also, Make-2, heater assembly confirms the length of wire to be 8 cm to generate the required temperature inside the DAC.

As Make-2 heater assembly winding is fragile and doesn't have provision for gasket resting onto it, therefore, an advancement which satisfies all the desired criteria, was required and heater in the form of a flat coil has been proposed. The diagram of which is shown in figure 3.11 (a). AUTOCAD software has been used to design the filament. To fabricate the filament, two kanthal strips of thickness 1.5 mm are cold rolled at IIT, Hyderabad. One strip is rolled to a thickness of 0.25 mm and another is rolled to 0.20 mm. Different thickness has been chosen so as to vary the resistance of the coil. Finally, the filament was cut from the strips using a laser cutting machine at Laser Development & Industrial Applications Division, RRCAT, Indore. The power of the CO_2 laser has been optimized to cut the kanthal material to the required thickness. Figure 3.11 (b) shows the final filament. Several sets of filaments are made using the laser cutting machine. The resistance of the filaments are measured. The filament of thickness 0.25 mm gives a resistance of 1.4 ohm, however, the filament of thickness 0.2 mm gives a resistance of 2 ohm. In comparison, the imported disc type heater has a resistance of 0.8 ohm with a thickness of 0.3 mm. The current vs temperature data for Kanthal strip heater inside DAC, Kanthal strip heater outside DAC, Kanthal wire heater, and platinum wire heater are plotted in a single plot in figure 3.12 for comparison.

A current source was used to supply the current to the heater and temperature was recorded at the center of the heater using a thermocouple. The maximum temperature recorded is 923 K which meets temperature requirement for further studies. However in the above configuration, the heater will have significant thickness due to wrapping around the pyrophyllite disk. This may lead to the transfer of heat to diamonds. Therefore, further modification in the design has been considered and grooves on one side of the surface of pyrophyllite are made as shown in figure 3.10.

Figure 3.10: *Make-2 Heater assembly, Groves in the pyrophyllite disc for the flat heater configuration*

A filament wire is inserted in the grooves and finally closed with a similar pyrophyllite disc. This assembly is tested in the same manner using the same current source and temperatures have been recorded. Platinum and kanthal wires have been used to test the flat heater design and functionality of the material and it has been found that Kanthal is better

2. Space constraints: Since space around the anvil in the DAC is limited, the wire length that could be accommodated in the proposed flat heater assembly has been estimated to be 8 cm. The length has been calculated for making three turns of coil in the filament.

3. The entry point of the thermocouple: For temperature estimation in the sample chamber, the thermocouple must touch the diamond. Therefore, a gap is required in the heater filament to accommodate the thermocouple wire.

To meet the requirements a provisional testing was carried out using a pyrophyllite disc with grooves in the form of the coil winding onto it. Figure 3.9 demonstrates the model heater on which kanthal wire of length 8 cm is wound. The whole assembly was wrapped in glass wool to insulate it from the atmosphere.
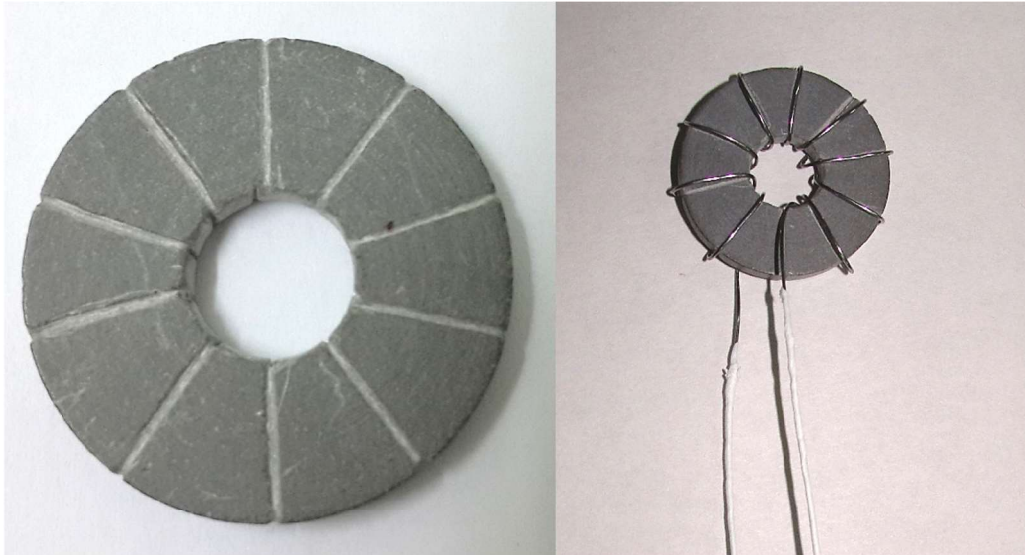
Figure 3.9: Make-1 heater assembly

of the present thesis work, a heater which can be reused several times with ease and less heat load on the diamonds, has been designed and developed. The development process consists of several stages. Some of them are discussed here in detail.

The choice of the material for the miniature heater which can go to high temperatures becomes important especially in the constraint of space. There are variety of materials available *viz.* precious metals (Platinum and Platinum-Rhodium Alloys), metallic alloys (Nickel-chrome, Iron-Chrome-Aluminum, Tungsten, Molybdenum, and Tantalum), ceramic metals (Molybdenum Disilicide, Lanthanum Chromite), ceramic materials (Silicon Carbide, Zirconium Oxide), and graphite-based materials etc. for use as heating elements. However, a material which could be operated at high temperatures in the presence of oxygen was needed for the resistive heating in DAC. Tungsten, molybdenum, tantalum, and graphite are the materials which cannot be used for heating in air. Therefore, precious metals and metallic alloys are chosen for testing of high-temperature miniature heater and hence, platinum and kanthal wires, which do not oxidize in air, are tested for their capabilities to reach 1073 K in air. To test the materials, the design of heater coil is also required to be explored. For the design aspect the following criteria become important from the point of view of their location inside a DAC.

1. Heat load on the diamonds: Heater must be designed to deposit heat directly to the gasket than to the diamond anvils as it may graphitize at higher temperatures. Therefore, the coil must be very near to the gasket which is possible only when a coil is in the form of a disc and placed near to the gasket.

To perform the HP-HT XRD experiment, the powdered sample is pelletized and a small chip of dia ~150 μm is cut from the pellet. The sample along with NaCl is loaded in 70 μm thick SS gasket, having 250 μm through hole which is mounted on the cylinder of the DAC. The culet diameter of the diamonds is 600 μm. Since NaCl has high compressibility it functions as a pressure transmitting medium. Also, NaCl functions as pressure calibrant and pressure is estimated using EOS of NaCl. The equation of state and thermal expansion behavior of NaCl at HP-HT is discussed extensively in the literature [9,10,12]. NaCl reflection in HP-HT XRD gives the value of the pressure inside the DAC.

In summary, as a part of this thesis a very useful laboratory-based HPXRD technique has been established using a combination of micro-focus, sealed tube based X-ray machine and a membrane type Diamond Anvil Cell (DAC) [13]. This technique has been proven to be equivalent to HPXRD experiments performed utilizing rotating anode based X-ray sources.

3.4 Design and development of a miniature-Heater for Helios DAC

As discussed in section 3.3 resistive heater was employed around the diamonds to heat the sample enclosed in the SS gasket of DAC. The whole assembly of the heater and the membrane DAC have been imported from a firm- M/s Almax easyLab. In view of high cost of the heater and less durability, it is essential to design an indigenous miniature heater to serve the same purpose. Indigenous product designed in the laboratory generally provides more maneuverability in access and control. Also, the native technologies are cheaper as compared to the imported ones. Therefore, a miniature heater has been designed and fabricated which is compatible with Helios DAC. Several reports on the design of an internal resistive heater exist in the literature [14,15]. With this back ground and as a part
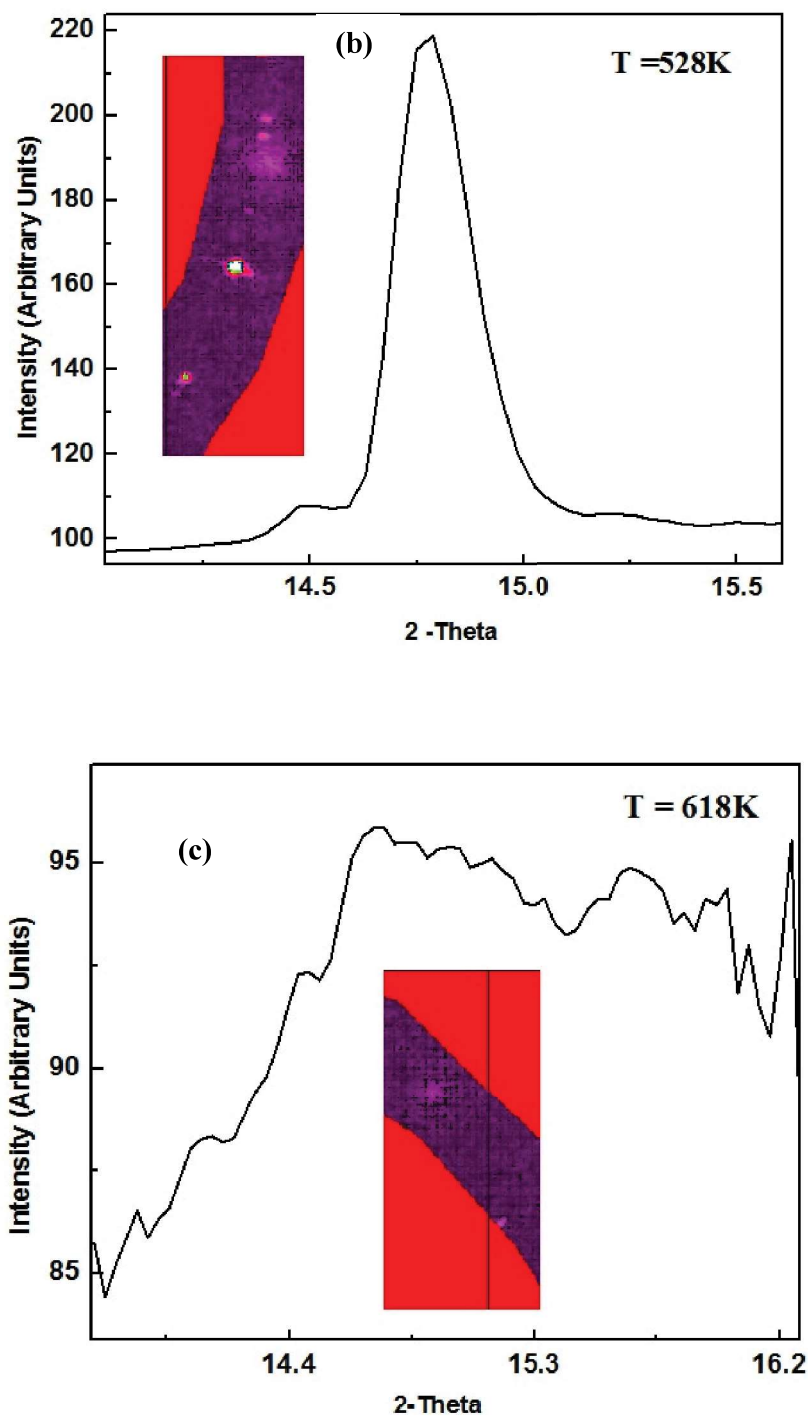
Figure 3.8: *X-ray diffraction pattern of NH₄Cl **(b)** the dotted pattern shows the nucleation of the phase near the melting point-528 K **(c)** disappearance of the pattern reveals the melting point of the compound at 618 K.*

Another validation of the thermocouple reading was done using fixed point method *i.e.,* monitoring the melting point of NH_4Cl and $AgCl$ at ambient pressure. For this NH_4Cl, which has a melting point of 611 K, has been loaded in the DAC and temperature is raised slowly up to 611 K. Near the melting temperature, a spotty diffraction pattern has been observed indicating nucleation of the grains in the material. At 611 K of the thermocouple reading, no peaks in the diffraction pattern were observed [Figure 3.8 (a, b and c)]. Since, diamond is a very good thermal conductor, the thermocouple reading and temperature reading from the sample chamber are found to be the same.

The first high pressure-high temperature experiment was carried out on Dy_6UO_{12} [11] which will be discussed in detail in chapter 6.
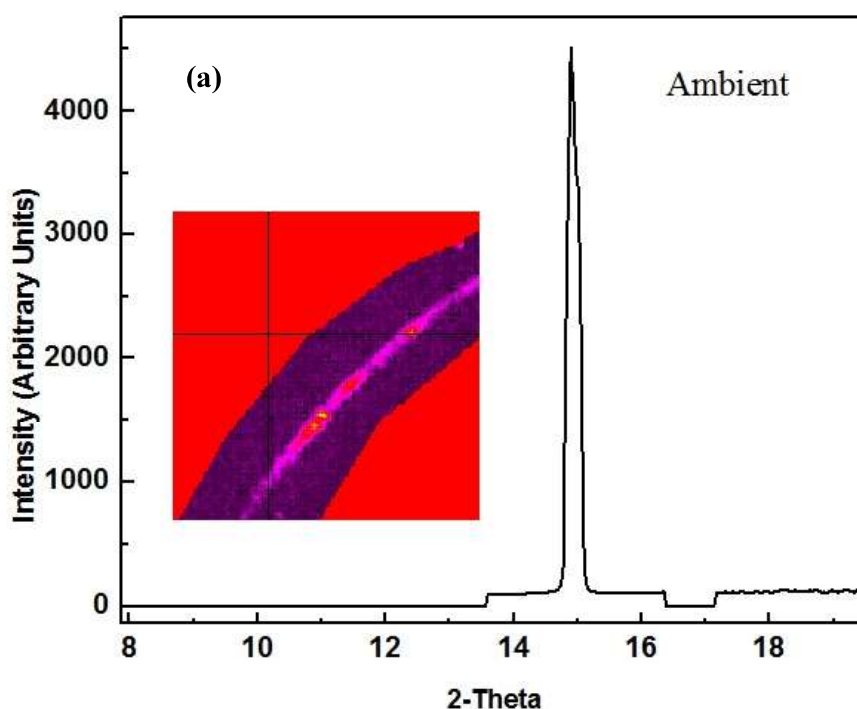
Figure 3.8: *X-ray diffraction pattern of NH$_4$Cl **(a)** at ambient*

93

in the path of the X-ray from the generator to cut any stray portion of the X-ray beam. Also, it ensures the passage of X-ray beam only through sample region avoiding the gasket peak. Angle-dispersive X-ray diffraction technique has been adopted to collect X-ray diffraction data on mar345 image plate detector in transmission mode. The image plate is kept on a guiding track which can be moved back and forth in order to get more degree of freedom on the resolution of the Bragg peaks.

As the sample and the thermocouple are spatially separated, the thermocouple is calibrated by comparing the temperature reading of thermocouple with the equation of state of NaCl and KCl [9,10]. The variation of NaCl Bragg's peak gives the values of the temperature present inside the chamber. Figure 3.7 shows the HP-HT XRD plot of NaCl at 1 GPa and 473K.
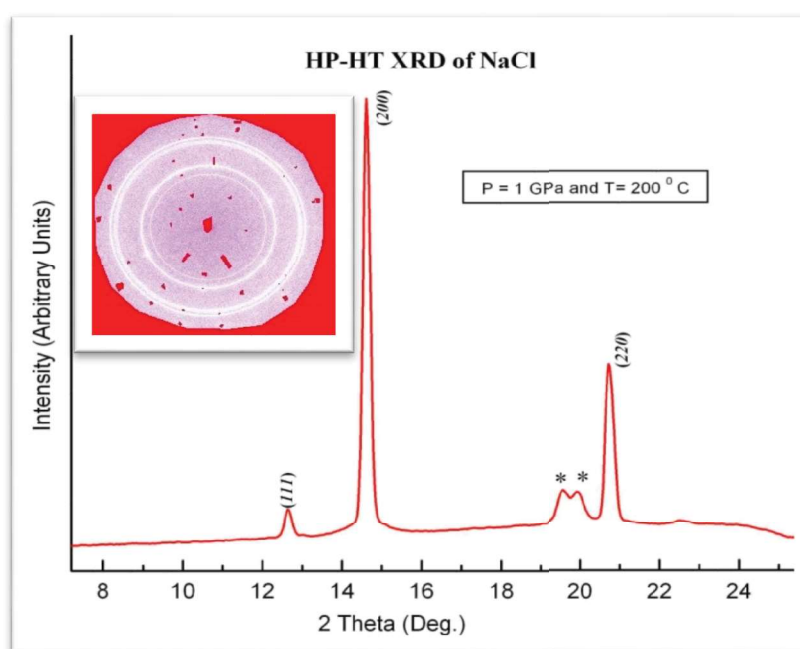
Figure 3.7: *The X-ray diffractogram of NaCl at HP-HT, '*' represents Gasket Peak*

deliverable flux is ~ 15.5×10^6 photon/sec @ 50 kV and 1 mA i.e. provides flux equivalent to the rotating anode generator with the consumption of just 50 W of power. Another salient feature of the X-ray generator is its sealed tube which makes it maintenance free.

Diacell-Helios DAC has been chosen in combination with the high-flux X-ray generator for HP-HT experiments. The DAC is designed to achieve 25 GPa and 1273 K simultaneously which is enough to study variety of compounds. The DAC is a gas membrane driven i.e. pressure inside the DAC is controlled by supplying helium gas to the membrane placed inside the DAC. The pressure inside the DAC is controlled by a gas pressure controller which not only provides a remote control of the pressure inside the DAC but also ensures accuracy in the control of the pressure. A pressure calibration as a function of gas pressure has been carried out using the EOS of NaCl and KCl as the pressure-temperature data of these materials are already reported in the literature [9,10]. The resistive heating method has been employed for heating the sample. The heater in circular form is placed inside DAC around the diamond anvils. For insulation mica is placed around the heater from all sides so that it does not get in contact with the DAC. Temperature is estimated using thermocouple placed in contact with cylinder diamond. The temperature is controlled using a current supply which works on the feedback mechanism from the thermocouple and it provides a good accuracy (± 0.1 K). Helios membrane DAC is equipped with mica on both the sides of DAC -along the X-ray path- to thermally insulate it from the environment. Inert, reducing gas (Ar + 2% H_2) is allowed to flow inside the DAC at a very low flow rate of ~15-18 sccm to avoid tarnishing and oxidation of the DAC surface due to heating. Diamond anvil cell is installed on a motorized stage which can be moved along x-y-z and theta axes remotely. A slit of ~100 μm is placed close to the DAC

91

pressure X-ray diffraction facility. The most common facilities are rotating anode X-ray generators which are difficult to maintain with magnetic seals, vacuum systems, and elaborate cooling systems. Here, we describe a customized set-up wherein a sealed tube along with the membrane cell DAC, is utilized to perform HP-HT X-ray diffraction experiments. Recently, Toulemonde *et al* (2014) have described an experimental setup, wherein a Paris-Edinburgh cell was employed to carry out *in-situ* HP-HT experiments [8]. Although this kind of cell can use large sample but it is limited to lower pressure range. Figure 3.6 shows the photograph of custom designed micro-HP-HT XRD set up.

Figure 3.6: *Novel set up of micro-focus XRD attached with membrane cell DAC*

Here, the sealed tube X-ray generator with X-ray multi-layered mirror optics (GENIX 3D supplied by M/s Xenocs, France), delivers intense monochromatic Kα beam at small focal spot having X-rays of wavelength 0.711 Å. The waist size of the X-ray beam was measured to be 130 μm at a focal length of 25 cm. Also, it provides a focus depth of 2 cm. The

Raman spectra before laser heating contains modes at 273 cm^{-1}, 430 cm^{-1}, 574 cm^{-1} and 737 cm^{-1}. After laser heating all the modes of GaN disappeared along with appearance of new modes at 201 cm^{-1}, 358 cm^{-1}, 449 cm^{-1}, 483 cm^{-1} and 780 cm^{-1}. All the Raman modes observed after laser heating can be ascribed to the conversion of GaN to Ga_2O_3 under HP-HT conditions in the presence of moisture. It shows the completion of the reaction in one of the chamber and pressure can been measured accurately using ruby in another chamber (no *in-situ* measurement). Hence, the experiment demonstrates that LHDAC HP-HT reactions/sample preparations can be carried out and pressure can be measured separately using pressure calibrant/ruby in another chamber.

By above experiments, we have established the usefulness of two-chamber experiment which is meant to avoid any possibility of interference between sample under consideration and pressure calibrant so that we can successfully heat only the sample and avoid the interference coming from ruby. Further, twin chamber technique can also be used for optical studies of the sample when the spectra of sample and pressure calibrant overlaps. This technique can also be used to study two samples- a reference sample and an actual sample under HP-HT conditions. The technique has been used by Schaeffer *et al.* [7] who studied the superconducting phase of Li at high pressures.

3.3 A novel Micro-focus High-Pressure High-Temperature X-ray diffraction technique

In spite of the availability of brilliant X-ray sources at synchrotron sources worldwide, laboratory-based X-ray sources are still very important for two main reasons: (i) quick and easy accessibility (ii) availability for longer duration without competition. For a high-pressure researcher, generally, it is important to have access to laboratory-based high-

89

that pressure of the sample chamber (GaN-chamber 1) can be measured independently from ruby in another chamber (chamber 2). Also, the possibility of reaction between ruby (Cr doped Al_2O_3, a probable source of oxygen) and sample is averted. The experiment demonstrates that LHDAC experiment can be performed in one of the chamber without affecting ruby or any other pressure calibrant in another chamber.

In another experiment, NaCl with moisture content, without heat treatment, was loaded with GaN and ruby in separate chambers. The Raman spectra before and after laser heating are shown in Fig 3.5.
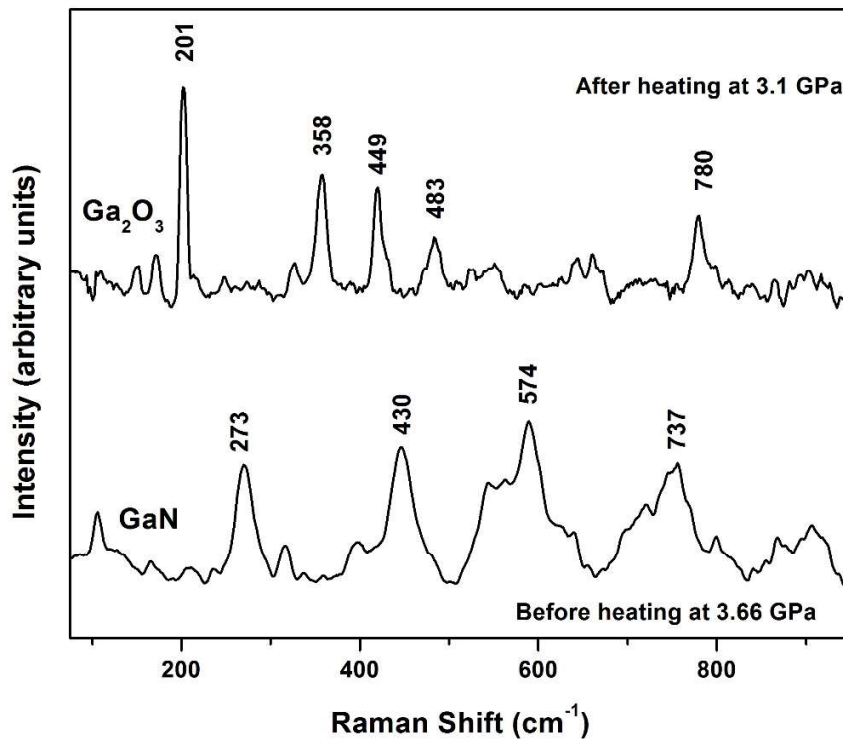
Figure 3.5: *Raman modes of GaN before heating and after heating. Complete transformation to Ga_2O_3 is seen in the top most pattern. Bottom spectrum is before heating and the top most spectra is after laser heating in moisturized NaCl [4,5].*

heated in the presence of oxygen [3–5]. NaCl was chosen as a pressure transmitting medium and was pre-heated before loading in both the chambers for up to 3 hours to remove any moisture. Afterwards, GaN was squeezed in between NaCl in one of the chambers (say chamber 1) and ruby in another (say chamber 2). The pressure correlation in both the chambers has already been established which shows that pressure in chamber 1 and chamber 2 are the same during the experiment, provided the holes are made equidistant from the center of the culet. Micro-Raman spectrum of GaN in chamber 1 before heating certifies the existence of wurtzite structure at ambient pressure and temperature. The cell was pressurized and the pressure was measured from the ruby chip in chamber 2, giving pressure to be ~3 GPa. Laser heating was carried out for ~10 min and the temperature was estimated to be ~2000 K [6]. Figure 3.4 shows the CO_2 laser heating of GaN inside DAC.

GaN being heated by CO_2 laser

Ruby in other chamber
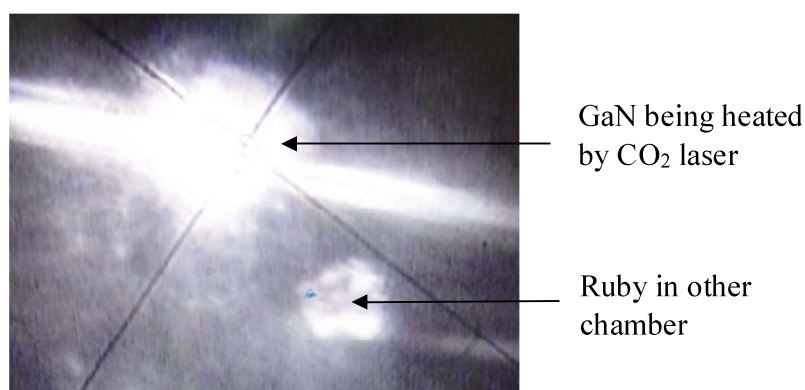
Figure 3.4: *Laser heating of the GaN in one of the chamber and ruby present in another chamber*

Raman spectra of the laser heated sample do not show any change with respect to the spectrum of GaN obtained before heating. The reason for not observing oxide formation was due to the inert atmosphere present in the sample chamber. The experiment confirms
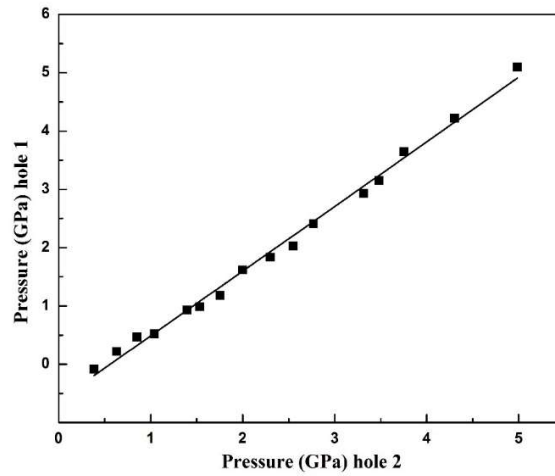
Figure 3.3*: Pressure correspondence in two holes of the gasket*

It was seen that the pressure reading is approximately same up to 6 GPa, (Figure 3.3) as ruby chamber centers are equidistant and particles are placed at the center of the hole. Two chamber experiment with the same set up was tested up to 15 GPa and found to be working. However, at high pressures, there are more chances for the sample chambers to get deformed leading to dissimilar pressure in both the chambers. Therefore, this process is well suited for the low-pressure experiments.

Two sets of HP-HT experiments on gallium nitride have been carried out to validate the two-chamber technique. The validation was done on the following points:

1. LHDAC experiment can be performed in one of the chamber without affecting pressure calibrant (ruby) in another chamber.

2. Sample Preparation/reaction in both the chambers can be performed independently.

GaN is III-V semiconductor and exists in wurtzite crystal structure at ambient [3]. It is known to show a transformation to gallium oxide at ambient pressure and 1173 K when

culet and the tail extends away from the center symmetrically up to the end of the culet. Two holes (of diameter ~ 70 μm each) have been made 'equidistance' from the center of the culet impression of the diamond so that center of each hole experiences same pressure. Modified micro-EDM [2] has been used to drill the hole in the SS gasket as discussed in Section 3.1. The schematic of the position of the drilled holes is shown in figure 3.2 a. A photograph of the actual gasket containing the two holes is shown in figure 3.2 (b).
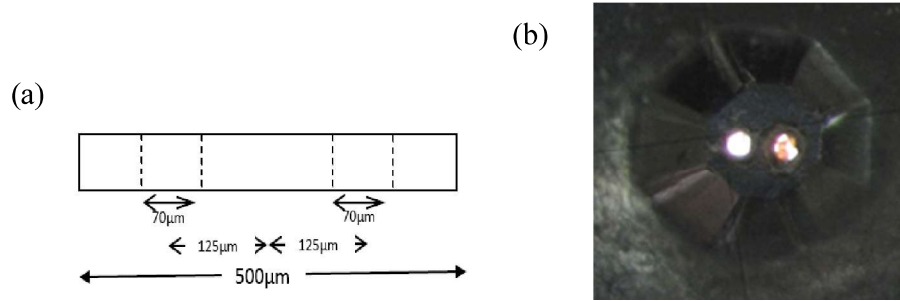
Figure 3.2: *(a) Hole positions in the culet impression on SS gasket (b) Two chamber SS gasket mounted on piston cylinder of the DAC with both the chambers filled with ruby*

To check for pressure correspondence between the two holes, an experiment with ruby particles was carried out wherein ruby particles were placed at the center of both the holes along with sodium chloride, acting as a pressure transmitting medium. The pressure was estimated using ruby fluorescence technique. Figure 3.3 shows the pressure relation in both the holes.

localized heat flux. Such intense localized heat flux leads to extreme, instantaneous and confined rise in temperature. The localized extreme rise in temperature leads to the erosion of the material. Material removal occurs due to instant vaporization of the material as well as due to melting. As the potential difference is withdrawn, the plasma channel is no longer sustained. As the plasma channel collapses, it generates pressure or shock waves, which evacuates the molten material forming a crater of removed material around the site of the spark. Due to the sudden decrease of internal pressure of the gas ball, the dielectric fluid breaks it while making the ball to implode. As a consequence of this implosion, an ejection of molten metal occurs. In the case of tungsten, since it is a hard material, the produced electric filed cannot erode the wire. For high precision applications the energy must be reduced, though it will take longer time to make hole.

3.2 Novel Twin Chamber Experiment

As explained in Chapter 2, a typical LHDAC experiment is performed using a single hole assembly in SS gasket wherein pressure calibrant is placed along with the sample. Since both the sample and pressure calibrant are not well separated, this may lead to a reaction between the sample and the calibrant at high temperatures. Moreover, if the photoluminescence of pressure calibrant and the spectrum of the sample coincide, one may not be able to carry spectroscopic studies. In order to overcome these problems, a novel technique to separate out the sample and the pressure calibrant is envisaged. The separation is done by making two holes in the pre-indented region of the same gasket. It is known that the pressure varies in a Gaussian fashion in the culet area during the high-pressure experiment. The peak of the Gaussian pressure distribution remains at the center of the

gasket, there is no force acting between them. An x-y-z stage is used for fixing the SS gasket. The positioning of the tungsten wire at the desired point is done under a microscope. Both the wire and the SS gasket are submerged in a dielectric fluid. De-ionized water is used as a dielectric. It provides flushing of the eroded particles, insulation in the gap between wire & gasket, and cooling. Depending upon the applied voltage and the gap between wire & gasket, an electric field is established. The voltage applied must be enough to create an electric field higher than the dielectric rigidity of the fluid used in the process. Electrical power is supplied to the electric discharge machine power supply through a variac transformer. The variac transformer is employed to vary the input voltage to the EDM power supply which in turn controls the discharge process. Various voltages have been tried for drilling. Higher input voltages are found not to be good for drilling as the material from the undesired spots also get eroded. Additionally, it makes uneven drilling with lots of bur on top of the SS gasket. It is due to the large electric field around the tungsten wire. However, after several tests, 45 V is found to be best suited for the drilling in SS gasket. In electrical discharge machining, the SS gasket stage is moved upwards toward the tungsten wire until the spark gap (the nearest distance between both electrodes) is small enough to ionize the dielectric. As the electric field is established between the wire and the gasket, a plasma channel is formed between them. The electrical resistance of such plasma channel is very less. Thus all of a sudden, a large number of electrons will flow from the wire to the gasket and ions from the gasket to the wire. This is called avalanche motion of electrons. Such movement of electrons and ions can be visually seen as a spark. Thus the electrical energy is dissipated as the thermal energy of the spark. The high speed electrons then impinge on the gasket and ions on the wire, creating

larger than 100 μm, is done by mechanical drilling using tungsten carbide drill bits, which is very tedious and time-consuming process. The centering of the hole is done under a microscope. Many times this process ends up in breaking the expensive drill bits and formation of burr while drilling, on top of other challenges.

To make the micro-drilling process simpler and efficient, electric discharge drilling method has been employed. A low-cost electric discharge machine (JOEMARS, Korea model no. TR 100), earlier used for tap removal, was modified for this purpose. The power supply of the machine supports voltages ranging from 100 V to 240 V with maximum power consumption 450 VA [figure 3.1] [1].

Tungsten wire electrode holder

Gasket mount

XYZ stage

EDM power supply
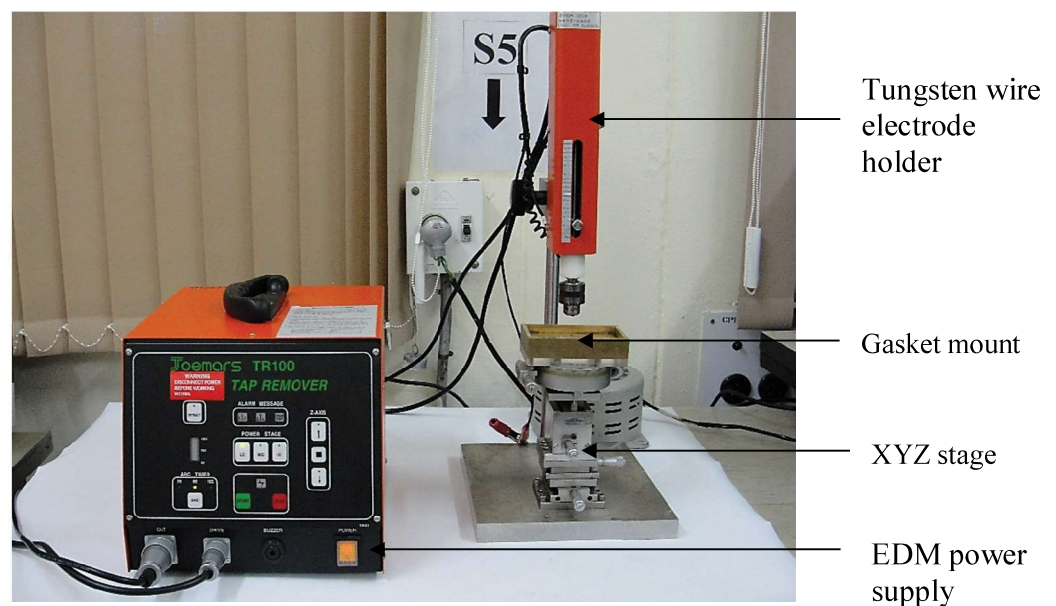
Figure 3.1: Electric Discharge Machine with drilling assembly

Micro Electric Discharge Machine (EDM) involves a thermal process. It utilizes spark to erode a conductive material. As there is no contact between tungsten wire tip and SS

Chapter 3

Development of Experimental Facilities

===

This chapter describes novel developmental activities carried out in the laboratory. It consists of four sections. Section 3.1 deals with the development of an electric discharge machine for drilling holes of various sizes ranging from 70 μm to 300 μm in stainless steel and rhenium gaskets. Section 3.2 consists of the development of a novel twin chamber Laser Heated Diamond Anvil Cell (LHDAC) experimental technique which is useful in High-Pressure and High-Temperature (HP-HT) experiments. Section 3.3 incorporates a novel combination of high flux micro-focus X-ray generator and Helios membrane Diamond Anvil Cell (DAC) for carrying out HP-HT experiments. Using this unique combination several *in-situ* HP-HT experiments have been carried out, the details of which will be discussed in the subsequent chapters. Section 3.4 comprises of an indigenous development of a resistive heater for the Helios DAC.

3.1 Development of Electric Discharge machine for drilling 70-300 μm hole

Diamond anvil cells are well suited for the high-pressure study of various samples ranging from solid substances to gases. In a typical experiment, a Stainless Steel (SS) gasket for containing the sample is prepared by pre-indenting the gasket up to 40 μm to 50 μm and drilling a hole of the desired size (~100-250 μm) for carrying out the experiments up to ~50-60 GPa using 500 μm culet diamond anvils. To attain higher pressure (>100 GPa) smaller culet sizes (100-300 μm) are used. The common method for drilling a hole that is

Heidelberg, Berlin, Heidelberg, 1985), pp. 1–56.

[15] J. P. Itié, J. Staun Olsen, L. Gerward, U. Benedict, and J. C. Spirlet, Phys. B+C **139–140**, 330 (1986).

[16] E. Wu, J. Appl. Crystallogr. **22**, 506 (1989).

[17] P. C. Sahu, N. V. Chandra Shekar, N. Subramanian, M. Yousuf, and K. Govinda Rajan, J. Alloys Compd. **223**, 49 (1995).

[18] N. V. Chandra Shekar, P. C. Sahu, N. R. Sanjay Kumar, M. Sekar, N. Subramanian, V. Kathirvel, S. Chandra, and M. Rajagopalan, Solid State Phenom. **150**, 123 (2009).

[19] J. F. Cannon, D. L. Robertson, H. T. Hall, and A. C. Lawson, J. Less Common Met. **31**, 174 (1973).

[20] A. E. Dwight, Trans. Amer. Soc. Met. **53**, 479 (1961).

[21] B. Soediono, J. Chem. Inf. Model. **53**, 160 (1989).

[22] E. R. Boyko, Acta Crystallogr. **10**, 712 (1957).

[23] J. M and Silcock, Trans. Am. Inst. Min. Metall. Eng. **209**, 521 (1957).

[24] V. E. Antonov, M. Baier, B. Dorner, A. Breidi, M. Andasmas, J. C. Crivello, O. Degtyareva, V. F. Degtyareva, M. Christensen, W. Wolf, C. Freeman, M. Akabori, T. Ogawa, A. Itoh, and Y. Morii, J. Phys. Condens. Matter **7**, 8249 (1995).

References

[1] N. V. Chandra Shekar and P. C. Sahu, J. Mater. Sci. **41**, 3207 (2006).

[2] N. V. Chandra Shekar, V. Kathirvel, B. Shukla, and P. C. Sahu, Proc. Natl. Acad. Sci. India Sect. A - Phys. Sci. **82**, 163 (2012).

[3] T. Nishioka, K. Kimura, H. Matsui, and M. Kontani, J. Phys. Soc. Japan **63**, 2722 (1994).

[4] T. Ogawa, J. K. Gibson, R. G. Haire, M. M. Gensini, and M. Akabori, J. Nucl. Mater. **223**, 67 (1995).

[5] B. Shukla, N. R. Sanjay Kumar, M. Sekar, and N. V. Chandra Shekar, J. Instrumentaion Soc. India **46**, 75 (2016).

[6] D. L. Decker, J. Appl. Phys. **42**, 3239 (1971).

[7] G. Kresse and J. Furthmüller, Comput. Mater. Sci. **6**, 15 (1996).

[8] G. Kresse and J. Hafner, Phys. Rev. B **47**, 558 (1993).

[9] G. Kresse and J. Furthmüller, Phys. Rev. B **54**, 11169 (1996).

[10] P. E. Blöchl, Phys. Rev. B **50**, 17953 (1994).

[11] J. P. Perdew, K. Burke, and M. Ernzerhof, Phys. Rev. Lett. **77**, 3865 (1996).

[12] F. Birch, Phys. Rev. **71**, 809 (1947).

[13] F. Birch, Phys. Rev. **71**, 809 (1947).

[14] J. M. Fournier and L. Manes, in *Actinides - Chem. Phys. Prop.* (Springer Berlin

High pressure and high-temperature study on UZr$_2$ shows that the material is stable up to 6 GPa and 473 K. The bulk modulus of 101.6 GPa at 473 K indicates a softening in the material at high temperatures. The lattice parameters decrease with increase in pressure at high temperatures. However, c/a ratio is found to increase. It could be due to the weakening of the partial covalent bonds between uranium and zirconium along a axis. A usual decrease in the thermal expansion coefficient with pressure is observed which are 4.6×10^{-5} K^{-1}, 3.7×10^{-5} K^{-1}, 2.7×10^{-5} K^{-1} at 1.2 GPa, 4.8 GPa and 6.6 GPa respectively in the temperature range of 300 K-473 K.

nature of bonding. Also, the covalency increases with increasing pressure. Therefore, application of pressure directly affects uranium tetrahedra and the distortions in uranium tetrahedra are responsible for the observed phase transition. Total density of state plot shows a dip at Fermi energy. Origin of pseudogap in the calculated DOS indicates new structure to be more favorable and stable at higher pressures.

High-pressure study on UOs_2 up to 35.5 GPa reveals the compound to be stable up to 12.0 GPa. Birch Murnaghan equation of state fit of pressure-volume data results in the bulk modulus of the compound to be 261 GPa. A structural phase transition has been observed between 12 GPa and 20.1 GPa wherein the compound transforms to hexagonal structure to an unknown structure with one formula unit in the cell. The bulk modulus of the high-pressure phase has been found to be 365.7 GPa which is the highest bulk modulus known till now among all the UX_2 type compounds.

Rietveld refinement on the powdered UZr_2 at ambient pressure and temperature gives the occupancy factor of Zr at position-(1/3,2/3,1/2) to be 0.84. High-pressure study at ambient temperature on δ-UZr_2 reveals that δ phase of UZr_2 is stable up to 20 GPa. Up to a pressure of 10 GPa, the c/a ratio is found to decrease slowly, after which a reduction rate increases sharply. The change in the rate of decrease in c/a ratio is attributed to the strengthening of U(1/3,2/3,1/2)$\rightarrow$ Zr(2/3,1/3,1/2) covalent bond along the 'a' axis, at higher pressures. The localization of charge density leads to a drop in the metallization of the material at high pressure which can be understood from the charge density and density of state plots where the charge is getting concentrated at each atom leaving the material to be less metallic.

Since pressure and temperature prevail together in the reactor, and UZr_2 being a reactor material, it becomes interesting to study the variation of thermal expansion coefficient at higher pressures. In the present study volume of the unit cell is found to increase with temperature at higher pressure showing the usual lattice expansion behavior. Thermal expansion coefficient has been calculated, from the first principle method, and it comes out to be $4.6 \times 10^{-5}\,K^{-1}$, $3.7 \times 10^{-5}\,K^{-1}$, $2.7 \times 10^{-5}\,K^{-1}$ at 1.2 GPa, 4.8 GPa and 6.6 GPa, respectively, in the temperature range 300 K-473 K. A decrease in the thermal expansion coefficient is a usual trend in the material at high pressure. As pressure causes a hindrance in the expansion of the material, thereby, thermal expansion coefficient drops at increased pressures.

4.5 Summary and Conclusion:

High-pressure experiments on UOs_2, UIr_2, and UZr_2 have been carried out up to 35.5 GPa, 55.0 GPa and 20.0 GPa, respectively. The bulk modulus of the compounds are found to be 261GPa, 284 GPa and 108.3 GPa at ambient pressure, respectively. $MgCu_2$ type structure compounds- UOs_2 and UIr_2 shows high bulk modulus whereas AlB_2 type compound-UZr_2 shows lesser bulk modulus.

In UIr_2 uranium 5-f electrons are participating in the bonding, giving rise to higher bulk modulus. At 40 GPa several new peaks appear indicating a phase transition. The high-pressure phase is found to have tetragonal lattice with lattice parameter $a = 6.460$ Å and $c = 10.313$ Å. DFT computation has been carried out to find the reason for phase transformation. The computational study reveals iridium tetrahedral network in the lattice to be more stable because of short Ir-Ir bonds. However, U-Ir has metallic & covalent

softening of the U(1/3,2/3,1/2)→ Zr(2/3,1/3,1/2) bond may result in the collapse of '*a*' axis with pressure at a higher temperature. Consequently, *c/a* ratio increases with pressure at higher temperatures. However, the explanation needs further confirmation through other experimental or computational evidence.

Figure 4.24 shows P-V data at 473 K. The pressure versus volume data was fitted with the 3rd order Birch Murnaghan (BM) equation of state resulting in the bulk modulus to be 104.8 GPa and 101.6 GPa at 373 K and 473 K respectively.
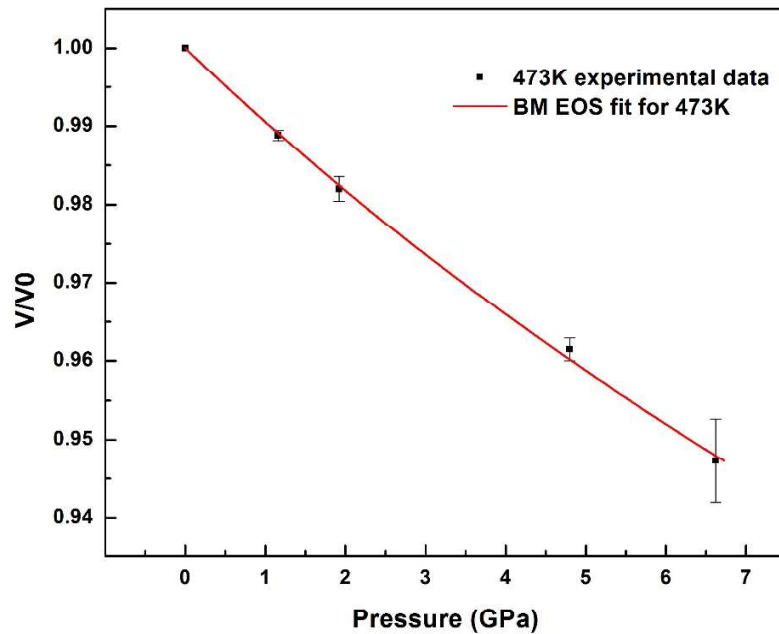
Figure 4.24: *Experimental P-V data at 473 K and 3rd order BM- EOS fit*

A drop in the bulk modulus at high temperatures signifies softening of the material. Reduced bulk modulus is due to softening of the lattice modes at raised temperatures. Apart from compressibility studies, thermal expansion behavior of the material have been studied. Thermal expansion coefficient is the parameter to define the expansion of a material which solely depends on the bond strength, packing density and compressibility.
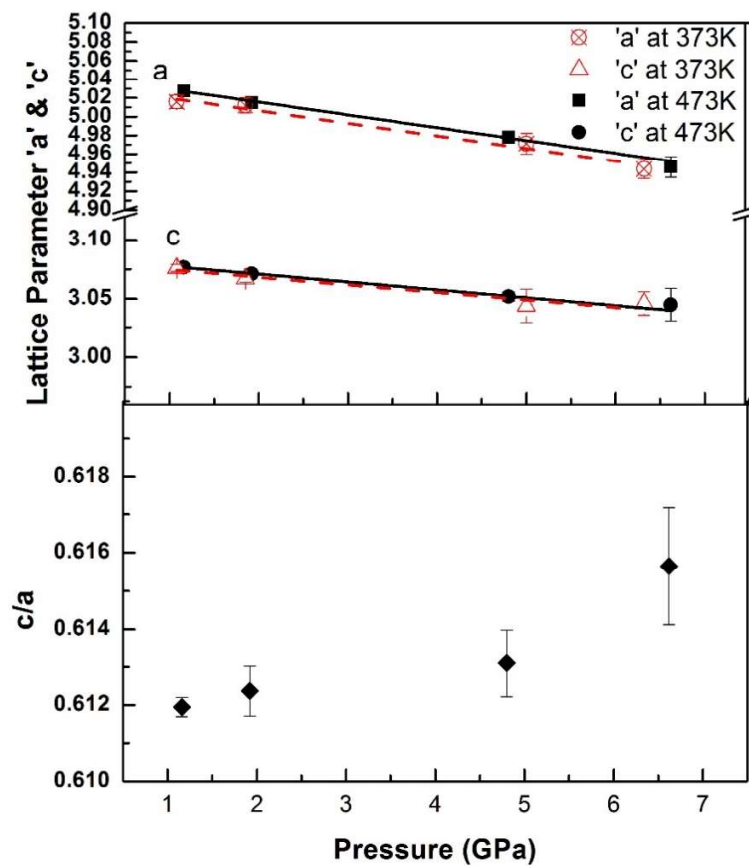
Figure 4.23: *Lattice Parameters and c/a vs P at 373K and 473K*

Diffraction data at 373 K and 473 K have been analyzed and lattice parameters at each temperature are plotted, as shown in figure 4.23. The lattice parameters are seen decreasing with increasing pressure at higher temperatures also. '*a*' parameter is found to decrease faster than '*c*' parameter, leading to an increase in the *c/a* ratio with pressure [figure 4.23-bottom]. This is again a contradictory result when compared with the *c/a* variation with respect to pressure at ambient temperature. As described earlier U(1/3,2/3,1/2)→ Zr(2/3,1/3,1/2) is covalent as well as metallic in nature and it is known that temperature causes the material to be more metallic as the number of electrons increase in the material which may lead to weakening of the U(1/3,2/3,1/2)→ Zr(2/3,1/3,1/2) covalent bond. The

hexagonal cell which is 0.612. Beyond 885 K the δ phase transforms to bcc phase which has higher atomic volume. The bcc and δ phase have Bragg's reflection at the same position except *(001)* and *(111)* peak through which the presence of δ phase can be identified.

High pressure and high temperature (HP-HT) XRD study up to a maximum pressure ~6 GPa and temperature 473 K simultaneously, have been done to study the structural behavior of the material. The XRD plots at different pressures and temperatures are shown in figure 4.22. It can be seen from the HP-HT plots that reflections *(001)* and *(111),* which particularly belong to δ structure of UZr$_2$, continue to appear and the relative intensities with the high intense reflection *(101)* do not change up to the highest pressure and temperature studied. Therefore, it can be concluded that δ structure remains stable up to 6 GPa and 473 K.
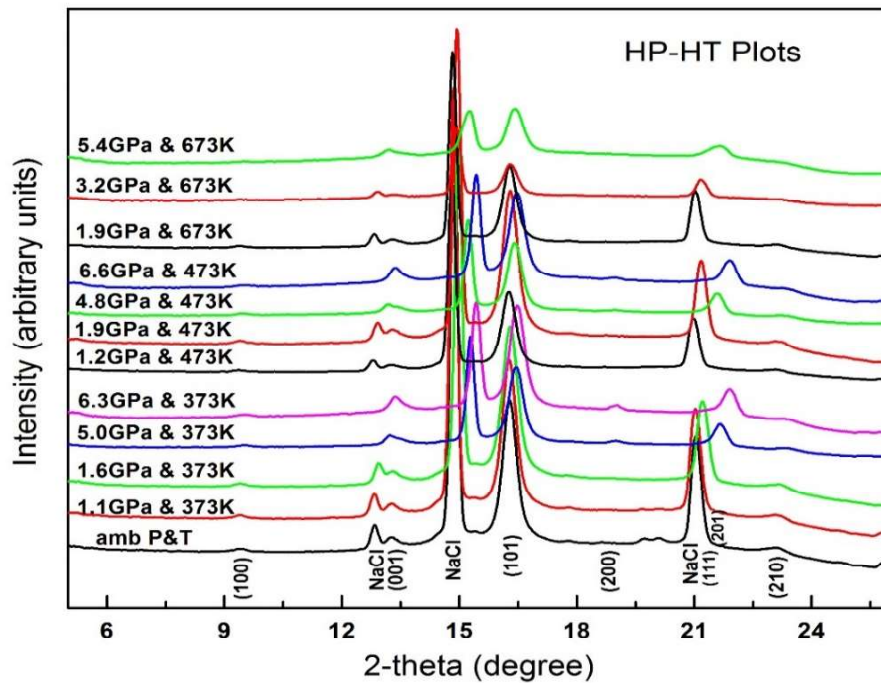
Figure 4.22: *HP-HT XRD plot of UZr$_2$*
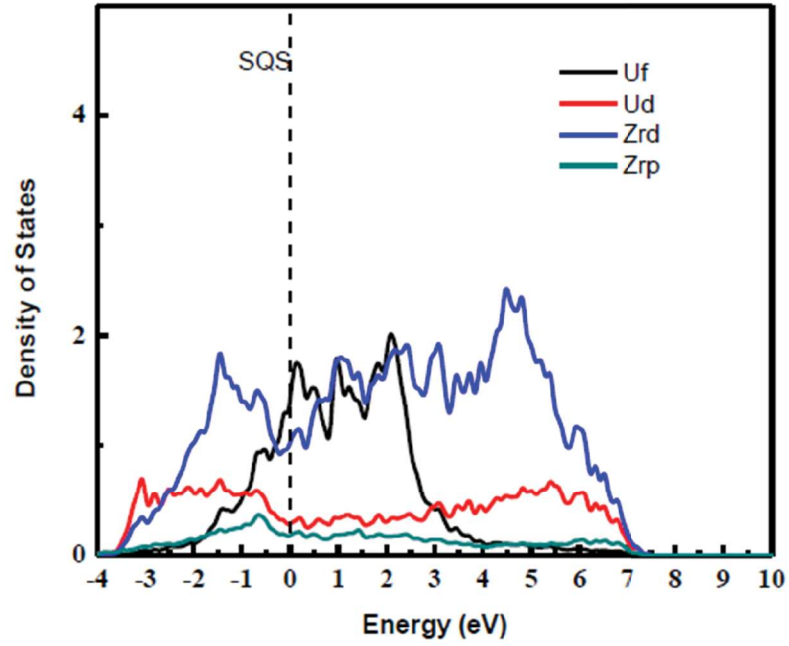
Figure 4.21: *Contribution of each atom to DOS in UZr$_2$*

The density of state plot with increasing pressure, as shown in figure 4.19, reflects a decrease in the total density of state at Fermi level indicating localization of electrons. However, after a certain pressure, the decrease in the DOS saturates [figure 4.20] and hence, electrons cannot localize more *i.e.* metallicity of UZr$_2$ cannot be decreased further. Since U-*f* electrons and Zr-*d* electrons contribute majorly to the total DOS, [figure 4.21] therefore U-*f* and Zr-*d* orbitals are responsible for the decrease in the metallicity of the system.

4.4.3.3 High-Pressure study at 293-673 K

High-temperature studies on δ-UZr$_2$ have been reported earlier [24] where temperature dependence of the lattice parameters are described up to 880 K. With increasing temperature, the *c/a* ratio decreases and above 500 K it drops below the ideal value of the

Density of state plot, computed at various pressures, are shown in figure 4.19.
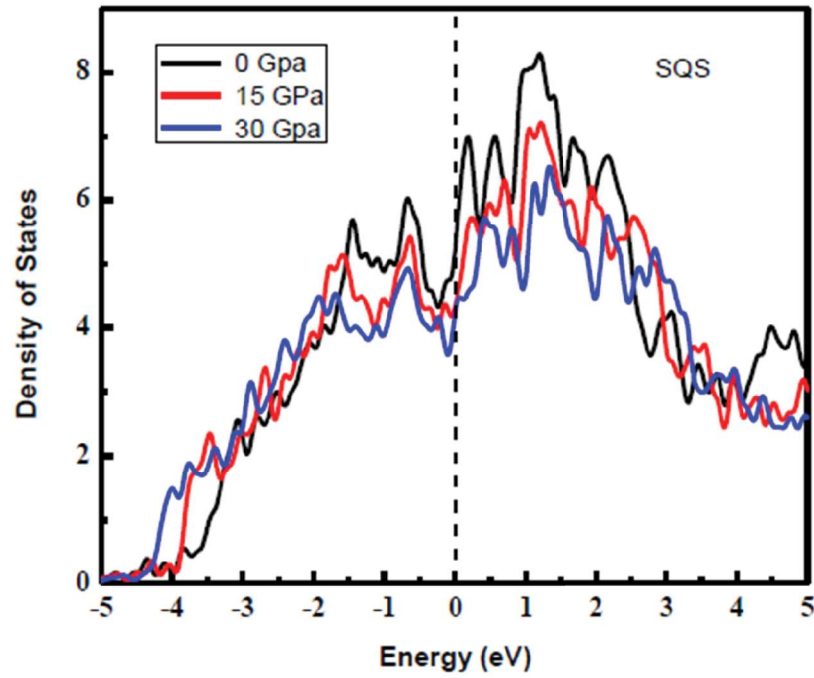
Figure 4.19: *Density of state vs Energy plot*
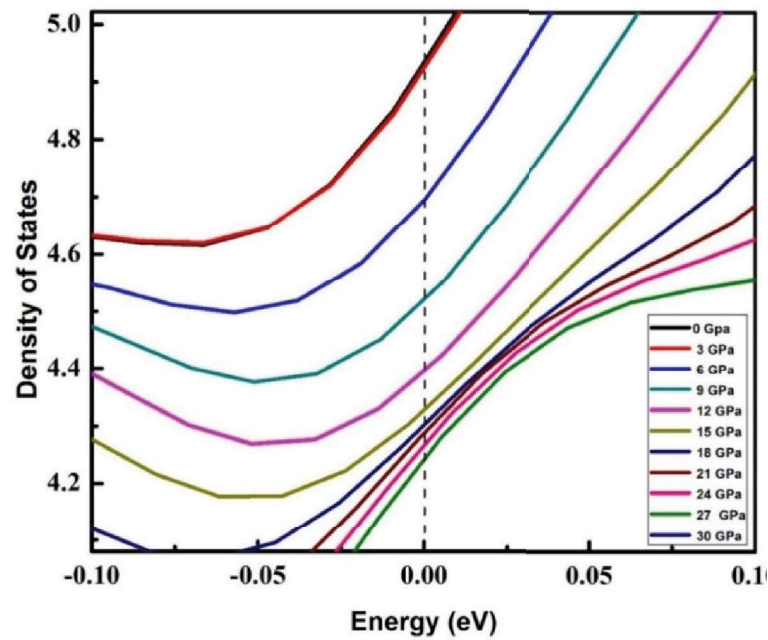
Figure 4.20: *Total density of state vs Energy plot showing saturation of DOS at high pressures*

pressure on the UZr$_2$ lattice may again lead to rapid decrease in the 'a' axis rendering slow

c/a decrease at higher pressures, but it need confirmation from HP experiments beyond 20

GPa.
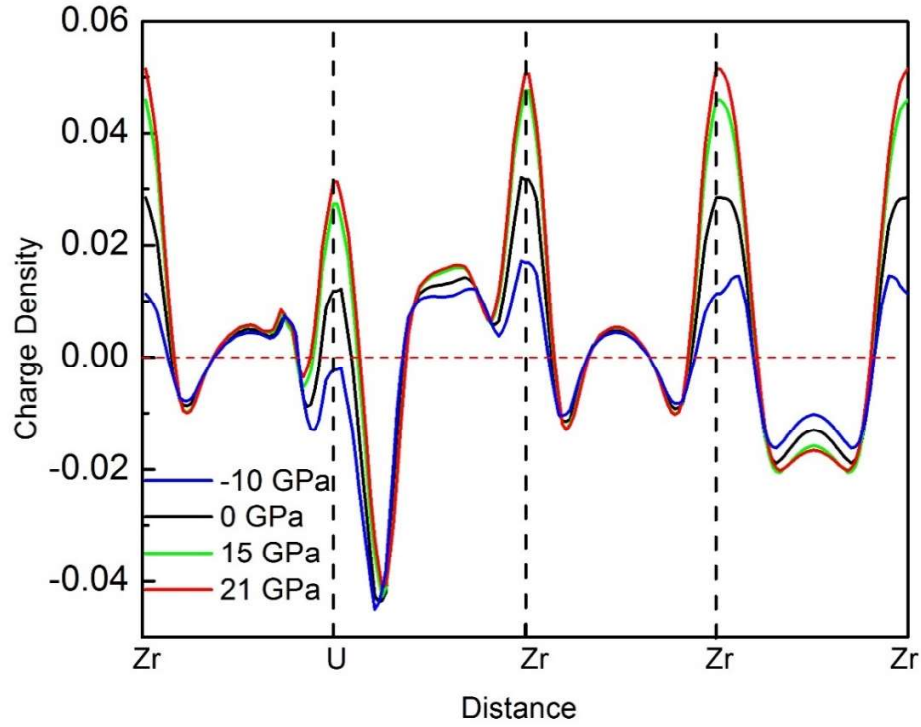
Figure 4.18: *Line charge density plot along the bonds: Zr (000)→ U(1/3,2/3,1/2)→*

Zr(2/3,1/3,1/2)→Zr (1,1,1)→Zr (0,1,1)

Another interesting point which comes out from the charge density plot is that charge gets

concentrated at each atom in UZr$_2$ with increasing pressure i.e. atoms get more localized at

higher pressure and hence the overall metallicity of UZr$_2$ decreases which is in

contradiction to the usual trend. At high-pressure generally the metallicity of the system

increases, however, UZr$_2$ shows different behavior and it becomes less metallic at high

pressures.

between U(1/3,2/3,1/2)→ Zr(2/3,1/3,1/2) bond is from 0.0109 eV at 0 GPa to 0.0155 eV at 15 GPa demonstrating an increase in the covalent nature of the bonding. Therefore, it can be concluded that at lower pressures U(1/3,2/3,1/2)→ Zr(2/3,1/3,1/2) bond is weaker hence fast decrease in the 'a' lattice parameter is seen up to 10 GPa, beyond which the bond is strongest (DFT computation) leading to a resistance in compression along 'a' axis at higher pressures.
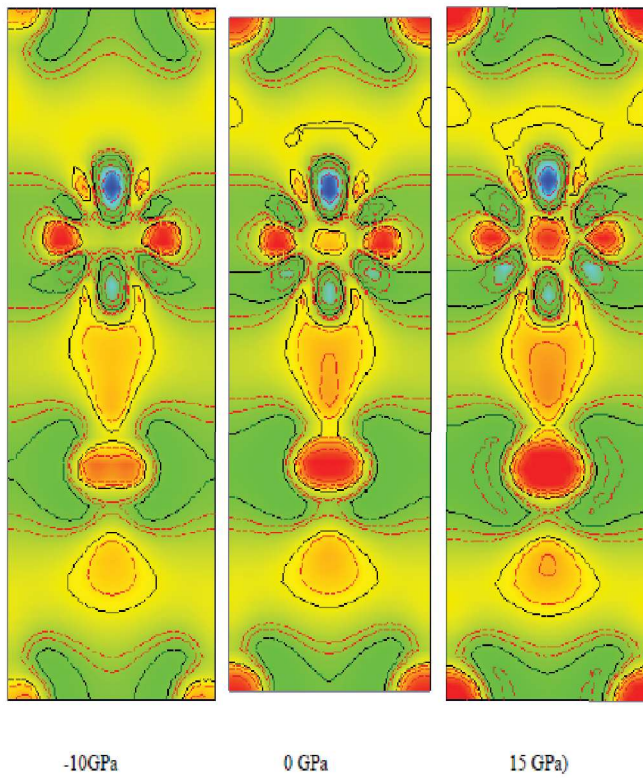
Along [110] plane
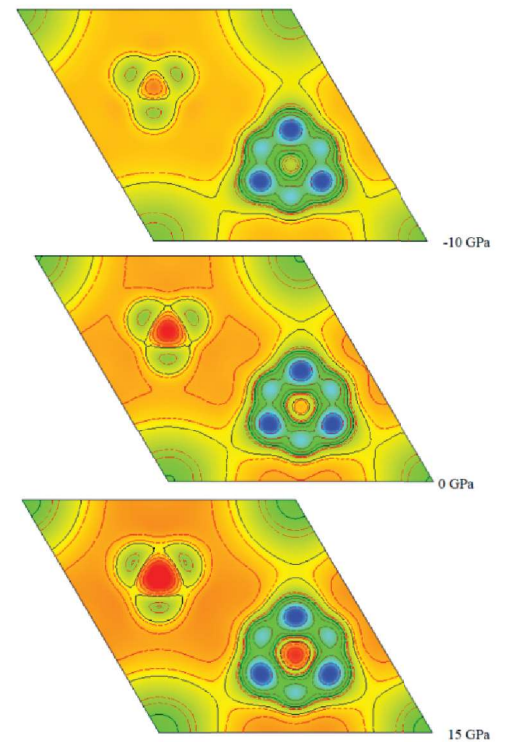
Figure 4.17: Difference charge density along (110) and (001) planes at various pressures

The line charge density plot also reveals that increase in the charge density between U(1/3,2/3,1/2)→ Zr(2/3,1/3,1/2) saturates after a certain pressure i.e. 21 GPa, and therefore the bond cannot get stronger with the increase in pressure [figure 4.18]. Hence, increased

130

From figure 4.14 it can be seen that lattice parameter '*a*' and '*c*' decrease with increase in pressure. However, the rate of decrease is different for both the axes. Axis '*a*' decreases faster than axis '*c*'. *c/a* ratio clearly reveals the relative changes in the lattice parameters '*a*' and '*c*' which can be seen in figure 4.14. The *c/a* vs pressure graph shows a very interesting behavior of lattice parameters in UZr$_2$ wherein a different rate of decrease in *c/a* have been observed. Up to 10 GPa *c/a* decreases slowly and as the pressure is increased further the rate of decrease in *c/a* increases sharply. Therefore, *c/a* vs pressure can be seen in two segments below 10 GPa and above 10 GPa. To affirm the *c/a* trend ab-initio DFT calculation was carried out wherein different slopes of *c/a* were seen under pressure [figure 4.14, bottom] which supports our experimental observation. The reason for the anomalous behavior of the *c/a* ratio lies in the structure of the unit cell. A Zr atom occupies (0 0 0) corner position of the unit cell hence the rate of change in the distance between two corner Zr atoms would be same at all the pressures and would not contribute much to the abrupt decrease in the *c/a* ratio. Therefore, the bonding between Zr and U atoms at z=0.5 position (along *a*-axis) in the unit cell may be the probable cause for the unusual *c/a* result.

Difference charge density were calculated along *(110)* and *(001)* planes at various pressures to explain the bonding nature with respect to pressure [figure-4.17, 4.18]. It can be seen that corner Zr-Zr atoms have metallic and U(1/3,2/3,1/2)-Zr (2/3, 1/3, 1/2) have metallic as well as covalent character. To quantify, line charge density was plotted along the bonds: Zr (0,0,0)→ U(1/3,2/3,1/2)→ Zr (2/3,1/3,1/2)→ Zr (1,1,1)→ Zr (0,1,1) at different pressures and it is shown in the figure 4.18. The plot shows that charge density between bond U(1/3,2/3,1/2) & Zr(2/3,1/3,1/2) increases with increasing pressure indicating an increase in the covalent nature of bonding. The increase in the charge density

modulus of the material to be 108.3 GPa. Energy-volume calculation for the unit cell is carried out to find the bulk modulus theoretically, and a plot of which is shown in figure 4.16. The Birch Murnaghan EOS fitting results in the bulk modulus of the material to be 100.4 GPa which agrees with the observed value.
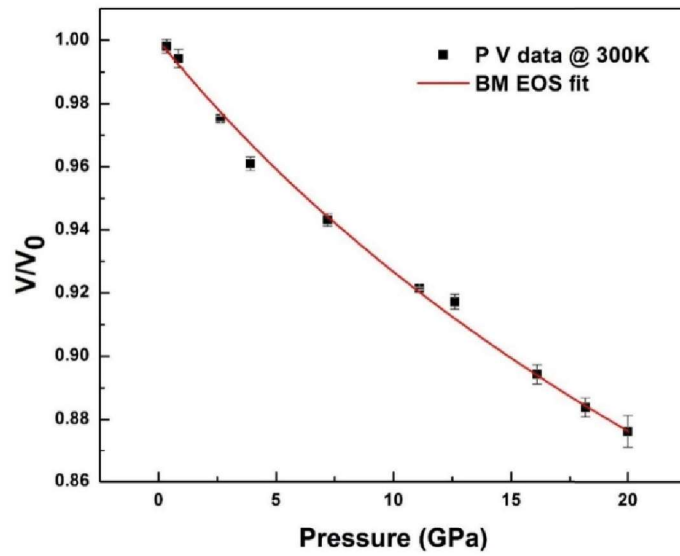
Figure 4.15: *Experimental Pressure vs Volume data at ambient temperature*
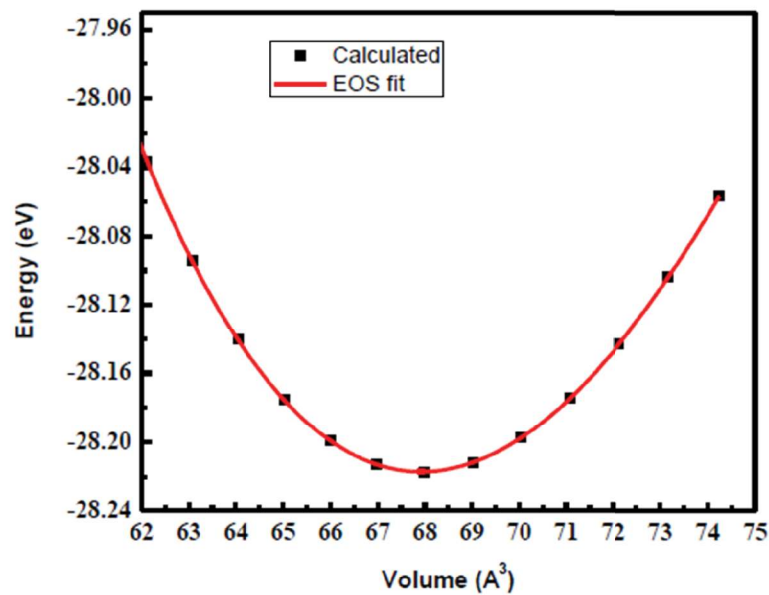
Figure 4.16: *Computational Energy vs Volume calculation*

It is seen from the diffraction patterns that the parent phase reflections can be traced up to the highest pressure studied ensuing the existence of parent δ-UZr$_2$ phase up to 20 GPa. Also, the reflections are least square fitted to the δ structure of UZr$_2$ and lattice parameters have been obtained [figure 4.14].
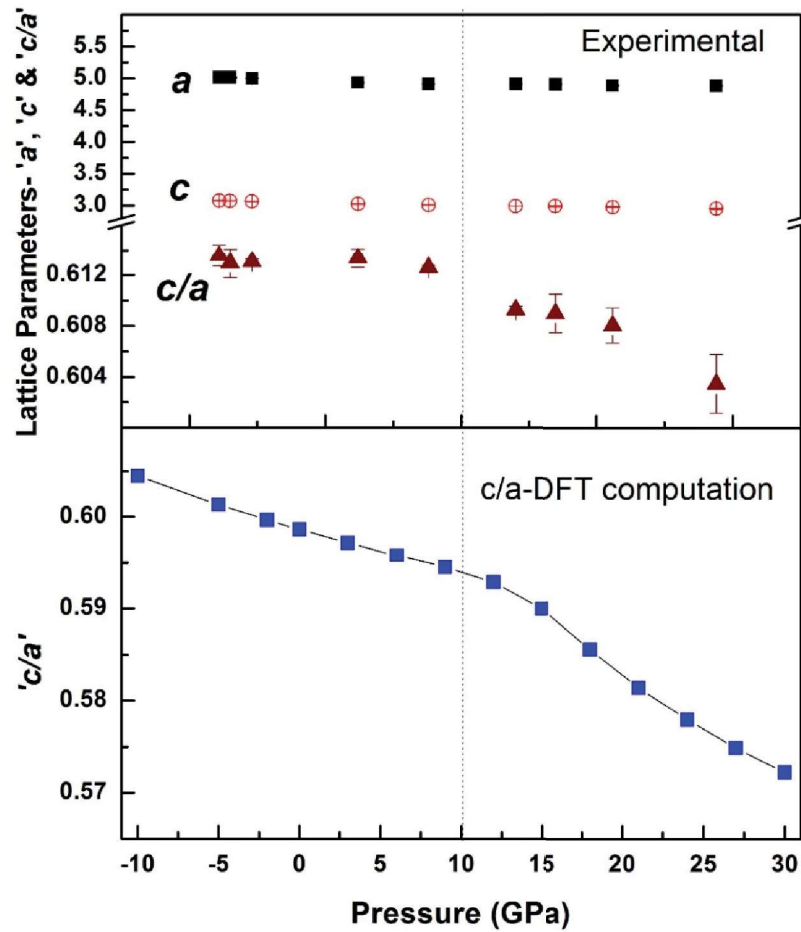
Figure 4.14: *Lattice parameters & 'c/a' ratio vs Pressure at ambient temperature: Top-Experimental, Bottom: Computation; Computation has been extended to the negative pressures to get an extrapolated view of the rate of change in c/a ratio*

The volume of the unit cell at different pressures are plotted as shown in figure 4.15. Pressure-Volume data have been fitted with Birch-Murnaghan EOS resulting in the bulk

127

With 50% randomness at U and Zr positions in UZr_2, it is found that there is a huge mismatch in the intensities of observed and calculated patterns [figure 4.12 (b), bottom]. However, the refinement of the occupancy factor at (1/3, 2/3, 1/2) and (2/3, 1/3, 1/2) positions results in a better match in the intensities. The occupancy factor of 0.84 at Zr position (1/3, 2/3, 1/2) turns out to be good fitting [figure 4.12 (b), top] i.e. in 84% of the unit cells Zr occupies (1/3, 2/3, 1/2) position in δ-UZr_2.

4.4.3.2 High-Pressure study at ambient temperature

High-pressure experiment on UZr_2 has been carried out up to 20 GPa at synchrotron source. Figure 4.13 shows XRD patterns at various pressures.

Figure 4.13: HP-XRD pattern of UZr_2

4.4.3 UZr$_2$

4.4.3.1 Structural analysis of δ-UZr$_2$ at ambient

X-ray diffraction study on UZr$_2$ was carried out at ambient temperature and pressure. The obtained data was analyzed using GSAS Rietveld refinement software [21]. It is reported that in UZr$_2$, a Zr atom occupies (000) position, and two U and two Zr atoms randomly occupy (1/3, 2/3, 1/2) and (2/3, 1/3, 1/2) positions [22,23]. A unit cell describing the atom positions are shown in figure [4.12 (a)].
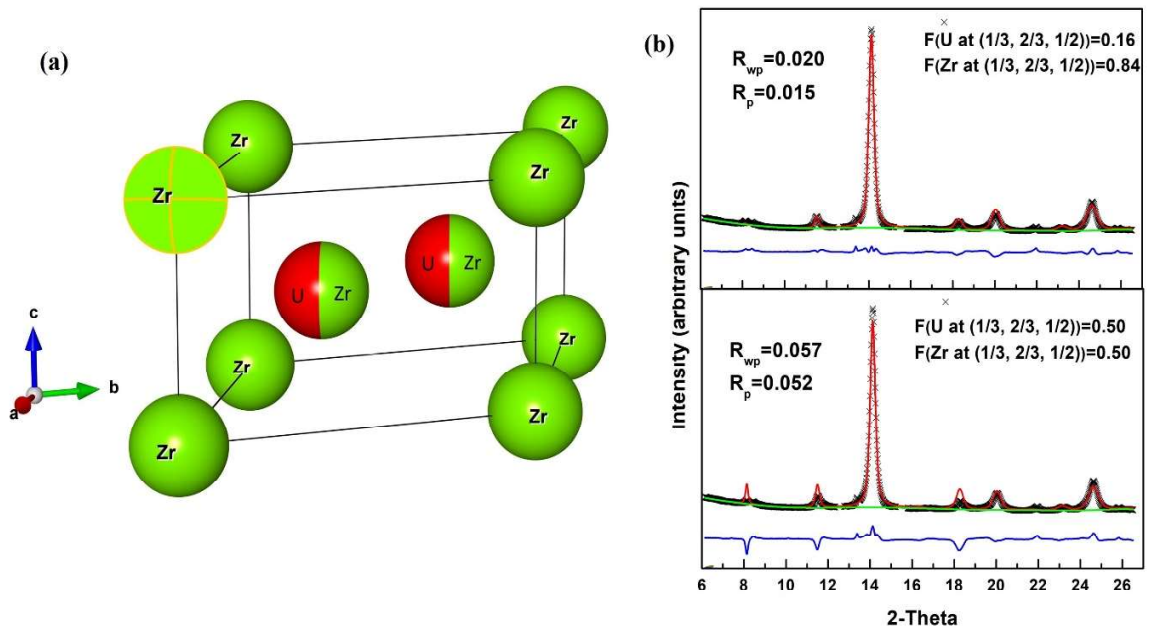
Figure 4.12: **(a)** A unit cell of UZr$_2$ **(b)** Rietveld Refined X-ray diffraction pattern. Bottom plot shows the mismatch in the observed and calculated intensity when fitted with 50% randomness at occupancy at (1/3, 2/3, 1/2) & (2/3, 1/3, 1/2) sites. Top plot shows better fitting with occupancy factor of 0.84 for Zr at (1/3, 2/3, 1/2)
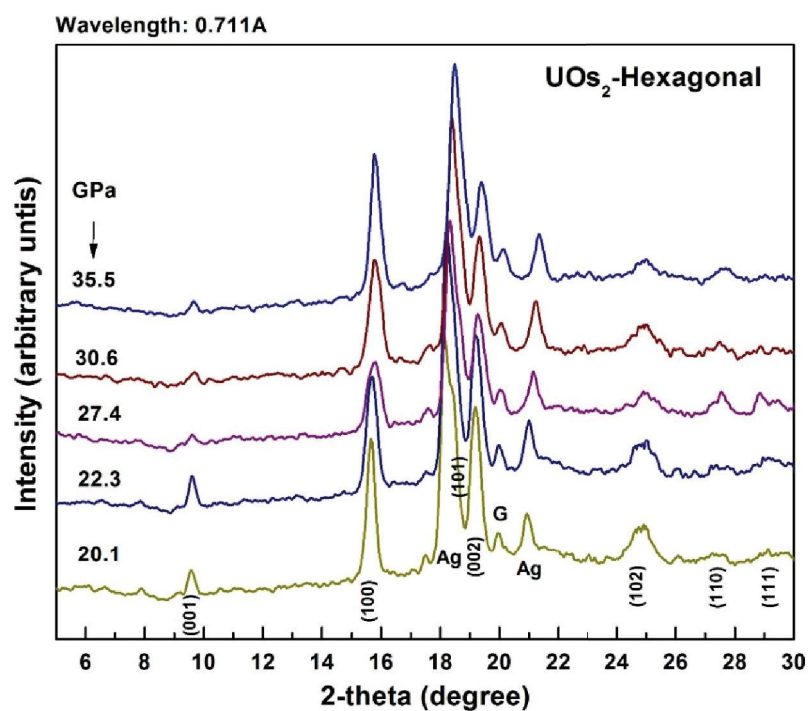
Figure 4.10: *Indexed high-pressure phase of UOs₂*
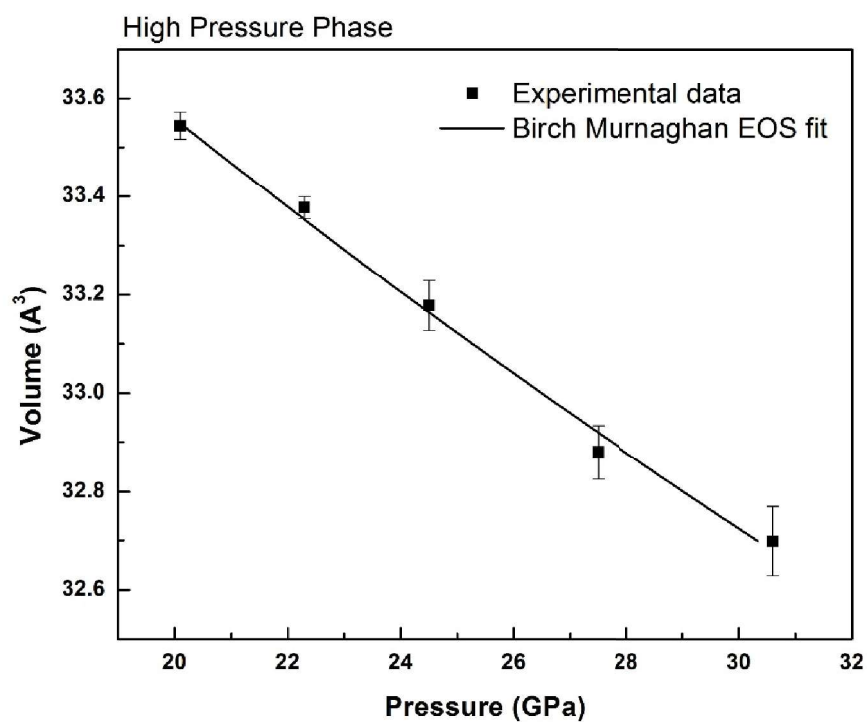
Figure 4.11: *P-V curve of high-pressure phase*

124

only 1 formula unit. Therefore, the possible structures with 1 formula unit i.e. *hP3* have been searched in the high-pressure structural sequence. XRD patterns for different space groups are generated with lattice parameter a=3.013 Å and c=4.267 Å. However, the following space groups-164,168,174,175,177,183,187,189,191 are found be matching with the Bragg reflections of 20.1 GPa experimental pattern.

As described in chapter 1, most of the UX_2 type compounds are observed to follow structural sequence under pressure. $CeCd_2$, AlB_2 are rhombohedral/hexagonal structure types which exist in the sequence containing one formula unit in each unit cell. However, none of the structure types have c/a ratio of 1.41, which is seen here. Therefore, it can be concluded that UOs_2 doesn't follow the high-pressure structural sequence. The XRD patterns for other structure types containing one formula unit with similar c/a ratio viz. HNi_2, CdI_2, $BaLiSi$ were generated but none of the structures match the experimental Bragg reflections. A more elaborate study is required to find out the coordinates of the atoms of the high-pressure phase.

The high-pressure indexed pattern was fitted to the hexagonal structure, and the lattice parameters were estimated using NIST*AIDS-83 software at various pressures. The volume of a unit cell of the high-pressure phase is plotted against increasing pressure in figure 4.11. The lattice parameters are found to decrease with pressure. Birch Murnaghan equation of state fit to P-V curve gives the bulk modulus of the daughter phase to be 365.7 GPa. This is the highest bulk modulus obtained till now among any uranium intermetallics. The obtained daughter hexagonal phase is irreversible hence the sample can be retrieved. Higher bulk modulus of the daughter phase was expected as the atomic density in the unit cell is more as compared to the parent phase.

The estimated lattice parameter form the XRD patterns are found to decrease with increasing pressure. The P-V curve of UOs_2 was fitted to Birch Murnaghan EOS up to 12.0 GPa [figure 4.9], resulting in the bulk modulus of the material to be 261.0 GPa.

After 12 GPa, the P-V curve shows a discontinuity, when fitted to the $MgCu_2$ structure [figure 4.9], in the pressure range of 12.0 GPa to 20.1 GPa wherein the volume of the cell does not change much over the said pressure range. To clarify the abnormality, a very careful observation of diffraction data of 16 GPa has been carried out. The XRD data reveals that the Bragg peaks *(311)* and *(222)* don't follow the increase in pressure, and the peaks are found to move towards lower theta. However, peak *(111)* & *(220)* is found to move towards higher theta. Bragg peak *(331)* is found to move towards higher theta by a large extent when pressure is increased from 16 GPa to 20.1 GPa. Therefore, it can be concluded from the observation of all peak movements along with the anomaly in the P-V curve that there is a new high-pressure phase appearing at 12 GPa and the phase transformation completes at 20.1 GPa. Such type of transformations are known to exist for $REOs_2$ (RE=Rare Earth) compounds [19] and are attributed to different stacking sequences of atomic layers [20]. Therefore, 20.1 GPa HP-XRD pattern has been considered for high-pressure phase analysis. Above 20.1 GPa the HP-XRD patterns are shown in figure 4.10. To obtain the structure of the new high-pressure phase, possible lattices were generated in different volume intervals using POWD- an indexing software. Out of all the crystal systems, hexagonal lattice with lattice parameter a =3.013 Å and c=4.267 Å gives the best figure of merit F(34). The volume of the new hexagonal lattice comes out to be 33.55 Å^3, however, the parent phase cell volume was 424 Å^3 which had 8 formula units in each unit cell. The high-pressure phase having volume 33.55 Å^3, can have
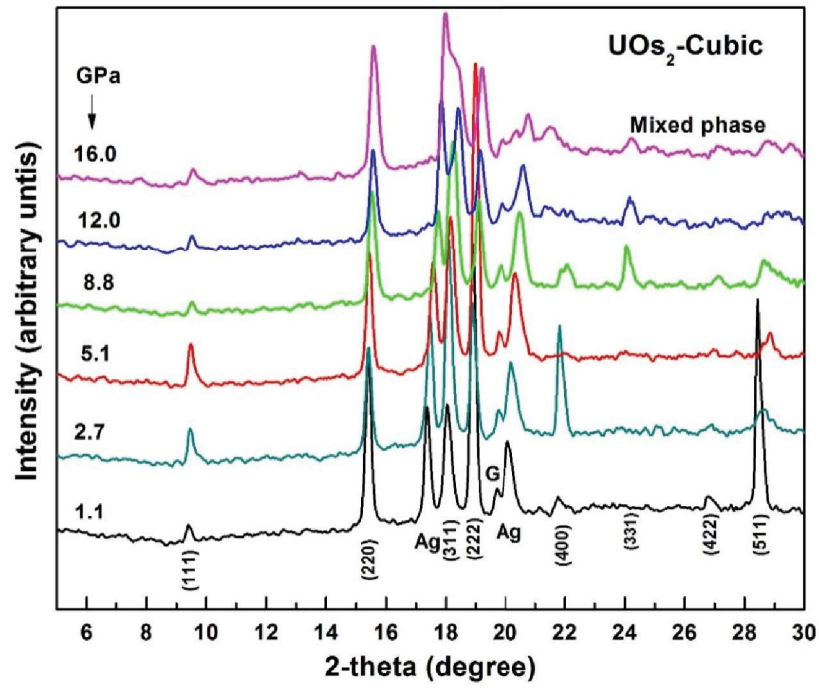
Figure 4.8: *HP-XRD pattern of UOs₂ at selected pressures*
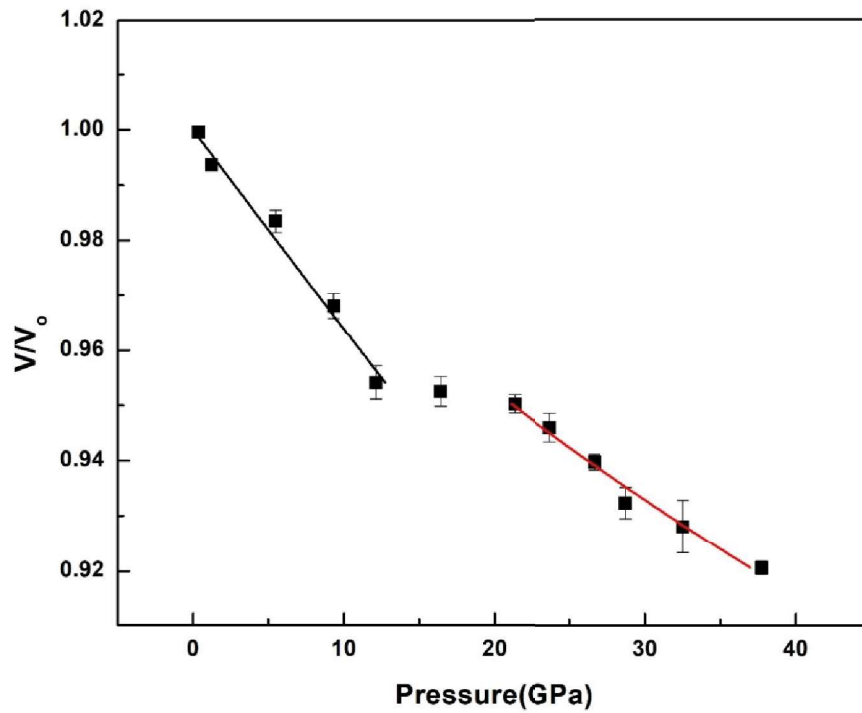
Figure 4.9: *P-V plot for parent –MgCu₂ type- phase of UOs₂ . B-M EOS fit for the parent phase shows two EOS fit, clearly showing a phase transition.*

The total energy of UIr$_2$ has been calculated at different primitive cell volume. The obtained data were fitted to the 3rd order Birch-Murnaghan equation of state. The fitting gives the bulk modulus of the material as 244.3 GPa and its pressure derivative as 4.75 [figure 4.7]. The bulk modulus value differs by 14% from that of the experimental bulk modulus which is an acceptable difference.
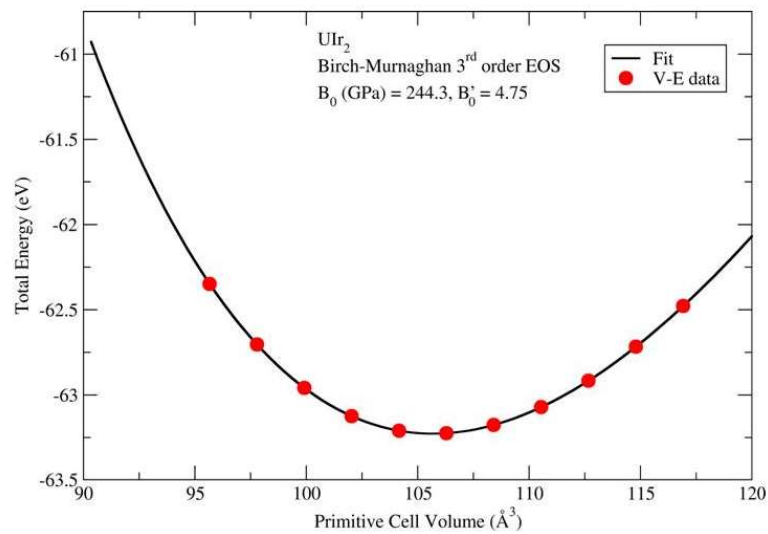
Figure 4.7: Computed total energy vs Primitive Cell Volume plot, data fitted to the 3rd order Birch Murnaghan equation of state

4.4.2 UOs$_2$

The high-pressure XRD study of UOs$_2$-Cubic phase was performed up to 36.0 GPa. Figure 4.8 shows X-ray diffraction pattern of UOs$_2$ at selected pressures. The diffraction patterns of UOs$_2$ were indexed with Fd-3m space group symmetry. However, the high-pressure diffraction patterns of UOs$_2$ are indexable only up to 12 GPa with Fd-3m space group, beyond 12 GPa the Bragg reflections are not indexable indicating the existence of a different phase.
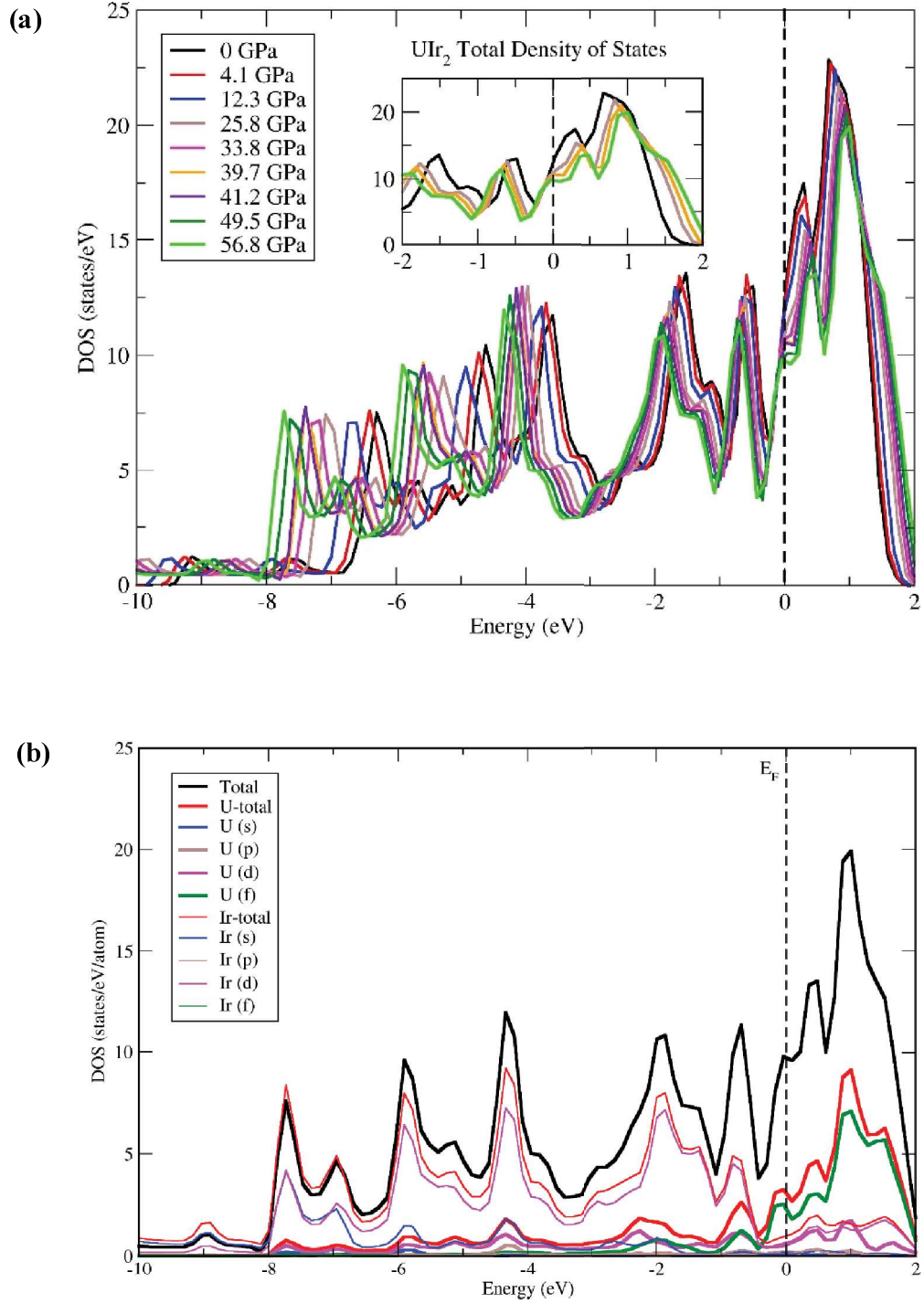
Figure 4.6: *(a) Total Density of state vs energy plot at various pressures. Inset shows the expanded view of total density of state near the Fermi energy. (b) Contributions of individual atoms to the total density of state at 56.8 GPa*

(b)
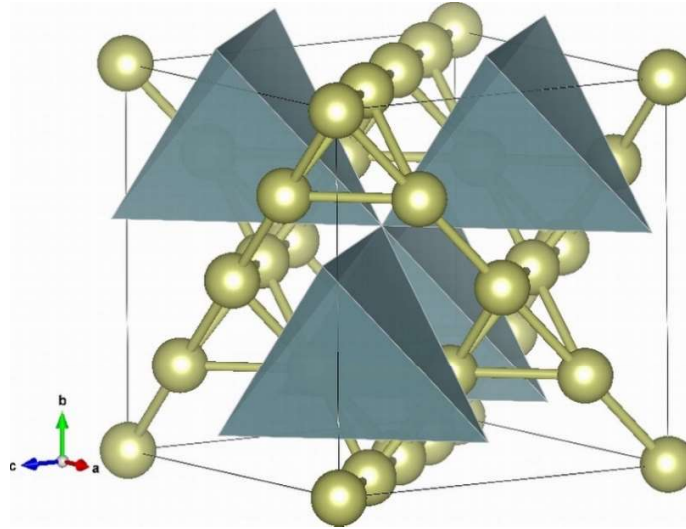
Figure 4.5: (b) *Structure of UIr₂: Uranium tetrahedra representation, interpenetrating in the Iridium network*

The density of state (DOS) vs energy plots were generated at various pressures up to 56.8 GPa and are shown in Figure 4.6 (a). It is evident from the plots that DOS changes significantly at Fermi energy as a function of pressure. Fermi energy also shifts to higher energy due to the localization of uranium's 5-f electrons in U-Ir bonding. The inset of the DOS plot [figure 4.6 (a)] shows a clear dip in the density of state at Fermi energy. With pressure, it is seen that a dip originates at E_F which in turn creates a shallow minimum in the conduction band near E_F. As electrons at Fermi energy are responsible for the bonding and overall behavior of the material, a lower density of state near E_F might point out to the emergence of a new stable phase [18]. The phase transition where the dip in DOS originates, is seen to start at the same pressure range observed in our experiments. Figure 4.6 (b) shows the individual atom contribution to the total DOS. It can be clearly seen that U-f electrons majorly contribute to the total DOS at Fermi Energy. Therefore, f-electrons of uranium are responsible for the phase transition to take place at high pressures.

interpenetrating network of uranium tetrahedra with a uranium atom at the center and corners of the tetrahedra, and iridium tetrahedra with the iridium atoms occupy only the vertices of the tetrahedral (figure 4.5 a, 4.5 b). Ir-Ir tetrahedron has short bonds compared to the U-U tetrahedron, hence the iridium tetrahedra form a stronger network as compared to the uranium tetrahedra network. Also, U-Ir bonding is metallic with covalent character in nature. The covalency of U-Ir bonding increases with pressure (figure 4.4 a) causing the bond to be more rigid. Hence, pressure directly affects uranium tetrahedra and bonds. Thus, the new structure can be envisaged in the form of change in the uranium network.

(a)
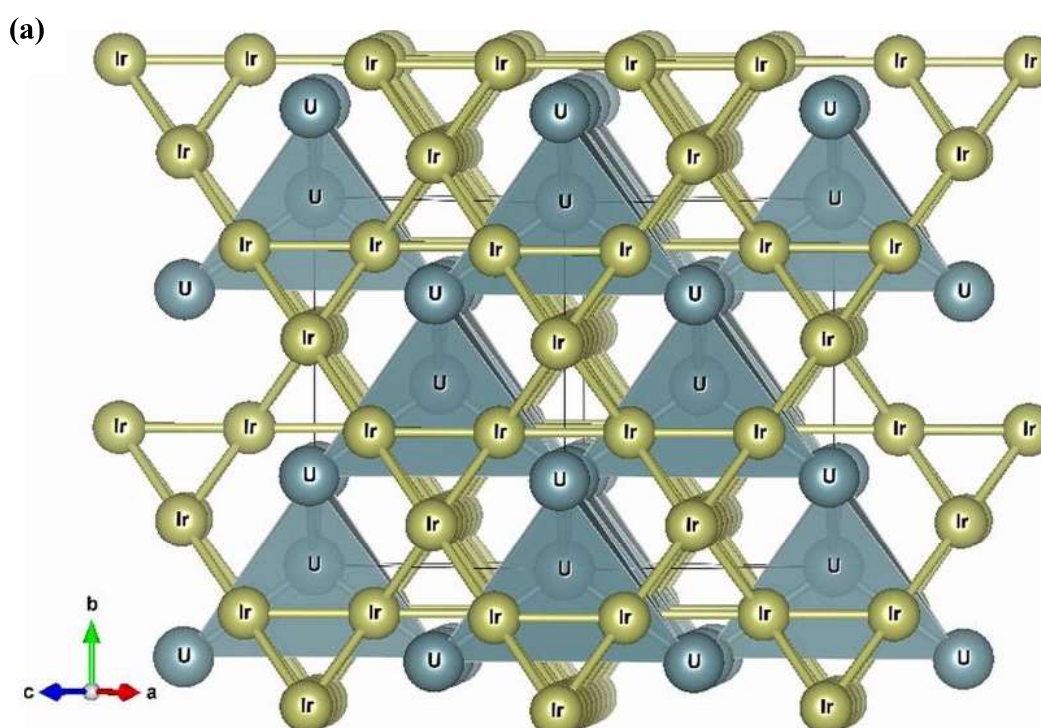
Figure 4.5: (a). Structure of UIr$_2$: tetrahedra representation

(a)

(b)
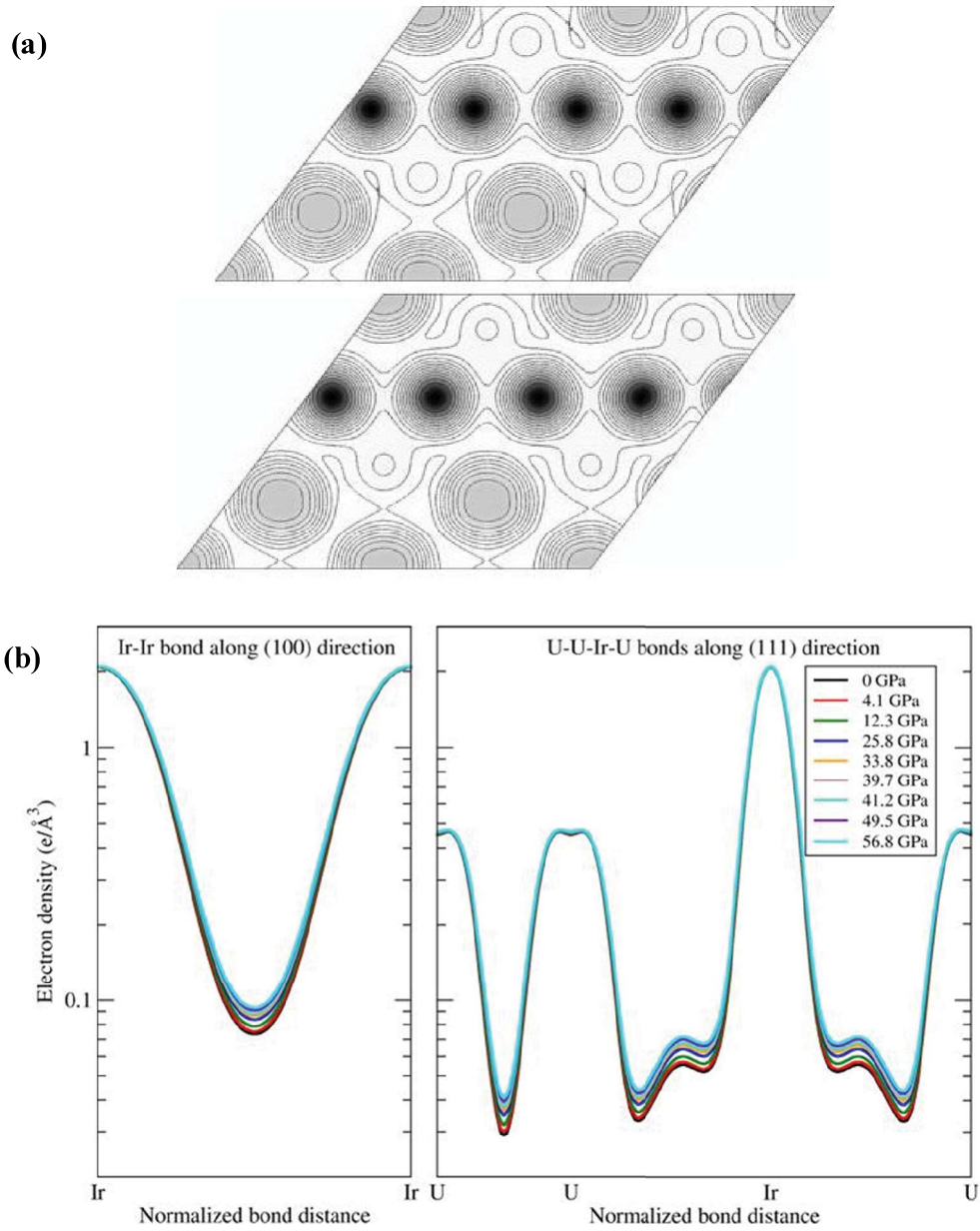
Figure 4.4: (a). Charge density plot in the (111) plane at various pressures (top=

ambient), bottom= 56.8 GPa (b). Electron density vs normalized bond distance

To explain the origin of phase transition in UIr_2 at high-pressures, the structure and bonding have been probed. UIr_2 structure, at ambient, can be visualized in the form of an

116

and these three new peaks are considered. Among various crystal structures hexagonal structure with lattice parameters $a= 7.662$ Å and $c=6.373$ Å is found to be the best lattice with a large figure of merit indicating that mixed phase is composed of $MgCu_2$ type structure and a hexagonal lattice. X-ray diffraction pattern was generated for the predicted hexagonal structure types of f-IMC's with lattice parameters $a = 7.663$ Å and $c = 6.373$ Å. The patterns generated for $CeCd_2$ (hex)- $CaIn_2$ (hex) -AlB_2 (hex) do not correspond to the experimentally observed pattern. $MgNi_2$ and $MgZn_2$ are a set of related hexagonal structures and occur frequently in UX_2 type compounds as seen in the case of UAl_2 [17]. With the obtained hexagonal lattice, patterns were generated for $MgNi_2$ and $MgZn_2$, and it was observed that these do not correspond to our experimental observation, either.

Therefore, it can be concluded that at high-pressure UIr_2 undergoes a structural transition to a crystal structure with tetragonal lattice, which yields the best figure of merit. To understand the structural stability of UIr_2, first principle electronic structure calculations have been carried out. Charge density plot (figure 4.4 a) along (*111*) direction shows that the U-Ir bonding has both metallic as well as covalent character, whereas, U-U and Ir-Ir bondings are purely metallic. Also, the covalent nature of bonding in U-Ir increases with pressure and the increase in terms of charge density is from 0.054 e/Å^3 to 0.072 e/Å^3 in the pressure range of 0 GPa to 56.8 GPa as measured along the (*111*) direction which causes localization of the 5-f electrons in uranium where uranium is bonded with iridium [figure 4.4 b]. Whereas, U-U (*111* direction) and Ir-Ir (*100* direction) metallic nature of bonding increases from 0.028 e/Å^3 to 0.041 e/Å^3 and 0.07 e/Å^3 to 0.09 e/Å^3, respectively, for the pressure range from 0 GPa to 56.8 GPa.

25 – 40 GPa are quite broad, and all the peaks become well resolved at 40 GPa. This feature is reproducible and has been confirmed not to be an artifact of any data processing. Solving the crystal structure of high-pressure phase is a non-trivial task because of preferred orientation effects and the limited range of 2-theta. Empirically the following structure types are found to be stable with increasing pressure for f-electron based intermetallic compounds (f-IMC's): $MgCu_2$ (cubic) -$MoSi_2$ (Tetragonal) -$CeCd_2$ (hex) - $CeCu_2$ (orthorhombic) -$CaIn_2$ (hex) -AlB_2 (hex)- $ZrSi_2$ (orthorhombic) -$ThSi_2$ (tetragonal) - $SmSb_2$ (orthorhombic) -Cu_2Sb (tetragonal). For high pressure phase structural analysis, the HP-XRD pattern at 40 GPa has been considered. All the seven observed reflections were indexed using POWD [16] and NIST*AIDS-83 powder diffraction indexing programs. Tetragonal lattice with a = 6.460 Å and c = 10.313 Å gives the best figure of merit (F_7= 20.9) indicating the high-pressure structure to be a tetragonal lattice. In the above mentioned structural sequence established for f-IMC's, the following structure types $MoSi_2$, $ThSi_2$, and Cu_2Sb have tetragonal lattice. For these structure types, XRD patterns were generated with the obtained tetragonal lattice parameter. However, the generated reflections do not match with the experimentally obtained X-ray diffraction pattern.

Also, the possibility of mixed phase can't be ruled out for high-pressure structural analysis. As there are many unchanged peaks at transition pressure and the fact that $MgCu_2$ type structure is found to be very stable for UX_2 type of systems, the possibility of co-existence of parent and the high-pressure phase is considered. However, with the available high-pressure data where preferred orientation persists, it is difficult to make a conclusive comment on intensities, which can be guiding route to find out the mixed phase. In the search for mixed phase, the splitting of peaks (*222*), (*422*) and (*511*) are taken into account

114

In uranium-based intermetallic compounds itinerant 5-f electrons participate in bonding and leads to high bulk modulus [14]. UIr_2 also follows a similar trend which clearly demonstrates the itinerancy of 5-f electrons. This argument is well supported by the Hill limit criterion, which states that U-U distance dictates the itinerancy and localization of 5-f electrons. In this case, U-U distance is 3.251 Å which is below the Hill limit (~3.5 Å), indicating delocalization of 5-f electrons in UIr_2 system up to 40 GPa. Earlier high-pressure experiment on the same sample was reported up to 50 GPa and the structure was found to be stable [15]. However, our HP-XRD experiment indicates a phase transition to a new structure above ~25 GPa associated with splitting of (222), (422) and (511) peaks as shown in figure 4.3 (a), (c), (d).
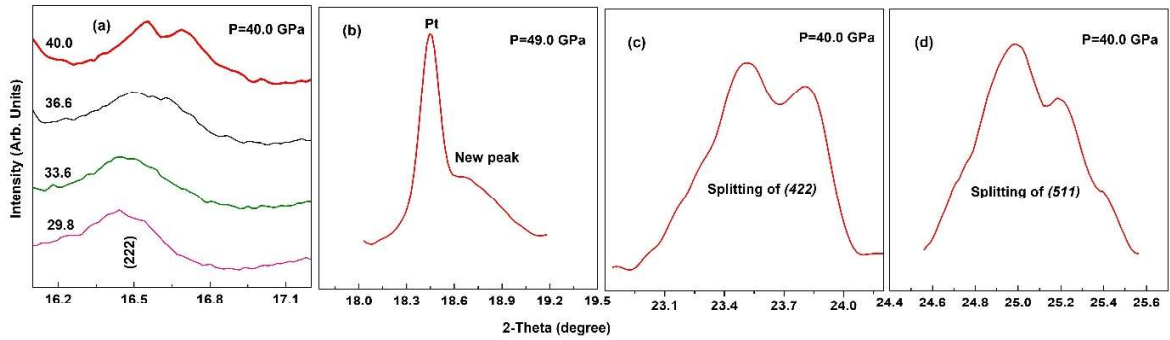
Figure 4.3: *X-ray diffraction patterns showing clear splitting of several peaks (a)- (222), (c)- (422) and (d)- (511) at 40 GPa. Diffraction plot (b) shows the emergence of the new peak at higher pressure 49.0 GPa. These are an indicative of the phase transformation at higher pressures.*

Few new peaks, e.g. at theta- 9.28 degree also appear at higher pressures [figure 4.3 (b)], clearly indicating structural phase transition. The sample peaks in the pressure range of ~

Table 4.2. Tabulation of volume and lattice parameter variation with pressure

Lattice Parameter, *a* (Å)	Volume (Å^3)	Pressure (GPa)
7.559	431.9	0.4
7.530	426.9	3.6
7.506	423.0	7.0
7.464	415.8	11.8
7.441	411.9	16.6
7.418	408.2	19.6
7.390	403.6	25.2
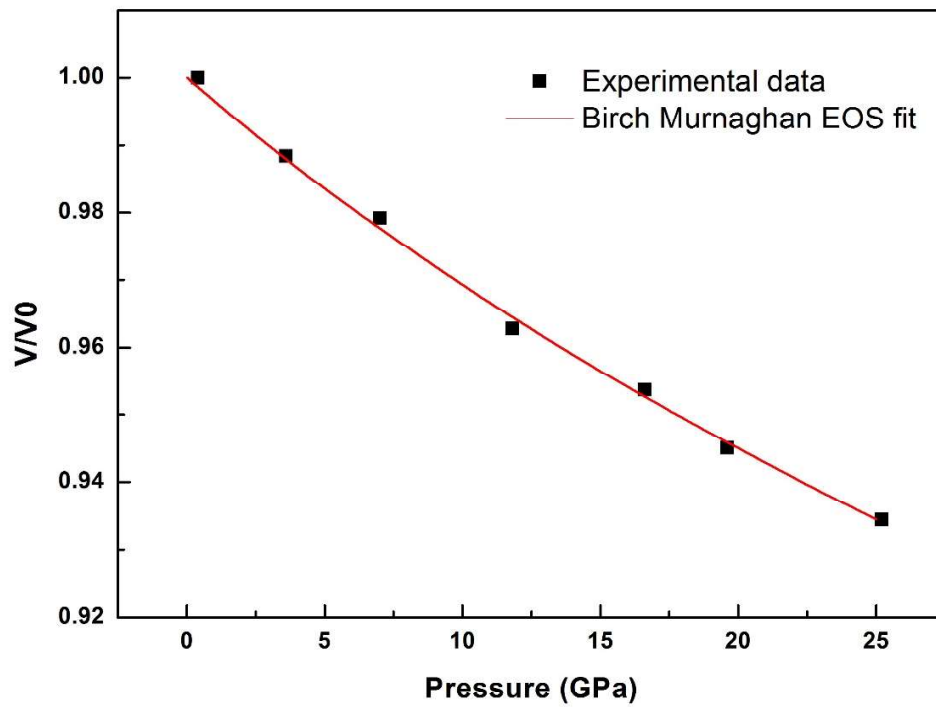
Figure 4.2: Pressure versus volume curve of UIr$_2$ up to 25 GPa.

4.4. Results and Discussion

4.4.1 UIr$_2$

High-pressure experiment on UIr$_2$ up to 55 GPa, brings out a phase transformation which is not seen in the similar type of UX$_2$ type compounds. The diffraction patterns at various pressures are shown in figure 4.1. The observed *hkl* reflections of the parent phase in the high-pressure experiment are: (*111*), (*220*), (*222*), (*422*), (*511*), and (*440*). These reflections could be followed up to ~25.2 GPa. Lattice parameters and volumes of the unit cell were estimated up to 25.2 GPa. The values are listed in table 4.2. Pressure-volume data were fitted with Birch-Murnaghan EOS [13], and estimated bulk modulus & its pressure derivative are found to be 284 GPa and 7.9 (Figure 4.2) respectively.
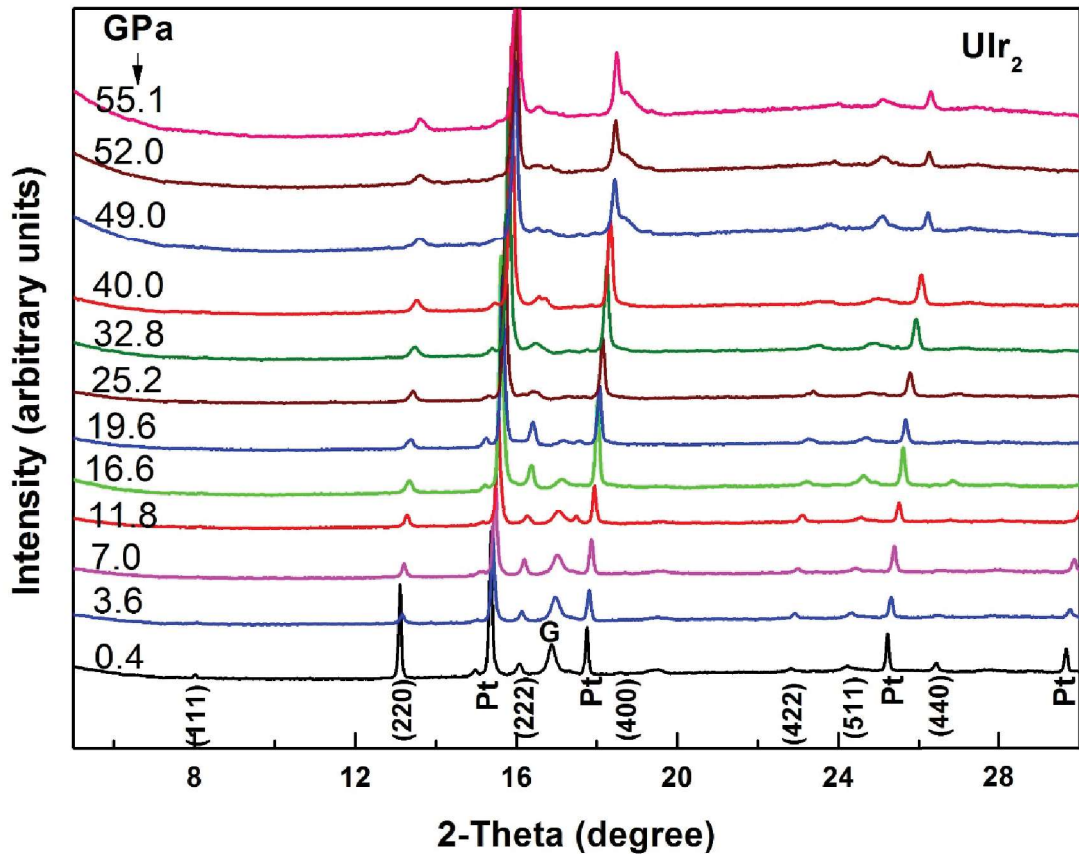
Figure 4.1: *HP-XRD patterns of UIr$_2$ up to 55 GPa, G represents gasket peak.*

point mesh. The minimum energy configuration for the UIr_2 system was obtained by relaxing the volume of the unit cell as there are no free parameters in the atomic positions in the unit cell. For the equation of state (EOS) calculations, the volume of the primitive cell was changed in +10% to -10% range in 11 steps and total energies of all the configurations were calculated. The total energy versus volume data was fitted to the third order Birch-Murnaghan Equation of State (EOS) to find the minimum energy volume/lattice parameter, bulk modulus B_0, its variation with pressure B_0' and the change in the internal pressure in the system as a function of volume. From this data, the volumes corresponding to the experimentally observed pressures were selected and the electronic properties such as the total and partial density of states (DOS), electronic density and the band structure were calculated for all the selected configurations. The results of these calculations are presented in this chapter and used to interpret the experimentally observed behavior of UIr_2 under pressure.

For UZr_2, the pseudopotentials used for U and Zr treat $6s^2$ $6p^6$ $7s^2$ $5f^3$ $6d^1$ and $4s^2$ $4p^6$ $5s^2$ $4d^2$, respectively, as valence electrons. All the calculations are scalar relativistic and non-spin polarized. A plane wave energy cut-off of 450 eV and Brillouin zone sampling using a 9×9×15 gamma centered mesh were used to ensure a convergence of less than 1 meV/atom in the energies. A random occupancy of the U & Zr at positions (1/3, 2/3, 1/2) & (2/3, 1/3, 1/2) was considered. Calculations were done for different volumes which were fitted to Birch-Murnagan equation of state [12] to obtain equilibrium volume, bulk modulus and pressure derivative of bulk modulus. To see the effect of pressure both cell shape and volume were relaxed at different pressures to get equilibrium structure corresponding to each pressure.

wavelength 0.711 Å. A stainless steel gasket was used to contain the sample, pressure calibrant and pressure transmitting medium. The SS gasket chamber was filled with NaCl which acts as a pressure transmitting medium as well as pressure calibrant [6]. A pelletized chip of size ~150 μm of the powder sample (UZr_2) was placed at the center of the chamber of the gasket and topped up with the NaCl so that the sample gets completely squeezed by pressure transmitting medium isotropically. The details of HP-HT experimental procedure are discussed in chapter 2.

The HP-HT study was carried out up to ~ 6 GPa and 473 K in the temperature interval of 100 K. XRD patterns were collected for 30 minutes at each pressure & temperature. A relaxation time of 30 min was given between successive temperature intervals. Data collection was done using a mar345 image plate based detector and converted to two theta vs intensity using Fit2D software. Lattice parameter was obtained using NIST*AIDS-83 at various pressure and temperature.

4.3.3. Computational details for UIr_2 & UZr_2

First-principle based calculations were carried out to understand the bonding and charge density distribution using the density functional theory as implemented in Vienna Ab-Initio Simulation Package (VASP) [7–9]. The interaction between the valence electrons and the ionic core was described by Projector Augmented Wave (PAW) based pseudopotential [10]. Generalized Gradient Approximation as parametrized by Perdew, Burke, and Ernzerhof (PBE) [11] was used for exchange-correlation functional.

To compute the energetics of UIr_2, an energy cutoff of 800 eV and a Gamma centered 13×13×13 Monkhorst-Pack k-point grid were used for all the calculations. The total energy of the system was seen to converge with respect to the energy cutoff and the k-

synchrotron (RRCAT, Indore, INDIA) for better resolution in an angle dispersive mode. Experiments were carried out at 2.5 GeV ring energy and 150 mA ring current. The image plate based detector was employed to record the diffracted beam. A wavelength of λ= 0.6061 Å was chosen to carry out diffraction experiments. Mao-Bell type DAC was used to achieve static high pressure. Stainless Steel (SS) gasket was used to contain the sample, pressure calibrant and pressure transmitting medium. MEW (methanol: ethanol: water :: 16:3:1) and platinum function as pressure transmitting medium and pressure calibrant, respectively. Platinum was selected as its XRD peaks don't overlap with the sample. The collection time for each spectrum was about 15 min at synchrotron at ambient temperature. The high-pressure experiment has been carried out at a pressure interval of ~ 5 GPa up to 55 GPa.

Similarly, HP-XRD study on δ-UZr$_2$ was carried out up to 20 GPa using BL-12, INDUS-2 synchrotron (RRCAT, Indore, INDIA). Mao-Bell type DAC was used to achieve high pressure. The sample was loaded into the DAC along with silver as a pressure calibrant and Methanol: Ethanol: Water :: 16:3:1 as a pressure transmitting medium. Silver was used since its XRD peaks doesn't overlap with the sample peaks. The incident X-ray beam size of 100 μm and wavelength of 0.6061 Å was selected for the high-pressure diffraction studies. The diffraction data were collected for 20 minutes at each pressure using mar345 IP detector.

4.3.2. High-pressure XRD experimental details at 373-673 K

HP-HT XRD studies have been carried out using a novel custom-designed combination of membrane cell DAC coupled to a high flux micro-focus X-ray machine (of M/s XENOCS, France) [5]. Molybdenum target of the X-ray generator gives a monochromatic beam of

The X-ray diffraction study of UIr_2, UOs_2 & δ-UZr_2 revealed the sample to be in single phase. The lattice parameter of the prepared sample is tabulated in table 4.1.

Table 4.1: The observed lattice parameters of various compounds

Compound	Structure	Lattice Parameters
UIr_2	Cubic, Fd-3m	$a = 7.561$ Å
UOs_2	Cubic, Fd-3m	$a = 7.515$ Å
δ-UZr_2	AlB_2 type	$a = 5.032$ Å, $c = 3.081$ Å

4.3 Experimental and Computational details

4.3.1 High-Pressure XRD experimental details

The high-pressure X-ray diffraction (HP-XRD) study on UOs_2 was carried out up to 36 GPa using laboratory-based X-ray source and Mao-Bell Diamond Anvil Cell (DAC). The wavelength used during the high-pressure diffraction was 0.711 Å. The equation of state of silver was used as a pressure marker and MEW (Methanol: Ethanol: Water :: 16: 3:1) as a pressure transmitting medium. The details of the high-pressure experiment using Mao-Bell Diamond Anvil Cell is described in Chapter 2. During the experiment, each high-pressure pattern was collected for 2 h in angle dispersive mode.

The HP-XRD experiment on UIr_2 was performed using Rigaku ULTRAX18 rotating anode X-ray source. The experiment was further repeated at BL-12, Indus-2

and study their stability under pressure and temperature, whereas, UZr_2 was chosen to probe the structural stability of ω phase at extreme conditions.

4.2. Sample Preparation and Characterization

UOs_2 & UIr_2 were prepared by using a standard arc melting technique. The buttons of both the uranium (99.99% pure) and Os/Ir (99.99%) were cleaned using emery sheet to remove any oxide layer on the surface. The buttons were etched using dilute HNO_3 and HF. Further, they were thoroughly washed using CCl_4 and acetone. A stoichiometric measure of U and Os/Ir were melted in a tri-arc furnace in an inert atmosphere and the melted button was flipped 2-3 times to obtain a homogenous compound. The ingots were then vacuum sealed in Ar atmosphere in a quartz tube. The annealing of the ingots was carried out at 1173 K for both the samples. There exists two phases of UOs_2 in the uranium-osmium phase diagram [3]. Therefore, annealing temperature for UOs_2 becomes important and was chosen such that the room temperature phase doesn't form during annealing. U-Os ingot was quenched to ambient after annealing. However, UIr_2 has only one phase in the phase diagram and annealing temperature was chosen below the melting point of the compound.

δ-UZr_2 was also prepared using the arc-melting technique. Cleaned uranium and zirconium were taken in the stoichiometric ratio and arc-melted several times to achieve a homogenous ingot. The ingot was vacuum sealed in a quartz tube. Proper care was taken to remove atmospheric gases as the preparation is chemically very sensitive to nitrogen and oxygen [4]. The ingot was annealed at 773 K for 2 weeks, and the temperature was slowly reduced to ambient.

Chapter 4

Compressibility Study of UX$_2$ (X=Ir, Os & Zr) Type Compounds

═══

4.1 Introduction

In addition to the relevance to nuclear technologies, high pressure and high temperature study of UX$_2$ type compounds are fascinating from the physics point of view. Most of the UX$_2$ compounds stabilize in MgCu$_2$ structure. Also, some of the UX$_2$ type compounds are found in AlB$_2$ type structure [1]. The MgCu$_2$ type structure is found to be very stable, however, AlB$_2$ type shows a series of structural phase transitions under High Pressure [1,2]. As a function of pressure the following structural sequence for UX$_2$ compound is established: MgCu$_2$ (cubic) -MoSi$_2$ (Tetragonal) -CeCd$_2$ (hexagonal) -CeCu$_2$(orthorhombic) -CaIn$_2$ (hexagonal) -AlB$_2$ (hexagonal)- ZrSi$_2$ (orthorhombic) -ThSi$_2$ (tetragonal) -SmSb$_2$ (orthorhombic) -Cu$_2$Sb (tetragonal) [1]. The sequence has been verified experimentally for many UX$_2$ type compounds [2]. The details of structural stability of UX$_2$ type compounds are described in Chapter 1.

UX$_2$ type compounds display a series of phase transitions, where $5f$ electrons of uranium show itinerant and localized behavior. The study of stability and the nature of $5f$ electrons of uranium in its binary UX$_2$ type compounds such as UIr$_2$, UOs$_2$ & UZr$_2$ under High Pressure (HP) & High Pressure-High Temperature (HP-HT) remains largely unexplored. Therefore, these compounds have been studied under HP and HP-HT in this thesis. While the choice of UIr$_2$ and UOs$_2$ was to investigate their compressibility behavior

Plane Wave plus Local Orbitals Program for Calculating Crystal Properties (Austria, 2001).

[11] J. P. Perdew, K. Burke, and M. Ernzerhof, Phys. Rev. Lett. **77**, 3865 (1996).

[12] M. Divis, Phys. Status Solidi **182**, K15 (1994).

[13] V. Kathirvel, S. Chandra, N. V. Chandra Shekar, P. C. Sahu, and S. M. Babu, J. Phys. Conf. Ser. **215**, 12115 (2010).

[14] F. Birch, Phys. Rev. **71**, 809 (1947).

[15] T. Oguchi and A. J. Freeman, J. Magn. Magn. Mater. **61**, 233 (1986).

[16] R. C. Albers, A. M. Boring, P. Weinberger, and N. E. Christensen, Phys. Rev. B **32**, 7571 (1985).

[17] N. V. Chandra Shekar, P. C. Sahu, N. R. Sanjay Kumar, M. Sekar, N. Subramanian, V. Kathirvel, S. Chandra, and M. Rajagopalan, Solid State Phenom. **150**, 123 (2009).

[18] J. Hafner, F. Hulliger, W. B. Jensen, J. A. Majewski, and K. Mathis, *The Structures of Binary Compounds* (1989).

References:

[1]   P. C. Sahu, N. V. Chandra Shekar, N. Subramanian, M. Yousuf, and K. Govinda Rajan, J. Alloys Compd. **223**, 49 (1995).

[2]   N. R. Sanjay Kumar, N. Subramanian, N. V. Chandra Shekar, M. Sekar, and P. C. Sahu, Phil. Mag. Lett. **84**, 791 (2004).

[3]   V. Kathirvel, S. Chandra, N. V. Chandra Shekar, P. C. Sahu, and M. Rajagopalan, Int. J. Mod. Phys. B **25**, 551 (2011).

[4]   V. Kathirvel, N. V. Chandra Shekar, L. M. Sundaram, and P. C. Sahu, ICDD, Powder Diffr. File W26208I (2008).

[5]   A. E. Dwight, J. W. Downey, and R. A. J. Conner, Acta Crystallogr. **14**, 75 (1961).

[6]   H. H. Hill, in *Plutonium 1970 Other Actinides, W.N. Miner, ed.,The Metall. Soc. AIME, New York*, edited by Miner and W. N. (ed.) (Metallurgical Society of AIME, New York, 1970), p. 2.

[7]   A. J. Arko, M. B. Brodsky, G. W. Crabtree, D. Karim, D. D. Koelling, L. R. Windmiller, and J. B. Ketterson, Phys. Rev. B **12**, 4102 (1975).

[8]   O. Eriksson, B. Johansson, M. S. S. Brooks, and H. L. Skriver, Phys. Rev. B **40**, 9508 (1989).

[9]   H. Blank and R. Lindner, *Plutonium 1975 and Other Actinides : Proceedings of the Conference in Baden Baden, September 10-13, 1975* (North-Holland Pub. Co., 1976).

[10]   P. Blaha, K. Schwarz, G. Madsen, D. Kvasnicka, and & J. Luitz, *An Augmented*

Total DOS around the E_F of Ni$_3$Sn type structure looks different from the total DOS of AuCu$_3$ type structure.

5.4 Summary and conclusion

High-Pressure experiments on UX$_3$ (X= Rh, Ir) type compounds were performed up to 25 GPa and the material is found to be stable up to the highest pressure studied. The high-pressure results are in agreement with the results of the electronic structural calculation for URh$_3$ up to 40 GPa. Beyond 40 GPa, 2-D structural stability map predicts a possible Ni$_3$Sn type structure in URh$_3$. However, total energy vs equilibrium volume for the cubic AuCu$_3$ and hexagonal Ni$_3$Sn type structures do not intersect up to 360 GPa predicting a large structural stability of ambient cubic phase in URh$_3$.

The Birch Murnaghan Equation of state fit of experimental pressure-volume data results in the bulk modulus of the compounds URh$_3$ and UIr$_3$ to be 133.0 GPa and 262.5 GPa respectively. Such a large difference in the bulk modulus of similar (isoelectronic) compounds is very surprising. However, the reason for such a drastic increase in the bulk modulus has been attributed to the increased hybridization between uranium site and Iridium site in UIr$_3$. Also, U-f states participation in the total density of state are found to be 61.3% more in UIr$_3$ at Fermi level as compared to URh$_3$. Therefore, U-f states are solely responsible for such a large change in compressibility of the compound.
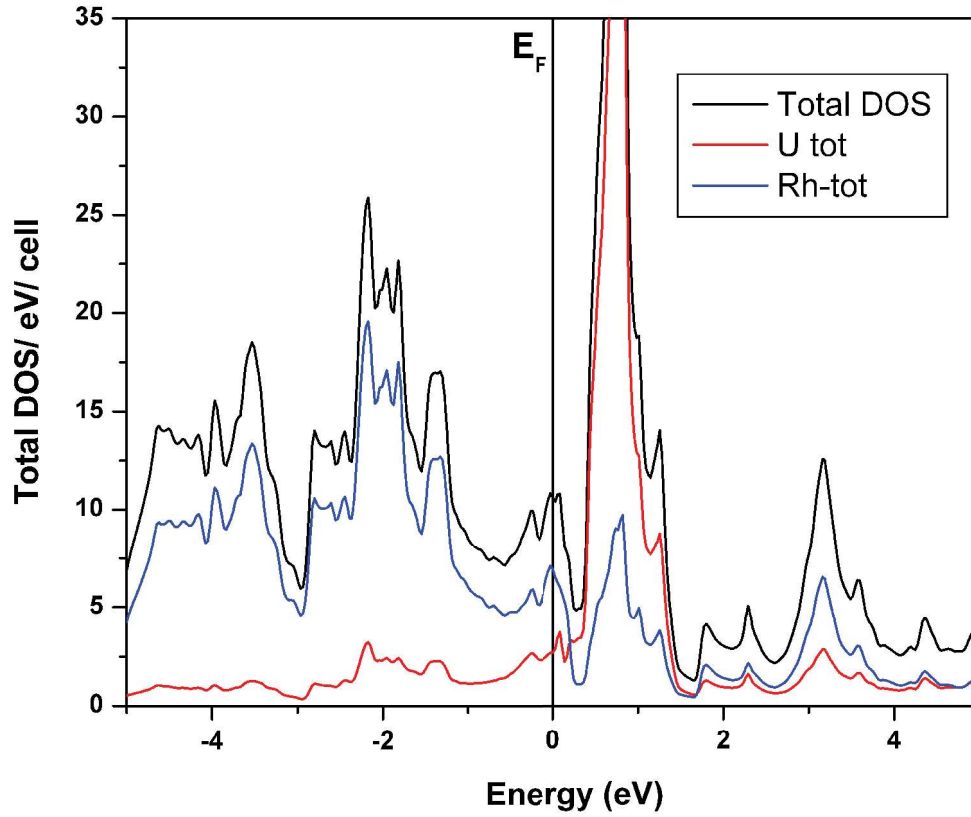
155

Figure 5.6 (b) *URh₃ in Ni₃Sn type Structure*

In figure 5.6 (a), the E_F lies very close to a maximum in the DOS curve, and the sharp narrow peak due to the U-f band is located above the Fermi level at around 0.2–1.5 eV. The tail of the f-band extends toward lower energy below the Fermi level, indicating the itinerant nature of f-electrons in URh₃ in AuCu₃ type structure. Figure 5.6 (a) shows that the Rh-d band states mostly dominated at lower energy region. Figure 5.6 (b) for Ni₃Sn type structure exhibits a similar kind of behavior as far as the itinerancy of the f-electrons is concerned. Above E_F, there is a sharp narrow peak due to the U-f band and the tail of the f-band extends below E_F which shows the strong hybridization of U-f band with Rh-d band states. However, the position of the Fermi level on the DOS curve is slightly different.

154

This figure illustrates that there is no possibility of phase transition, as the two curves do not intersect and both the curves exhibit similar kind of behavior. However, the two curves come closer to each other at lower values of V/V_0 (or higher pressure). In order to see the possibility of an intersection of the two curves at higher pressures, we extended the calculations up to 0.65 V/V_0 (360 GPa), but there was no intersection. The extrapolated curves from 360 GPa to 900 GPa did not intersect, either.

Figs. 5.6 (a) and (b) display the total DOS of URh_3 at ambient conditions in $AuCu_3$ and Ni_3Sn type structures, respectively.
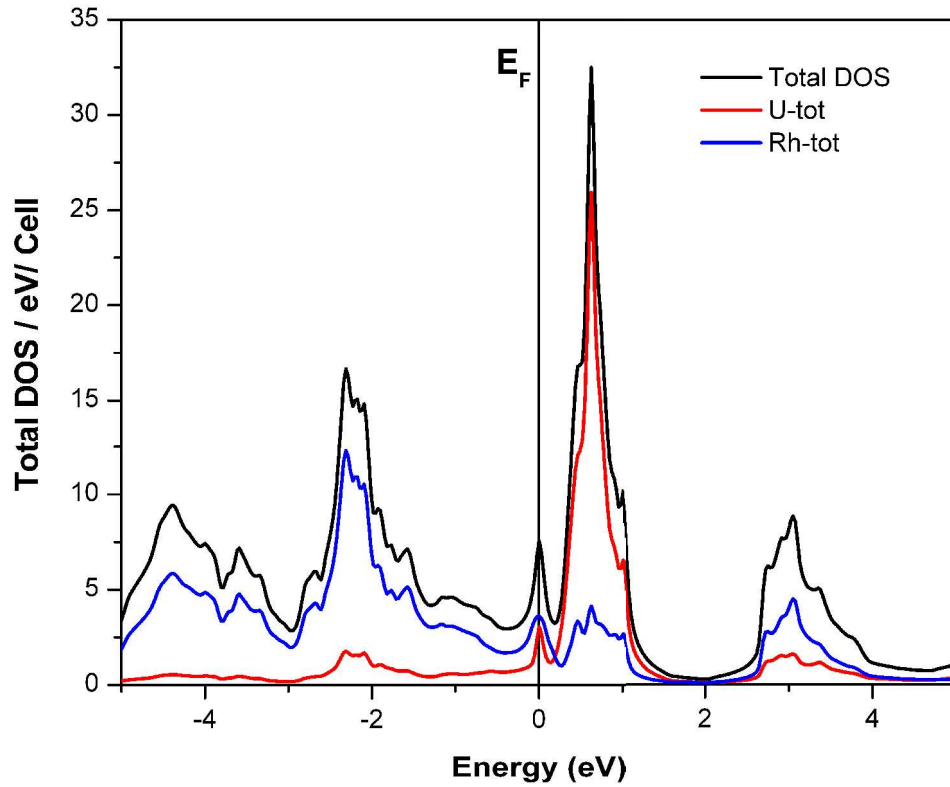

Figure 5.6 (a) URh₃ in AuCu₃ type Structure

calculated ΔX, ΔR, and VE values are -0.232, 1.2 (a.u) and 7.5, respectively. In 2-D stability maps (AB_3 type compounds), the important observation is that the domain belonging to Ni_3Sn type structure overlaps with the domain belonging to $AuCu_3$ type structure (where the URh_3 system is located). The overlap indicates that URh_3 may transform to the Ni_3Sn type structure at very high pressures due to the changes in its ΔX, ΔR and VE.

The total energy curves for the two structures are obtained by using the optimized lattice parameters. At ambient pressure, the total energy difference between the $AuCu_3$ (cubic) and Ni_3Sn (hexagonal) type structure is 0.0163 Ry/cell. This shows that total energy of Ni_3Sn (hexagonal) type structure is very close to that of the $AuCu_3$ (cubic) type structure. Figure 5.5 displays the total energy curves of both the cubic $AuCu_3$ and hexagonal Ni_3Sn type structures of URh_3.
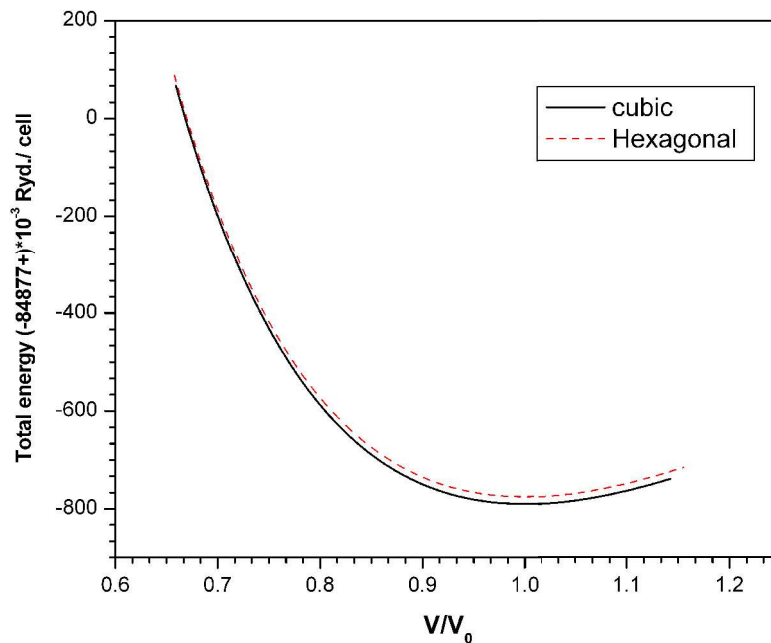

Figure 5.5: *Total energy curve for both the cubic $AuCu_3$ and hexagonal Ni_3Sn type structures up to 360 GPa.*

152

The high bulk modulus and increased stability of UIr_3 as compared to the similar compound URh_3 could be due to increased hybridization as described below:

1. High Bulk Modulus: The density of state computation on URh_3 and UIr_3 was already reported by Kathirvel *et al.*, and Oguchi *et al.*, [13,15,16]. The computation on URh_3 reveals a strong hybridization between 5-*f* orbitals of U and 4-*d* orbitals of Rh. Similar hybridization was also reported for UIr_3 where 5-*f* orbitals and 5-*d* orbitals of Iridium hybridize. However, the participation of U-*f* states at Fermi energy in total density of state for URh_3 is found to be 31% as compared to 50% for UIr_3 [15]. This large enhancement, 61.3% more, of uranium's *f*-electron contribution in the density of state for UIr_3, may lead to strengthening of bonds, and hence it could be the possible reason for high bulk modulus in UIr_3 as compared to URh_3.

2. High Stability: The position of the Fermi level E_F lies on the maxima of a peak on the DOS curve for URh_3 [13]. However, the DOS plot is different for UIr_3 wherein the Fermi level lies on a slope [15]. Above the Fermi energy, the DOS increases, however, the tail of the uranium total DOS extends to a small valley towards lower energy below the Fermi level. The tail of iridium states at lower energy too passes through the uranium's *f*-states valley leading to a strong hybridization of uranium and iridium states. Thus, UIr_3 is more stable than URh_3

5.3.2. Electronic structure and total energy calculation for URh_3

In order to look for possible high-pressure phases beyond 40 GPa, empirical method of 2-D structural stability maps for AB_3 type (where A belongs to lanthanide or actinide metals, and B belongs to *p* or *d* block metal) compounds were used [17,18]. For URh_3, the

It can be clearly seen from the figure that lattice parameter of URh_3 decreases much faster with pressure than that of UIr_3 which clearly reflects in the compressibility of the compounds. The volume of the unit cell of both the compounds is plotted in figure 5.4
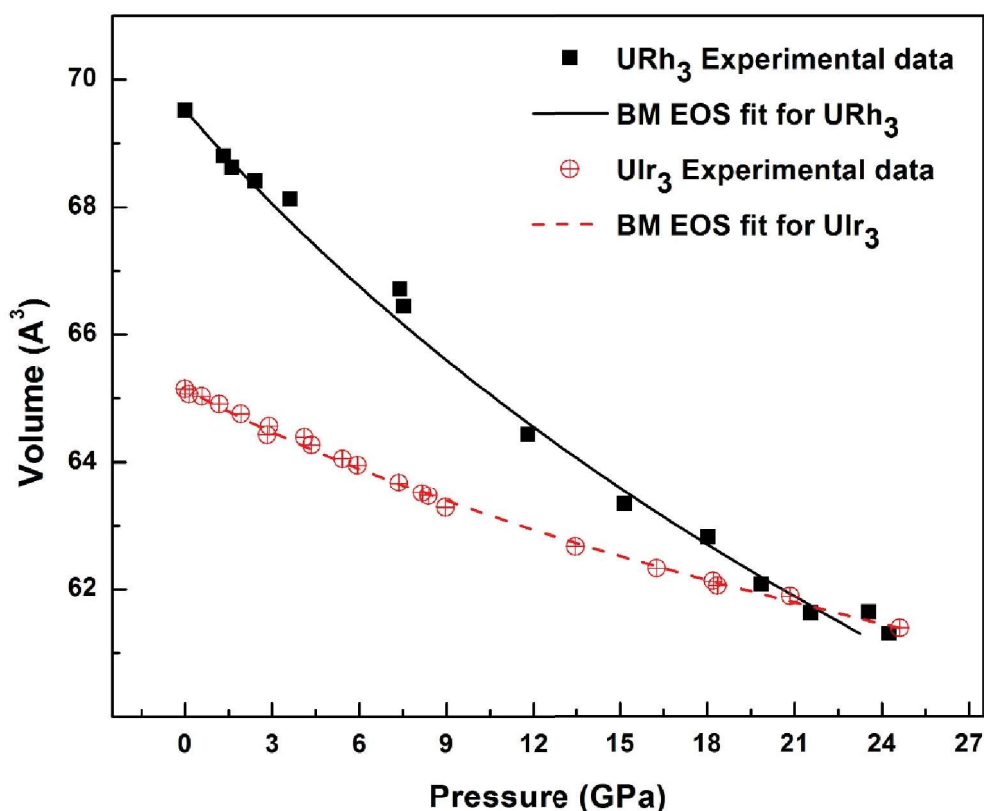
Figure 5.4: *Pressure-volume data and Birch-Murnaghan equation of state (BM EOS) fit for URh₃ and UIr₃*

The P–V data for both URh_3 and UIr_3 were fitted to Birch–Murnaghan equation of state [14] resulting in the bulk modulus of the compounds to be 133.0 GPa and 262.5 GPa, respectively. Though being the member of the same transition metal group in the periodic table and having the same structure, the uranium compounds of Rh and Ir show much different behavior as seen in terms of compressibility where URh_3 is found to be much more compressible than UIr_3.

150

It is evident from the X-ray diffraction patterns that there is no change in the structure up to 25 GPa and all the peaks are found to be indexable with the parent $AuCu_3$ type cubic structure. The stability of the URh_3 compound was probed by Kathirvel *et al.*, using density functional computation [13]. The electronic structural calculations on URh_3 up to 40 GPa show that the material remains stable up to 40 GPa as the position of the Fermi level E_F lies on a small peak in the DOS curve and it remains pinned at the same position even at 40 GPa. The small changes of the DOS at E_F support the structural stability of the URh_3 up to 40 GPa.

The lattice parameters of both the samples at different pressures were estimated using NIST*AIDS83 program and are shown in figure 5.3.
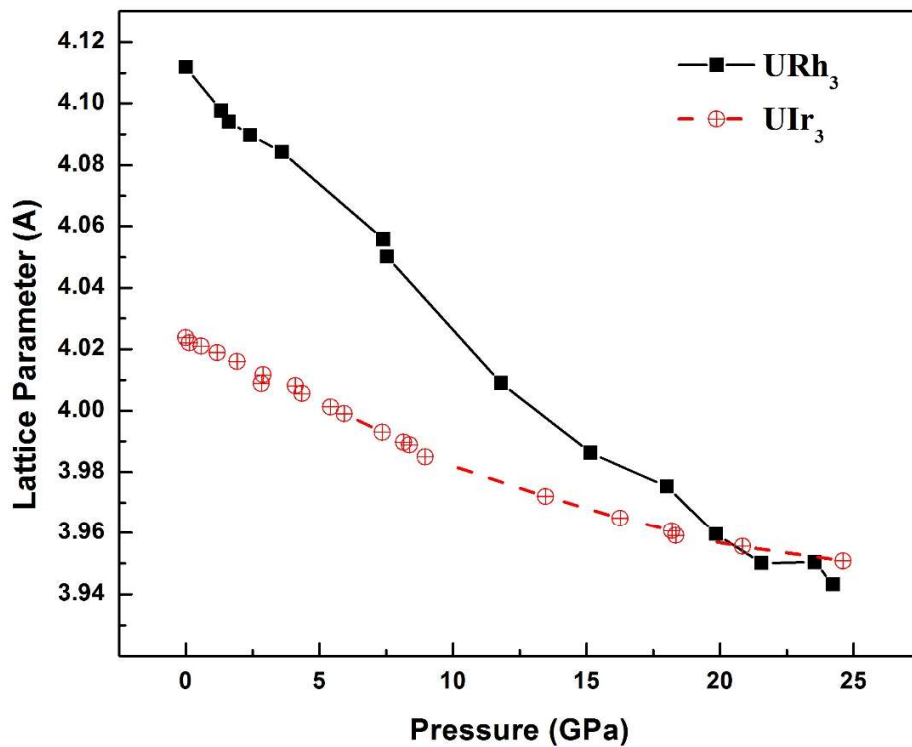

Figure 5.3: *Lattice parameter variation of URh_3 and UIr_3*

theta value in the X-ray diffraction pattern was limited to about 5°–30° because of mechanical restriction on the exit slit in the diamond-anvil cell.
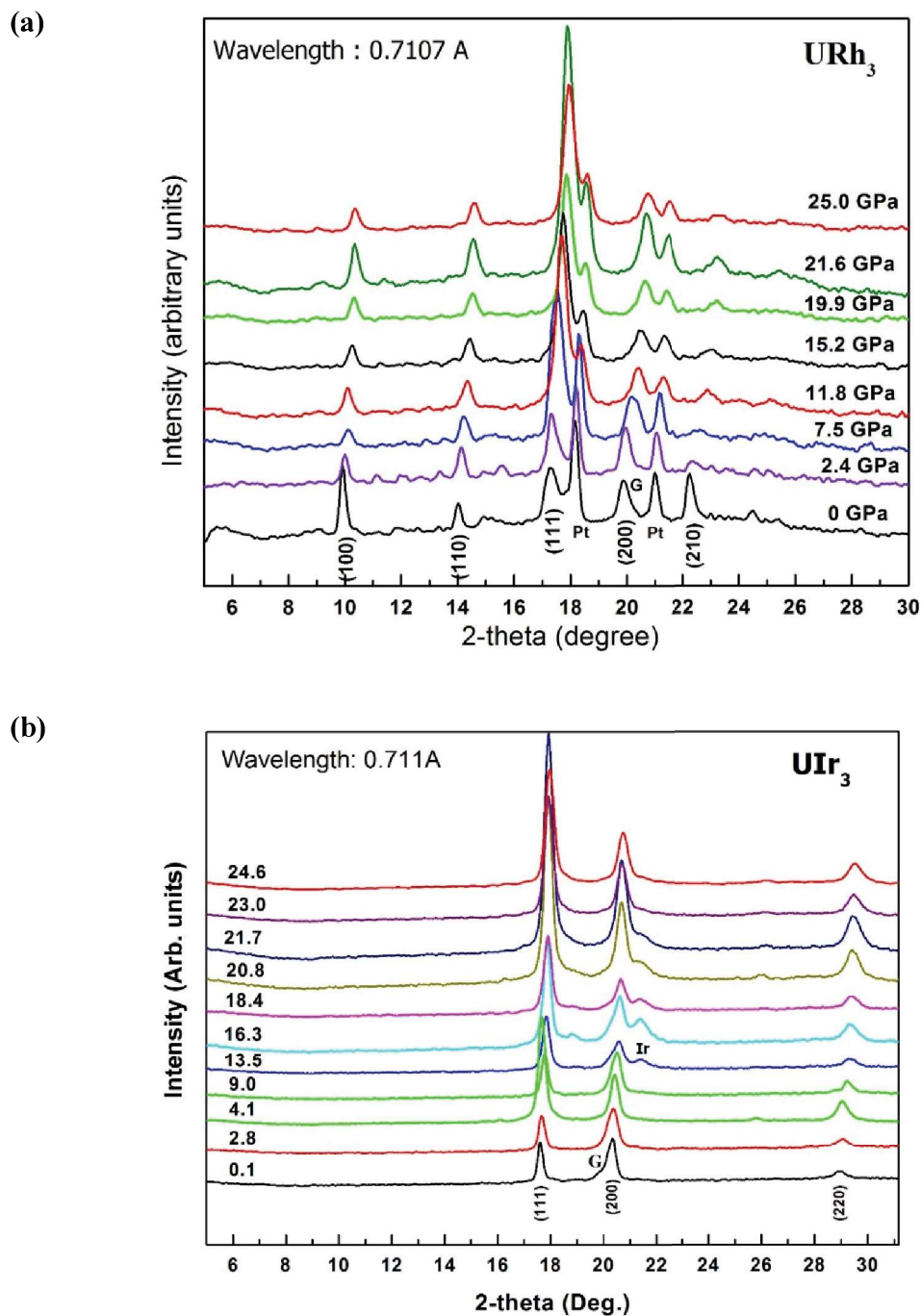
(a)

(b)

Figure 5.2: *Powder X-ray diffraction pattern of **(a)** URh₃ and **(b)** UIr₃ up to 25 GPa.*

In the above optimization procedure, the internal degrees of freedom were included and symmetry constraints were applied.

Again, these a & c values were fed into the steps 1 & 2 and repeated several times until the optimization reached up to the very low percentage of c/a ratio deviation value (*i.e.*, <0.1%; lower percentage of c/a ratio deviation value indicates the optimized c/a ratio value).

In order to optimize the volume and c/a ratio, around 20 calculations were carried out following the procedure mentioned above keeping the percentage of c/a ratio deviation value to 0.11%. The optimized lattice parameters are a=5.6806 Å and c=4.6791 Å; c/a=0.8237. The initial positions of rhodium atoms in the URh_3 (H type structure) are Rh1(0.833, 0.666, 0.25); Rh2(0.167, 0.333, 0.75); Rh3(0.167, 0.833, 0.75); Rh4(0.833, 0.167, 0.25); Rh5(0.666, 0.833, 0.75) and Rh6(0.334, 0.167, 0.25). The URh_3 compound in H type structure has free internal structure parameters for rhodium atom, and it was optimized using the calculated forces on nuclei. Here, the 2 uranium atoms occupy the positions (0.333, 0.667, 0.250) and (0.667, 0.333, 0.750). The optimized internal positions of rhodium atoms are Rh1(0.834, 0.669, 0.25); Rh2(0.165, 0.33, 0.75); Rh3(0.165, 0.834, 0.75); Rh4(0.834, 0.165, 0.25); Rh5(0.669, 0.834, 0.75); and Rh6(0.33, 0.165, 0.25).

5.3 Results and discussions

5.3.1 HPXRD Studies on URh_3 & UIr_3

Figure 5.2 (a) & 5.2 (b) show the angle-dispersive X-ray diffraction pattern of URh_3 & UIr_3, respectively, by using area sensitive detector at various selected pressures. The 2-

Hereafter, the cubic $AuCu_3$ (Space group: Pm-3m) and Ni_3Sn (Space group: P6$_3$/mmc) type structures will be mentioned as C and H type structures, respectively. Standard crystallographic data and atomic positions are available for C type structure. C type structure has only one formula unit per unit cell (i.e. 4 atoms per unit cell). But, the H type structure has two formula units per unit cell (i.e. 8 atoms per unit cell). Hence, the unit cell volume of the H type structure is two times that of the C type structure. The following procedure was adopted to estimate the approximate lattice parameters and cell volume for H type structure.

Equilibrium relaxed unit cell volume of the C type structure [13] = 64.843 Å^3

Unit cell volume of the H type structure (V_H) = 2 × Equilibrium volume of the C type structure

$$V_H = 2 \times 64.843 = 129.687 \text{ Å}^3; a = 5.714 \text{ Å}, c = 4.587 \text{ Å}; c/a \text{ ratio} = 0.802$$

Further, these approximated lattice parameters were fed into the WIEN2K code to optimize the lattice parameters. The calculation was performed in two steps. The first step was to optimize a and c values by varying volume and keeping the c/a ratio constant. The lattice parameters a and c were derived from the volume which corresponded to minimum total energy. These lattice parameters were fed as input into the second step to optimize c/a ratio. Here, the volume was kept constant and c/a ratio was changed. Different c/a ratios are obtained for a constant volume or energy. In order to find out the c/a ratio which was closer to constant energy, the percentage of deviation of c/a ratio was calculated. This deviation was added to the c/a ratio that was used in step one and the corrected c/a ratio was obtained. The lattice parameters a and c were calculated from the corrected c/a ratio.

146

URh$_3$ system in Ni$_3$Sn type structure (hexagonal structure), the approximate volume was calculated from the equilibrium volume of AuCu$_3$ type structure.
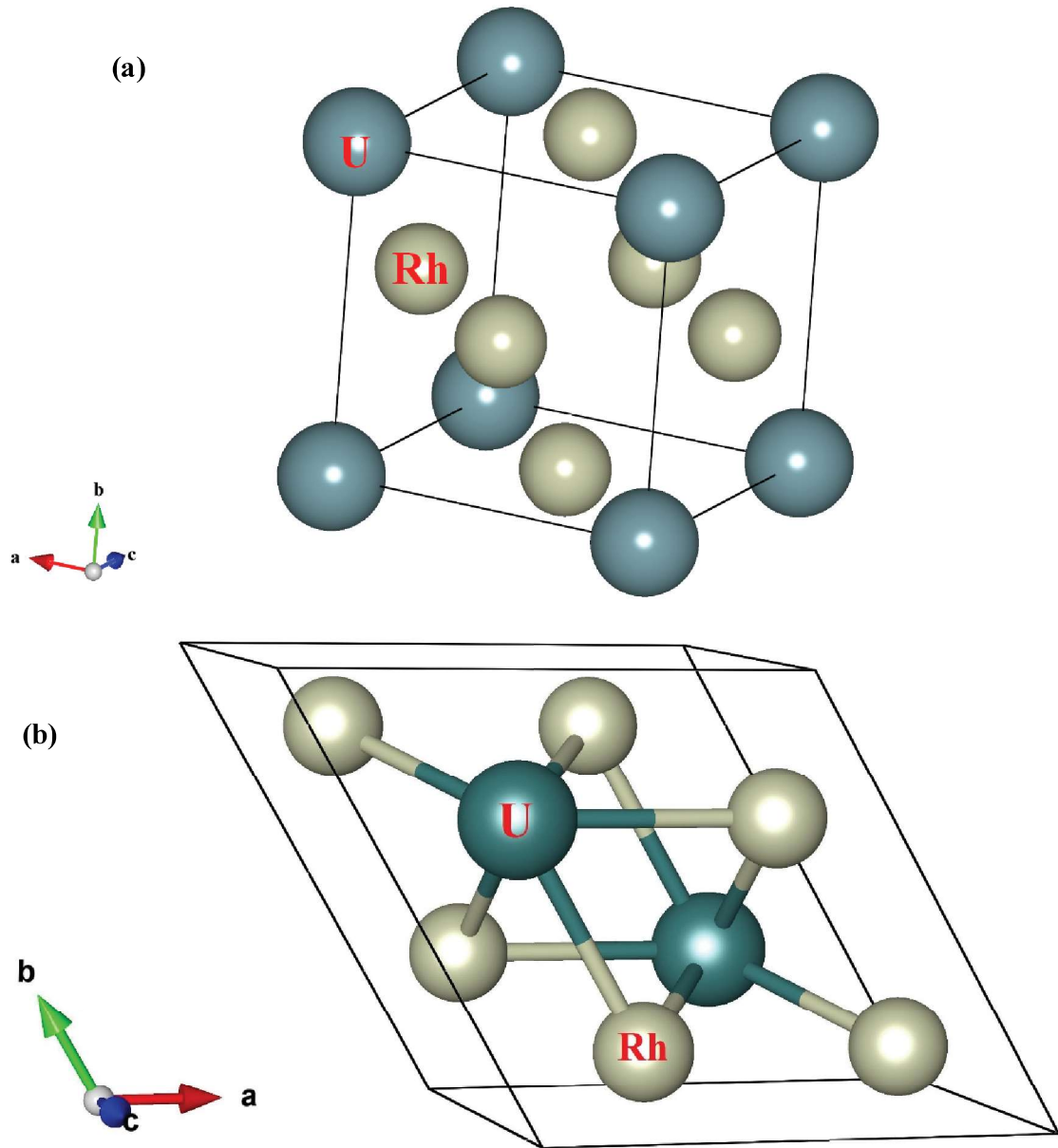
(a)

(b)

Figure 5.1: *Structures of URh$_3$:* ***(a)*** *AuCu$_3$ type cubic structure and* ***(b)*** *Ni$_3$Sn type hexagonal structure.*

145

experiment of URh$_3$, however, ruby fluorescence method was employed to estimate the pressure for UIr$_3$ experiments. A mixture of Methanol, Ethanol, and Water (MEW) in the proportion of 16:3:1 by volume was used as the pressure transmitting medium. The high-pressure experiment on URh$_3$ was carried out using Mo X-ray beam obtained from a Rigaku ULTRAX (18 kW) rotating anode X-ray generator which was monochromatized with a graphite monochromator giving Mo radiation with wavelength 0.7107 Å. The collection time for each spectrum was 2 h. However, the high-pressure experiment on UIr$_3$ was performed using a high flux micro-focus X-ray machine (of M/s XENOCS, France) with molybdenum target that gives a monochromatic beam of wavelength 0.711 Å. The collection for each spectrum was 2h. The details of the X-ray generator for both the experiments are given in chapter 2 & 3.

5.2.3 Computational details of URh$_3$

Electronic structure calculations of URh$_3$ were carried out using WIEN2k code [10] implemented with Full Potential–Linear Augmented Plane Wave (FP–LAPW) method. The exchange-correlation interaction was treated within GGA approximation of Perdew *et al.* [11]. Previous work suggests that the FP–LAPW methodology provides more reliable insights into the electronic structure of these compounds, as compared to Tight-Binding based approaches [12].

Structural Stability Map shows that URh$_3$ may stabilize in Ni$_3$Sn type structure at very high pressures. Therefore, computation has been carried out to check the stability of URh$_3$ in both the structures. Figure 5.1 (a) and (b) show the structures of URh$_3$ in AuCu$_3$ and Ni$_3$Sn type structures, respectively. In order to find out the equilibrium volume for

to compare their structural stability and understand the bonding nature of the f electron states.

5.2 Experimental and computational details

5.2.1 Sample preparation

All the UX$_3$ (X=Rh, Ir) type compounds were prepared by arc melting their stoichiometric quantities of U (99.98%), Rh (99.999%)/Ir (99.999%) in an inert atmosphere. The melted ingot was flipped several times to obtain a homogenous compound during melting. Afterwards, the ingots were vacuum sealed in an inert atmosphere in a quartz tube and annealed for about 4 weeks at a temperature of 1100 K. The annealed sample was powdered, and their XRD patterns showed single phase compound. The lattice parameters of the compounds are mentioned in table 5.1.

Table 5.1. The observed lattice parameters of the prepared compounds

Compound	Structure	Lattice Parameters	PCPDF ref.
URh$_3$	Cubic Pm-3m	a=4.100 Å	[4]
UIr$_3$	Cubic Pm-3m	a=4.024 Å	[5]

5.2.2 Experimental Details

In-situ High-Pressure X-ray Diffraction experiment (HP-XRD) was carried out using a Mao–Bell type diamond anvil cell (DAC) in the angle dispersive mode. The equation of state (EOS) of platinum was used for pressure calibration during the high-pressure

Chapter 5

High-Pressure Structural Stability of UX₃ (X=Rh, Ir) Type Compounds

5.1 Introduction

Many of the UX_3 compounds stabilize in Laves $AuCu_3$ type cubic structure. These compounds show high structural stability under high pressure [1,2]. The electronic structure calculations as a function of reduced volume show very little change in Density of States (DOS) at the Fermi level (E_F), justifying the structural stability of this compound under pressure [3]. In order to understand the structural stability and bonding nature of 5f-electrons in UX_3 type systems, high-pressure studies become important.

URh_3 and UIr_3 stabilize in the cubic $AuCu_3$ type structure at ambient conditions [4,5]. Although the U–U distance which is 4.100 Å and 4.023 Å for URh_3 and UIr_3, respectively, are much larger than the Hill limit (~3.5 Å), the 5f states in the system exhibit itinerant nature due to strong hybridization between the U-f and Rh-d electron orbitals [6–8]. Rh and Ir belong to the same group but to different period, and the bulk characteristics of the compounds URh_3 & UIr_3 resemble the transition elements i.e. show similar behavior [9]. Therefore, in order to test the structural stability of UX_3 type compounds in the same period, URh_3 and UIr_3 have been chosen for high-pressure study.

The results of the HPXRD studies on URh_3 & UIr_3 up to 25 GPa are presented in this chapter. In addition, electronic structure and the total energy of the URh_3 compound have been computed as a function of reduced volume in $AuCu_3$ and Ni_3Sn type structures

[13]   D. R. Rittman, K. M. Turner, S. Park, A. F. Fuentes, J. Yan, R. C. Ewing, and W. L. Mao, J. Appl. Phys. **121**, 45902 (2017).

[14]   Y. Hinatsu, N. Masaki, and T. Fujino, J. Solid State Chem. **73**, 567 (1988).

[15]   B. Shukla, N. R. Sanjay Kumar, M. Sekar, N. V. Chandra Shekar, H. Jena, and R. Asuvathraman, J. Alloys Compd. **672**, 393 (2016).

[16]   M. Sahu, K. Krishnan, M. K. Saxena, and K. L. Ramakumar, J. Alloys Compd. **482**, 141 (2009).

References

[1]   M. Zinkevich, Prog. Mater. Sci. **52**, 597 (2007).

[2]   M. Sahu, K. Krishnan, M. Saxena, and K. Ramakumar, J. Alloys Compd. **482**, 141 (2009).

[3]   M. Sahu, K. Krishnan, M. K. Saxena, and S. Dash, J. Therm. Anal. Calorim. **112**, 165 (2013).

[4]   J. J. Moore and H. J. Feng, Prog. Mater. Sci. **39**, 243 (1995).

[5]   J. J. Moore and H. J. Feng, Prog. Mater. Sci. **39**, 275 (1995).

[6]   H. Jena, R. Asuvathraman, and K. V. Govindan Kutty, J. Nucl. Mater. **280**, 312 (2000).

[7]   A. P. Hammersley, S. O. Svensson, M. Hanfland, A. N. Fitch, and D. Hausermann, High Press. Res. **14**, 235 (1996).

[8]   B. Shukla, N. R. Sanjay Kumar, M. Sekar, and N. V. Chandra Shekar, J. Instrumentaion Soc. India **46**, 75 (2016).

[9]   F. Birch, Phys. Rev. **71**, 809 (1947).

[10]   F. X. Zhang, J. Lian, U. Becker, R. C. Ewing, J. Hu, and S. K. Saxena, Phys. Rev. B **76**, 214104 (2007).

[11]   F. X. Zhang, M. Lang, Z. Liu, and R. C. Ewing, Phys. Rev. Lett. **105**, 15503 (2010).

[12]   H. Li, N. Li, Y. Li, Q. Tao, Y. Zhao, H. Zhu, Y. Ma, P. Zhu, and X. Wang, High Press. Res. **37**, 256 (2017).

HP-HT study was carried out on RE_6UO_{12} (RE=Sm, Gd, Dy) and the materials are found to be stable in rhombohedral structure up to (5.6 GPa, 673 K) for Sm_6UO_{12}, (5.0 GPa, 673 K) for Gd_6UO_{12} and (11.3 GPa, 673 K) for Dy_6UO_{12}. Bulk modulus at various temperatures have been estimated and all the compounds are found to be more compressible at high temperatures rendering the expected behavior under temperature. However, more softening is seen in Gd_6UO_{12} as compared to the other RE_6UO_{12} (RE=Sm, Dy) in the same temperature range. Gd_6UO_{12} has the largest volume thermal expansion coefficient at ambient pressure because of its weaker bonding in the lattice and a large drop in the thermal expansion coefficient has been observed at 1 GPa. However, Sm_6UO_{12} and Dy_6UO_{12} do not show such sharp change and their thermal expansion coefficients fall linearly with respect to pressure.

decrease in the thermal expansion coefficient of Dy_6UO_{12} with increasing pressure is found to be lower as compared to other compounds. This could be due to shorter lattice parameters in Dy_6UO_{12}.

6.4 Summary and Conclusion

High-pressure studies on Sm_6UO_{12}, Gd_6UO_{12}, and Dy_6UO_{12} have been carried out using synchrotron source at ambient temperature. The study reveals that the compounds are stable at lower pressures. a-axis of the lattice is found to be more rigid as compared to c-axis because of its corner sharing polyhedra along a-axis, though, high temperature study suggests c-axis to be more rigid due to high density of atoms along c-axis. The bulk moduli of the compounds Sm_6UO_{12}, Gd_6UO_{12} and Dy_6UO_{12} are estimated to be 157.7 GPa, 134.1 GPa, and 144.0 GPa, respectively. An abrupt softening in Gd_6UO_{12} has been observed which can be ascribed to the localization of 4-f electrons of Gd. At lower pressures, the peaks broadening can be due to the anion (oxygen) disorder. However at higher pressures, cations (RE^{3+}) also start moving leading to an increase in the (300) peak intensity and sharp decrease in the (211) and (122) intensities, simultaneously. The movement of cations leads to a possible unknown high-pressure disordered phase. At very high pressures, the compound is found to amorphize when both the anion and cation disorder takes place simultaneously. The anion disorder followed by cation disorder leads to collapse of polyhedra at high pressures. For the first-time pressure induced amorphization has been seen in rare earth uranates. The disorder pressure in the system has a correlation with the compressibility of the compound where disorder at lower pressures was seen in the compound with high compressibility.
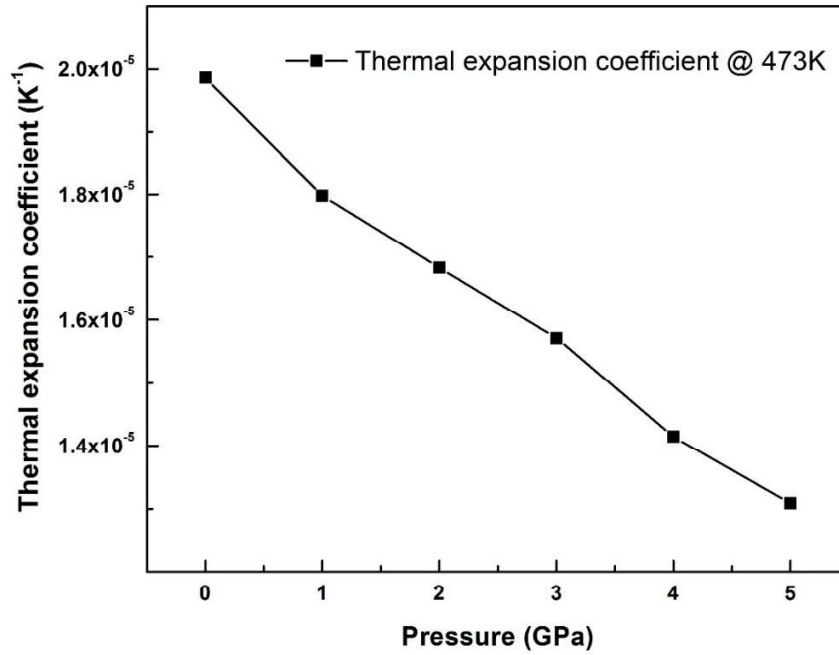
(c)

Figure 6.13: (c) Thermal expansion coefficients vs Pressure plot for Dy_6UO_{12}

It is evident from both the plots that thermal expansion coefficient decrease with increasing pressure affirming the usual behavior due to constraints applied by pressure. Furthermore, the rate of decrease in thermal expansion coefficient is faster at higher temperatures, and this is because of more softening at higher temperatures. A sharp decline in the thermal expansion coefficient was observed in Gd_6UO_{12} at 1 GPa where a total of 54% fall in the volume thermal expansion coefficient is seen in Gd_6UO_{12} as against 22% fall in Sm_6UO_{12} in the temperature range 293 K-673 K. Moreover, 9.4% fall was observed for Dy_6UO_{12} in the temperature range of 293 K-473 K. The high rate of change in volume thermal expansion coefficient at lower pressures makes it interesting and valuable for reactor technologies. The reason for different rates of decrease in thermal expansion coefficient in Gd_6UO_{12} can be addressed using charge density and density of state calculation. The
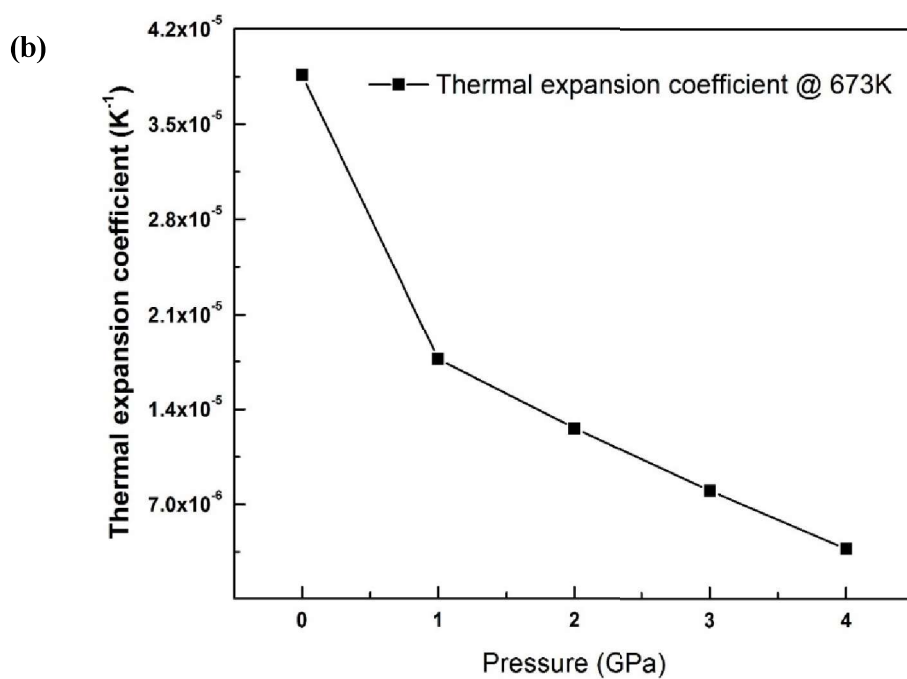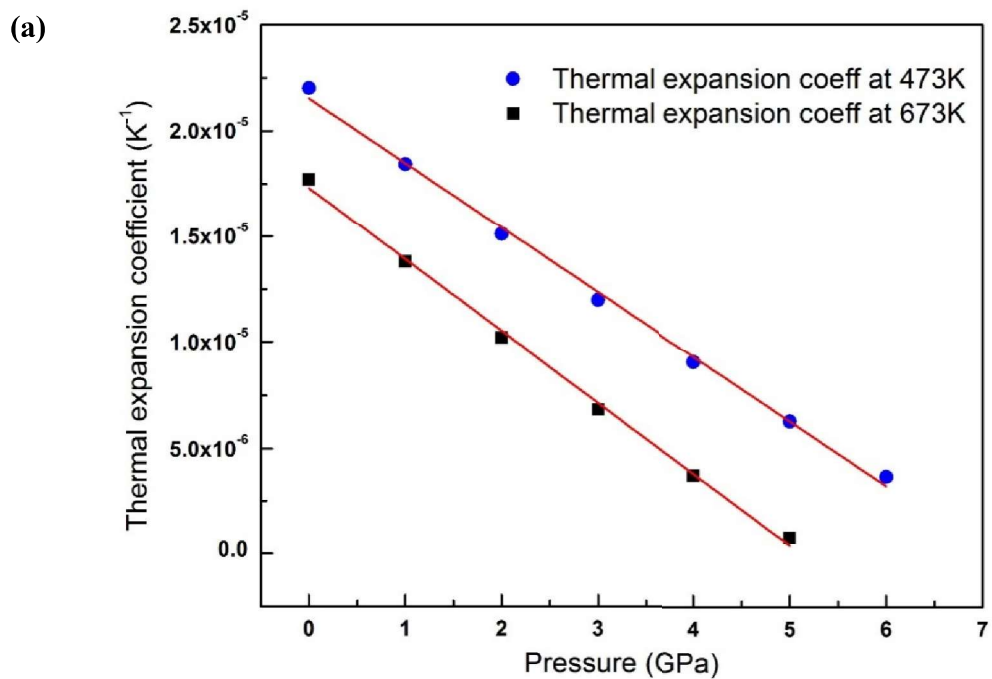
185

(a)

(b)

Figure 6.13*: Thermal expansion coefficients vs pressure plot for **(a)** Sm_6UO_{12}*
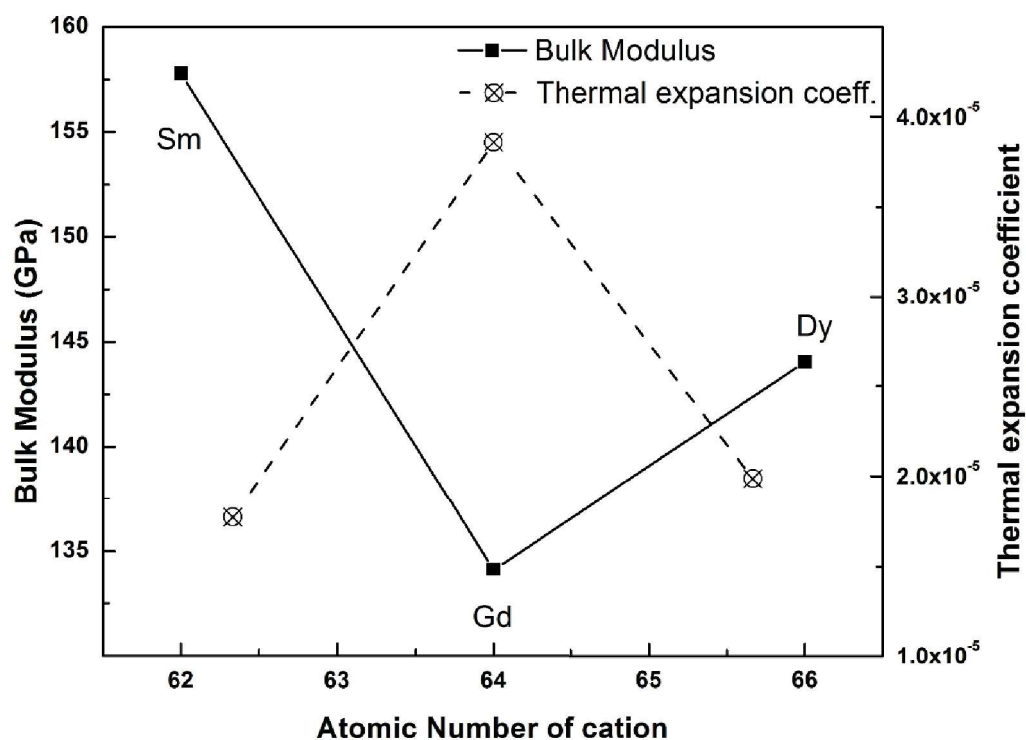
(b) *Gd_6UO_{12}*

184

Figure 6.12*: Bulk modulus & Thermal expansion coefficient vs atomic number of the cation at ambient pressure.*

The plot clearly reveals opposite trend between bulk modulus and thermal expansion coefficient i.e. higher the bulk modulus of the compound lower would be its thermal expansion. It can be correlated to the bond strength where stronger bonds in the material results in the higher bulk modulus, thereby, restricting the material to expand at high temperatures which is seen here in rare earth uranates.

Also, volume thermal expansion coefficients were estimated at higher pressures. Data from the P-V plot at high pressure were used to calculate the coefficients. Figure 6.13 shows the Thermal expansion coefficient vs Pressure plot for the Rare earth uranate compounds.

The general trend in all the compounds is to have lower bulk modulus at high temperatures. As the temperature increases, the materials become soft, hence more compressible. The softening in the compound arises because of softening of the lattice modes at elevated temperatures.

Thermal expansion behavior of the nuclear material, such as Rare-Earth Uranates in extreme conditions, is important from the nuclear technology as well as physics point of view, therefore, we have studied the thermal expansion of RE_6UO_{12} (RE=Sm, Gd, Dy) at high pressures. In this study, unit cell volumes were obtained from the P-V curve at different temperatures and constant pressure. A volume expansion of 1.57 % was observed for Gd_6UO_{12} compared to 0.71 % in Sm_6UO_{12} in the temperature range of 293 K - 673 K at ambient pressure. At ambient pressure, the thermal expansion coefficients of RE_6UO_{12} (RE=Sm, Gd, Dy) were calculated using the preliminary equation of thermal expansion of materials as given below:

$$\alpha_V = \frac{(V2 - V1)}{V1(T2 - T1)}$$

Thermal expansion coefficients at ambient pressure in the temperature range 293-673 K come out to be 17.7×10^{-6} K^{-1}, 38.6×10^{-6} K^{-1} and 19.86×10^{-6} K^{-1} for Sm_6UO_{12}, $Gd_6UO_{12,}$ and $Dy_6UO_{12,}$ respectively, which are plotted in figure 6.12 along with the bulk modulus data of the same compounds. It is noticeable from the thermal expansion coefficient data that Gd_6UO_{12} is a high thermal expansion material. The data matches with the earlier reported values [16].
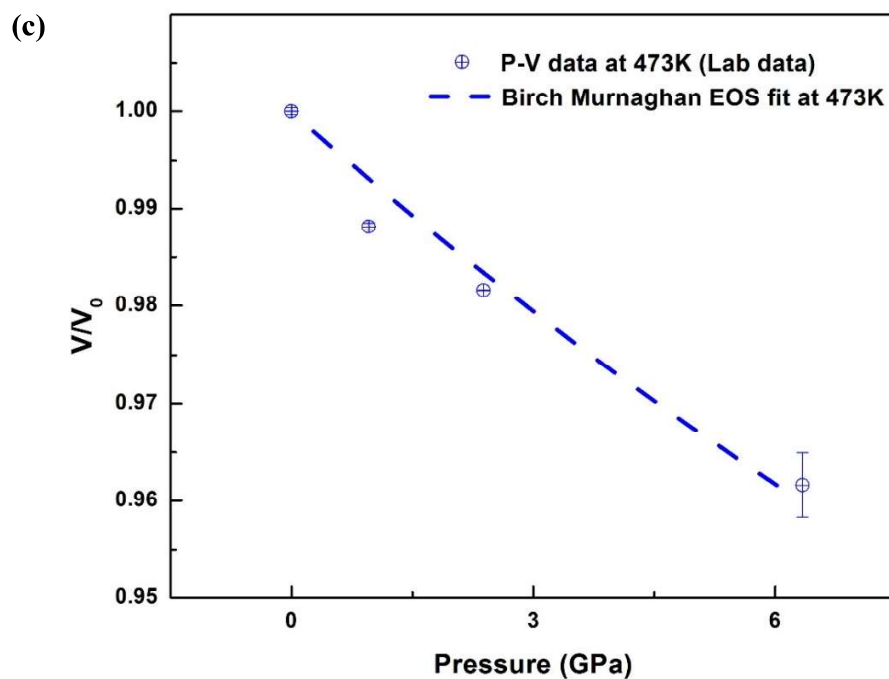
(c)

Figure 6.11: (c) P V Plot for Dy$_6$UO$_{12}$

Bulk modulus was estimated from the Pressure vs Volume data which was fitted with the 3rd order Birch Murnaghan equation of state. Estimated bulk modulus values at different temperatures are mentioned in table 6.4.

Table 6.4: Bulk modulus of the compounds at various temperatures

Compound / Temperature	Sm$_6$UO$_{12}$	Gd$_6$UO$_{12}$	Dy$_6$UO$_{12}$
293 K	157.7 GPa	134.1 GPa	144.0 GPa
473 K	139.1 GPa	-	134.0 GPa
673 K	123.7 GPa	96.0 GPa	-

181

The volume of the unit cell was estimated using the 2-theta reflection at different pressures for all the compounds. The plot of volume ($Å^3$) vs Pressure (GPa) is shown in figure 6.11.
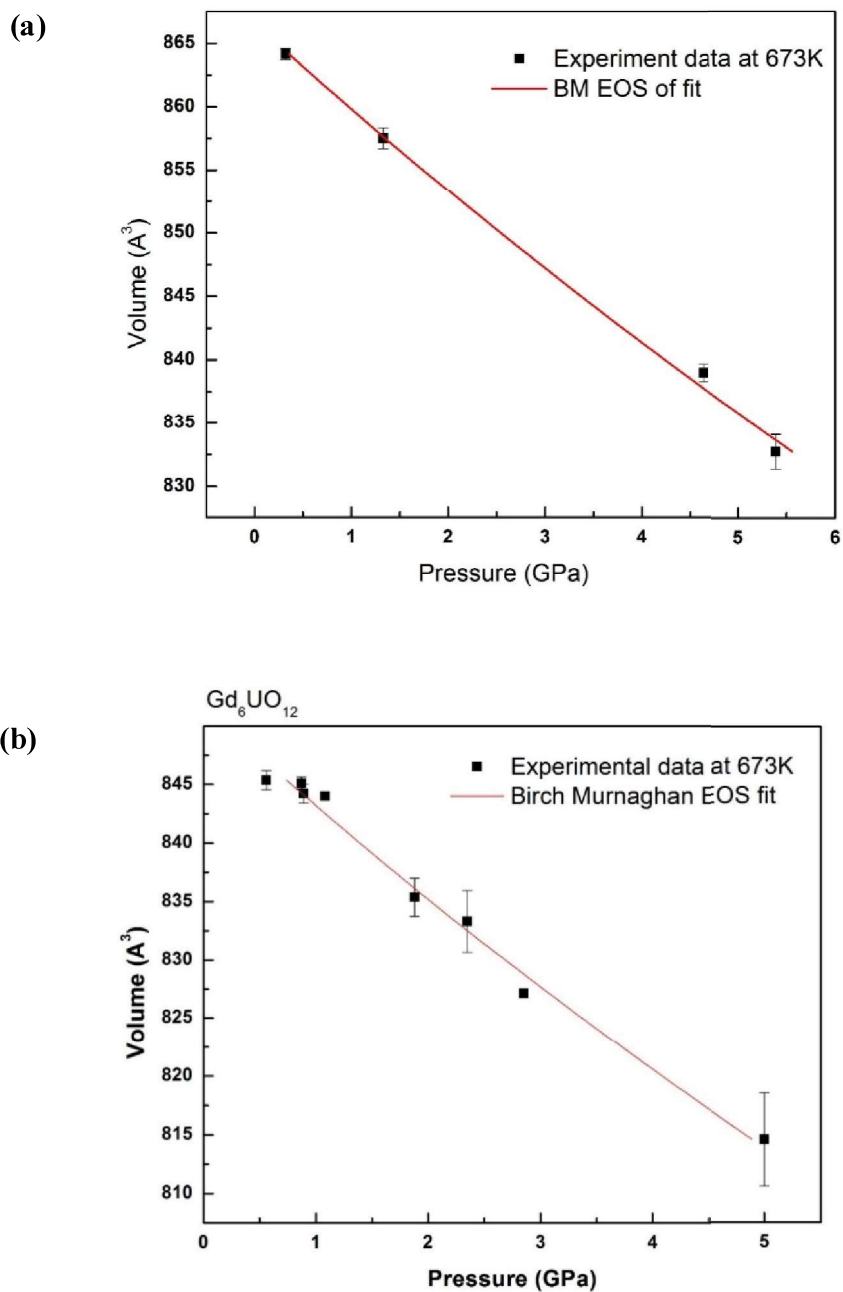
(a)

(b)

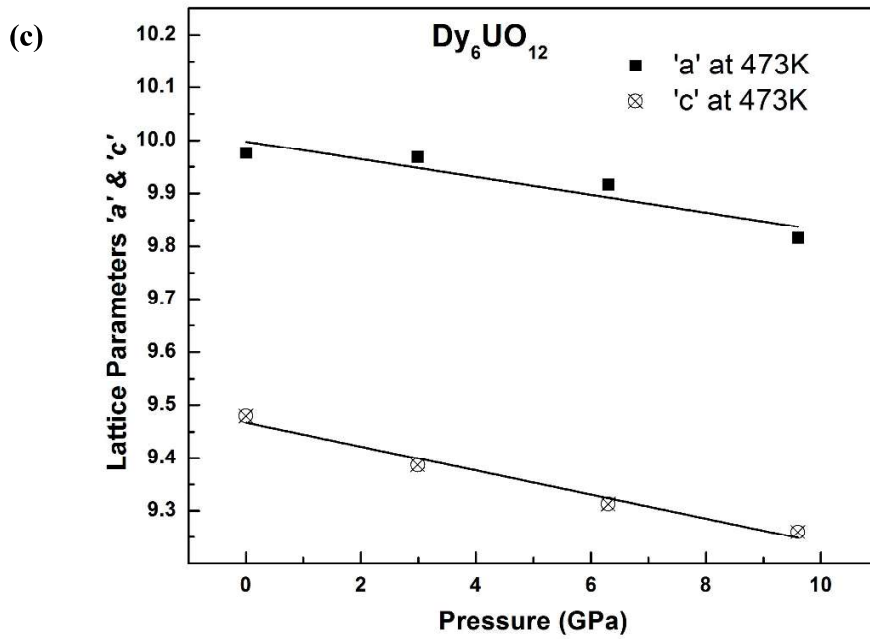***Figure 6.11:*** *P V Plot for **(a)** Sm₆UO₁₂ **(b)** Gd₆UO₁₂*

(c)

Figure 6.10: (c) Lattice parameter variation of Dy₆UO₁₂ at various temperatures

A continuous decrease in both a and c parameters with increasing pressure can be seen. c parameters compress readily as compared to a parameter. However, the rate of decrease in both the axes of Sm_6UO_{12} is higher at higher temperature. The contraction in the lattice parameters a and c of Sm_6UO_{12} is found to be 0.0187 Å/GPa and 0.0224Å/GPa, respectively at 473 K which increase to 0.0223 Å/GPa and 0.02436 Å/GPa, respectively at 673 K. The increase in the contraction rate is because of softening of the bonds at high temperatures. Even more softening is seen in the Gd_6UO_{12} where the contraction rate increases to 0.0275 Å/GPa and 0.033 Å/GPa along a and c-axis, respectively. At high temperatures, the rates of contraction of lattice parameters of Gd_6UO_{12} is found to be higher than that of Sm_6UO_{12} which can be attributed to the weaker bonding in the lattice. It arises because of localized nature of 4-f orbitals (half-filled) in Gadolinium causing the existence of weaker bonds in the Gd_6UO_{12} as compared to Sm_6UO_{12}.

179

Lattice parameters at different pressures and temperatures were obtained from the NIST*AIDS-83 software and are plotted in figure 6.10.
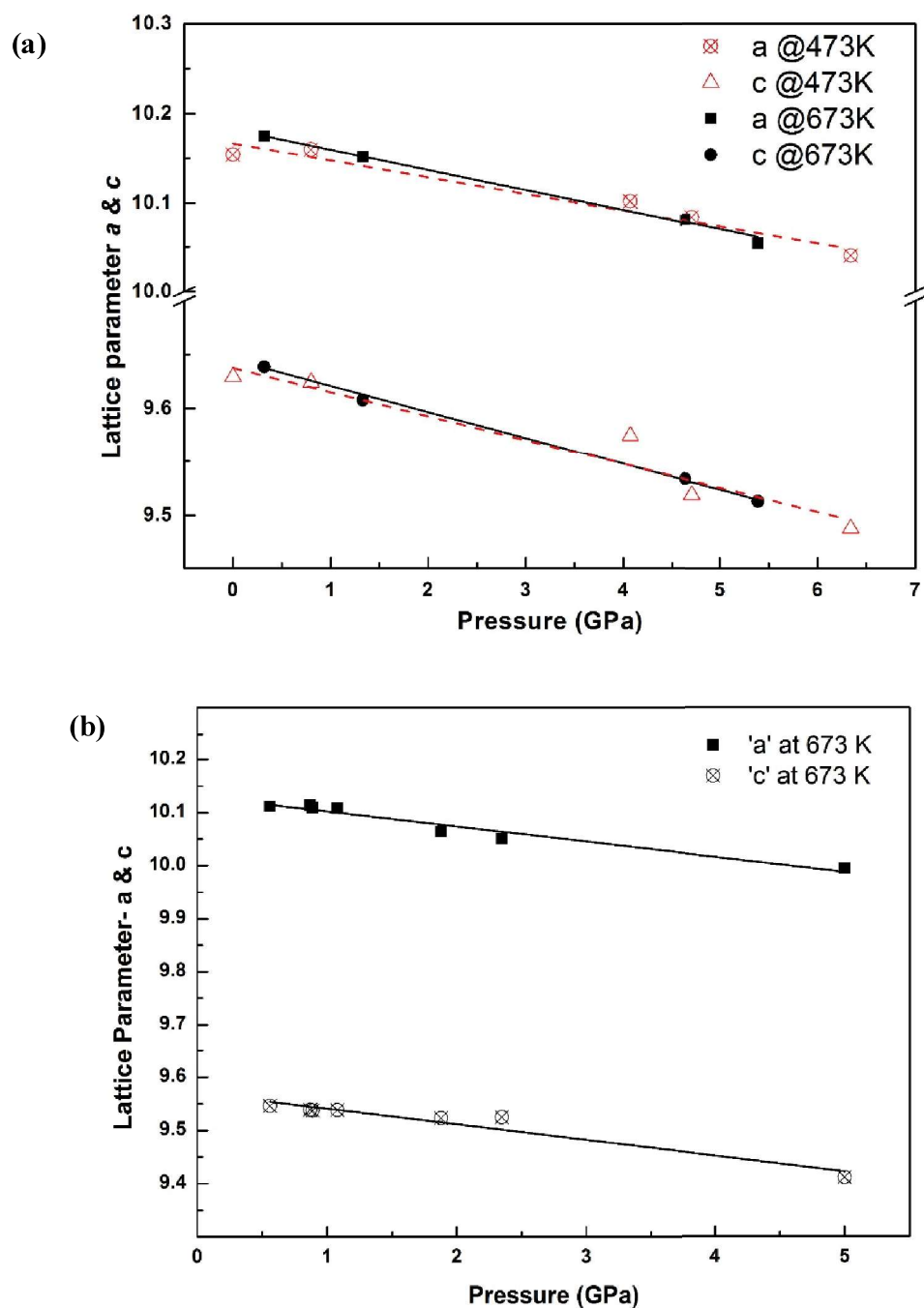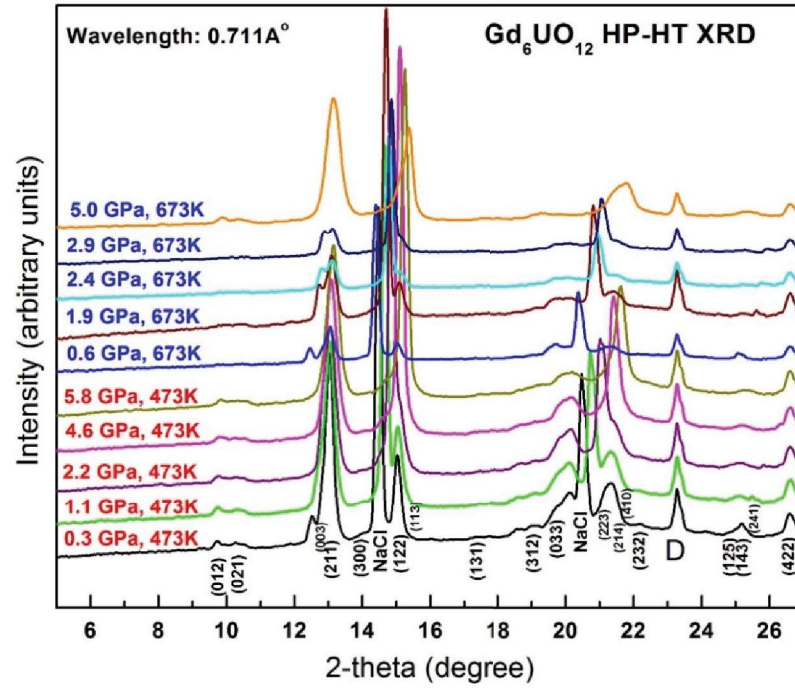

Figure 6.10: *Lattice parameter variation of (a) Sm₆UO₁₂ (b) Gd₆UO₁₂ at various temperatures*
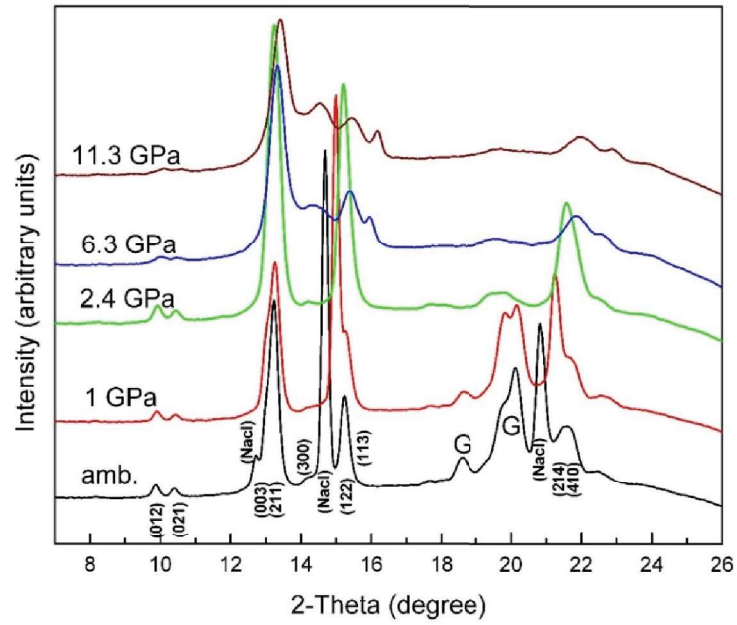
(b)

(c)

Figure 6.9: *HP-HT XRD patterns of **(b)** Gd₆UO₁₂ and **(c)** Dy₆UO₁₂, G & D represents peak from SS gasket & DAC, respectively.*

However, the general trend in the rare earth uranates could be a decreasing amorphization pressure with increasing atomic number of rare earth cation.

6.3.2 High-pressure study of RE_6UO_{12} (RE=Sm, Gd, Dy) at high temperature

High Pressure and high-temperature X-ray diffraction study were carried out up to 5.6 GPa, 673 K for Sm_6UO_{12}; 5.0 GPa, 673 K for Gd_6UO_{12}; and up to 11.3 GPa, 673 K for Dy_6UO_{12} [15]. Intensity vs 2-theta plot [figure 6.9] shows that all the reflections can be traced up to the highest pressure and temperature studied, signifying the fact that the material is stable in its parent rhombohedral structure.

The NaCl peaks overlap extensively with the sample *(122)* peak at high pressure. Also, sample peaks *viz. (003) & (211)* overlap and peak fitting was carried out to estimate the exact angle of diffraction of the sample as well as that of NaCl.
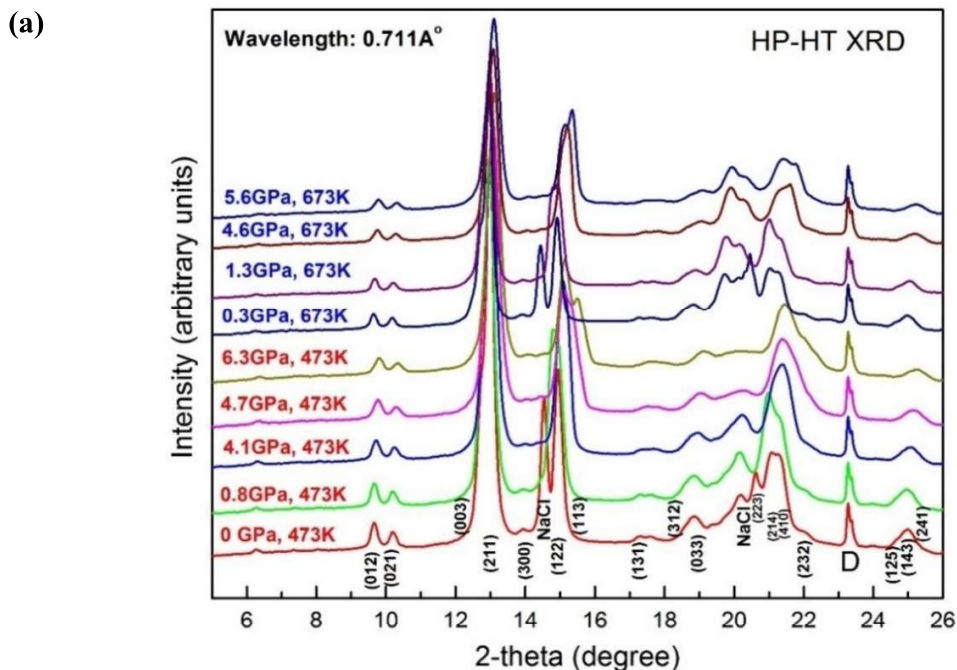

Figure 6.9: (a) *HP-HT XRD patterns of Sm_6UO_{12}, D represents peak from DAC*

2. Effect of disorder on polyhedra: Random tilting of the polyhedra in the lattice at lower pressures and distortion in the polyhedra at very high pressures are the major changes causing PIA. At ambient pressure, the polyhedra are highly distorted [14]. The Rietveld refinements of Sm_6UO_{12} at high pressures state that samarium atom moves along the *(300)* plane. Therefore, it can be concluded that RE polyhedra are mostly affected by pressure. Also, lattice parameter behavior with pressure reveals that c-axis is shorter than a-axis and decreases faster than a-axis. This leads to 'shorter RE-O' bonding and sharp decrease along c-axis resulting in even more distortion in the REO_6 polyhedra which may collapse at high pressures. Therefore, increased distortion in the polyhedra might be one of the reasons for the onset of the disorder and finally amorphization at higher pressures.

However, Raman spectroscopy at high pressure may provide insight of the RE-O bonding in the lattice which may explain the oxygen and cation bonding at high pressures. The disorder/amorphization of the compound is found to be partially reversible upon release of pressure which is indicated by the partial strengthening and sharpening of few reflections [figure 6.1].

The disappearance (not amenable to fit or find its position) of peaks in compound Sm_6UO_{12}, Gd_6UO_{12} and Dy_6UO_{12} appear at different pressures like ~27 GPa, ~20 GPa, and ~21 GPa, respectively. The trend in the bulk modulus and the disorder pressure are found to be similar. Therefore, the conclusion can be arrived in the terms of compressibility which affirms that softer compounds get easily distorted and amorphized at lower pressures than those having lower compressibility. The softness can be attributed to the weaker bonding strength in Gd_6UO_{12} due to non-participation of 4-f electrons in gadolinium atom.

Amorphization

Beyond 28.0 GPa, 17.0 GPa and 21.6 GPa in Sm_6UO_{12}, Gd_6UO_{12} and Dy_6UO_{12}, respectively, the peaks broaden in such a manner that peaks are not traceable and the quality of data is not amenable for refinement or lattice parameter estimation. The disorder in the system sets in, which further increases at higher pressures. The disorder is found to increase such that the system has a tendency to amorphize at high pressures. Pressure-induced amorphization (PIA) is reported for the first time in rare earth uranates. The reason for the PIA can be understood in terms of disorder and its effects on the lattice as follows:

1. Origin of Disorder: Sharp increase in the FWHM & rapid decrease in the intensities of the peaks at lower pressure due to anions and movement of RE^{3+} cation at high pressures is conjectured to cause the stabilization of a disordered phase which finally might lead to amorphization. The argument of origin of the disorder by anion followed by cation seems more probable. A disorder was generated by oxygen atoms (anion). At high pressures, movement of cations, mostly along the *a* and *b* axes, has also been inferred from refinement. The movement leads to a sudden increase in the *(300)* intensity with significant broadening and a sharp decrease in the *(211)* and *(122)* intensities. Also, in the same pressure range, a new peak starts appearing just before the *(003)* peak, which is an indication of a new disordered phase. A mismatch in the intensity of *(122)* peak also supports the argument of formation of a high-pressure phase. A similar high-pressure disordered phase has been reported earlier in pyrochlore system [10–13]. In the present case, amorphization due to disorder of the anions followed by cations is well supported by the series of events occurring in high-pressure X-ray diffraction patterns.

The refinement gives fitting of high intense *(300)* reflection when samarium positions are refined, clearly indicating the enhanced contribution from samarium atom [figure 6.7]. With the new atomic position of Sm in Sm_6UO_{12}, lattice structure was generated and compared with the old Sm_6UO_{12} structure. The comparison indicates that Samarium atom in the unit cell moves towards the *(300)* plane and away from *(211)* and *(122)* planes, causing increase in the intensity of *(300)* peak and sharp decrease in the intensity of *(211)* and *(122)* peaks *i.e.* intensity of *(300)* reflection increases at the cost of *(211)* and *(122)* reflections. Figure 6.8 shows the movement of the samarium atoms in the unit cell. However, charge density calculation may enlighten the subject more explicitly.
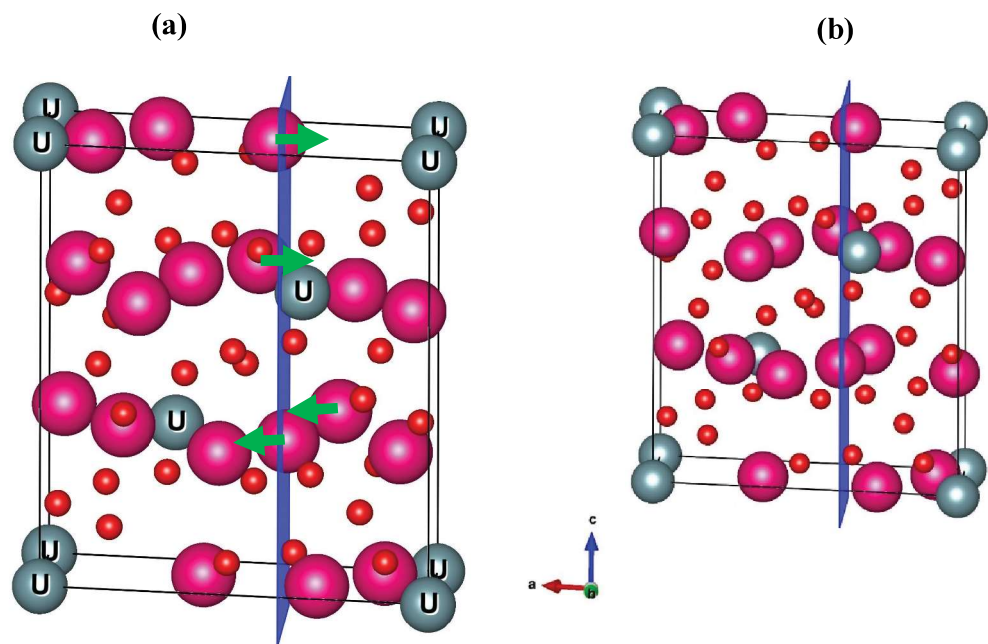

Figure 6.8: *A unit cell of Sm_6UO_{12}.* ***(a)*** *P=ambient* ***(b)*** *P=27.0 GPa. The figure shows the movement of the samarium atoms towards (300) plane when pressure is increased from ambient to 27.0 GPa*

173

just 3% peak, shoots over the 100% intense peak. The peculiar behavior of *(300)* reflection becomes interesting when thought in terms of charge density in the plane. This observation is indicative of an increase in the charge density in the plane above 27.0 GPa. To clarify Rietveld refinement of atomic positions were carried out in the pressure range. The atom position of the samarium atom was refined and tabulated in table 6.3.
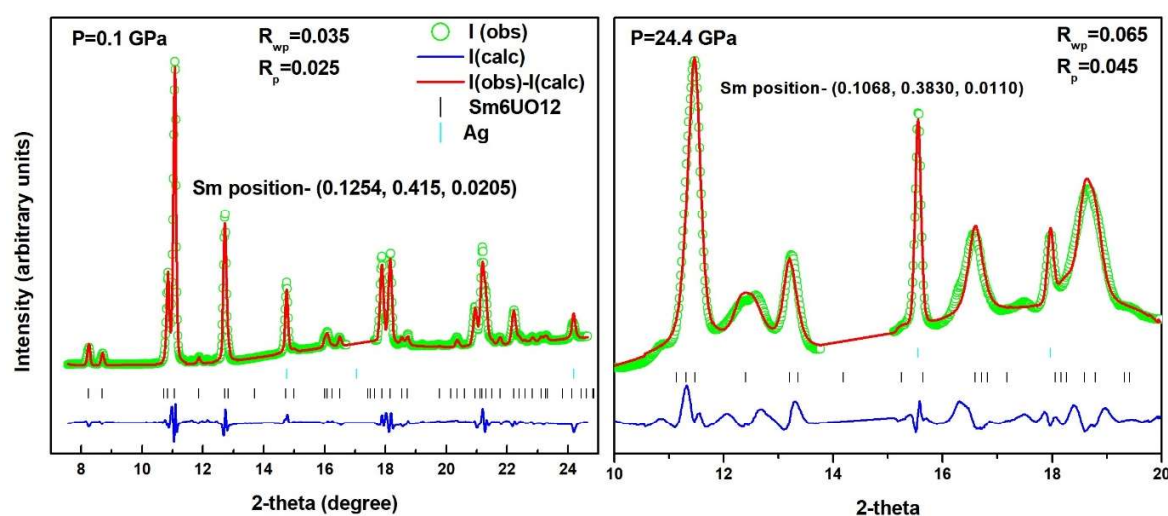

Figure 6.7: *Rietveld refined XRD pattern of Sm₆UO₁₂ at 0.1 GPa (left) & 24.4 GPa (right)*

Table 6.3: *Rietveld refined atomic position of 'Sm' in Sm₆UO₁₂ at different pressures.*

Pressure (GPa)	X	Y	Z
amb.	0.1254	0.415	0.0205
16.7	0.1233	0.4046	0.0171
19.8	0.1222	0.4177	0.0184
22.9	0.1097	0.3824	0.0152
24.4	0.1068	0.3830	0.0110
27.0	0.0876	0.3547	0.0084
30.4	0.0490	0.3333	0.0012

The broadening cannot be attributed to the quasi-hydrostaticity of the pressure transmitting medium because FWHM of silver, present in the sample chamber, doesn't show such broadening throughout this pressure region. A sudden increase in the FWHM and rapid fall in the intensities are very interesting from the point of view of atomic arrangement inside the unit cell. To know the reason for large broadening of the peaks, Rietveld refinement was carried out on Sm_6UO_{12}'s high-pressure XRD patterns. Since uranium atom has a special position in the atomic cell, the samarium atom position was refined at various pressures. The result shows that samarium position doesn't change up to 19.8 GPa.

However, FWHM vs pressure & HP-XRD plot reveals significant broadening & sharp decline in the Bragg's peak intensities, respectively, even below 19.8 GPa. As uranium and samarium position does not change up to 19.8 GPa, the increase in FWHM & sharp decline of the intensities can be attributed to oxygen (anion) disorder happening between 10 GPa and 19.8 GPa. In this pressure interval, the lattice is unable to sustain the energy supplied, hence, the polyhedra may try to tilt keeping the central samarium (cation) fixed as tilting of polyhedra is easier than moving a heavy cation. Thus anion disorder may result in sharp decline of the Bragg's peaks observed between 10 GPa -20 GPa.

Above 19.8 GPa and below 27.0 GPa in Sm_6UO_{12} following features are seen in the diffraction pattern- appearance of new peak, mismatch in the intensity of peaks during Rietveld refinement, sudden increase in the intensity of *(300)* peak, sharp decrease in the intensity of *(211)* and *(122)* peaks & uniform broadening of all the peaks. Reflection *(300)* shows an increase in the strength, and the intensity of the peak increases with increasing pressure. This increase in the intensity with its broad FWHM, renders other nearby reflections *(211)* and *(122)* to merge. At higher pressures, the reflection *(300)*, which was

orbitals, which is considered to be stable compared to the partially filled orbitals, indicating that these outer shell 4-f electrons are localized and do not participate in the bonding.

The density of states and charge density calculations are required to quantitatively explain the nature of bonding, its variations with respect to pressure and the localization of the 4-f electrons in Gd_6UO_{12} which has been seen in our high-pressure experiments. More compressibility of Gd_6UO_{12} can be related to the probable low density of states at Fermi energy can make the 4-f electrons localized and lead to a weaker bonding in Gd_6UO_{12}. This may be the cause of the observed lower bulk modulus as compared to other rare earth uranates which also reflects in highly compressible lattice parameters at high pressures. However, the argument must be supported by the computation.

High-pressure diffraction patterns of RE_6UO_{12} were evaluated, and it was found that beyond 10 GPa, FWHM of the reflections increases sharply along with the rapid fall in the intensities. A plot of FWHM of Sm_6UO_{12} is shown Figure 6.6.
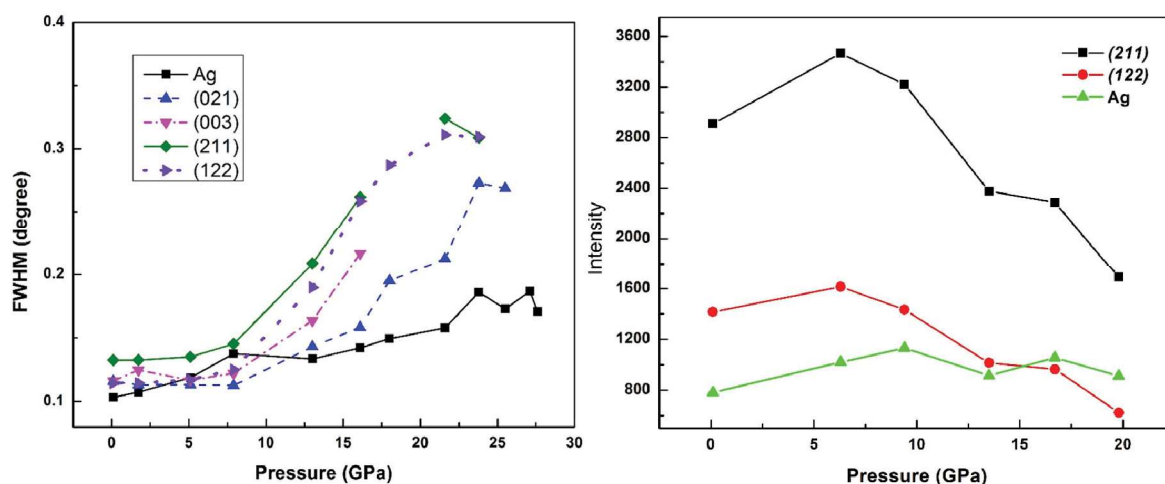

Figure 6.6: *FWHM of Sm_6UO_{12} as a function of pressure (left), Intensities of the sample & pressure calibrant at higher pressures for comparison (right)*
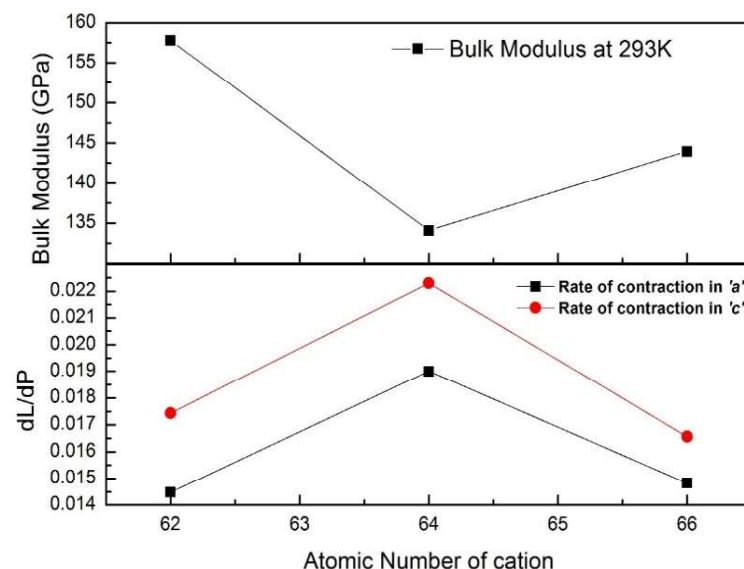
170

Figure 6.5: *Bulk modulus [top] and rate of change of lattice parameters [bottom] with pressure (dL/dP) as a function of atomic number of cation*

The bulk modulus is expected to decrease continuously as the atomic number of the cation increases. The reason is the decrease in cation-RE^{3+} radius which results in a decrease in cation-cation distance. Shorter cation-cation distance increases the repulsion between them, causing instability of the lattice. Moreover, lesser cationic radius causes localization of the 4-f electron and hence weaker bonding. Sm_6UO_{12} and Dy_6UO_{12} follow the usual trend of decrease in the bulk modulus. However, a sudden drop in the bulk modulus has been observed in Gd_6UO_{12} [figure 6.5, bottom] indicating Gd_6UO_{12} to be a softer compound. The same is reflected in the lattice parameters where it follows the similar trend. The rate of decrease in lattice parameters of Gd_6UO_{12} is found to be higher compared to that of Sm_6UO_{12} and Dy_6UO_{12} [figure 6.5]. The abnormality in the bulk modulus of the compound may be explained in terms of localization of electrons. Gadolinium has half-filled 4-f
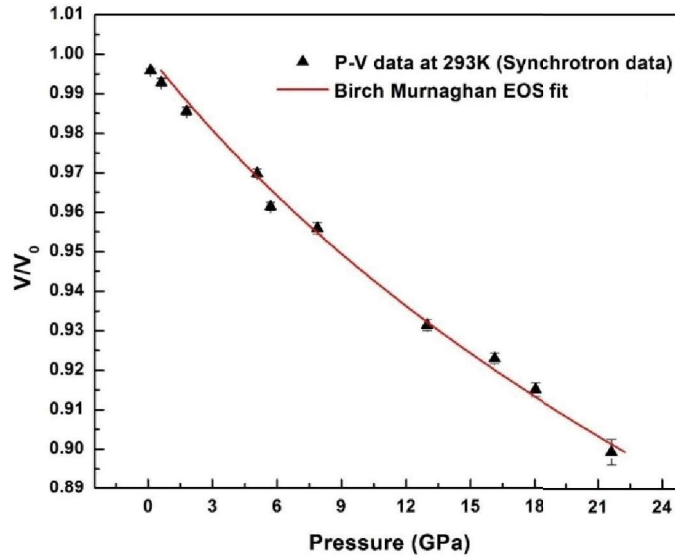
(b)
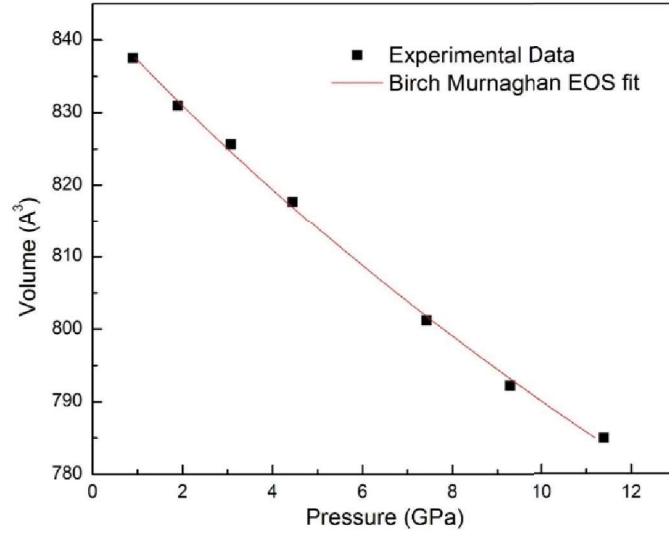
(c)

*Figure 6.4: P-V data and Birch Murnaghan Equation of state fit for **(b)** Gd_6UO_{12} and **(c)** Dy_6UO_{12}*

The nonlinear BM-EOS fit yields bulk modulus 157.7 GPa, 134.1 GPa and 144.0 GPa for Sm_6UO_{12}, Gd_6UO_{12}, and Dy_6UO_{12}, respectively. The bulk modulus vs atomic number of cation (RE^{3+}) is plotted in figure 6.5.

168

Two REO_6 polyhedra share edges, whereas, UO_6 and REO_6 polyhedra are linked at one corner. Corner-sharing is considered to be more stable as compared to the edge-sharing by Pauling's rule for ionic structures. Hence, the compression along the edge-sharing REO_6 polyhedra is more at high pressures. The converse happens along the c-axis where REO_6 and UO_6 share edges. Moreover, there are more number of polyhedra along a-axis as compared along c-axis. Since polyhedra determine bonding nature of the crystal and number of bonds are more along a-axis, therefore, making it difficult to compress. Thus, the Pauling's rule for ionic structure and more number of polyhedra along a-axis, lead to the observed trend in the lattice parameter variation as a function of pressure.

It is noticeable from the diffraction plots that the rhombohedral reflections are traceable up to the pressure 28.0 GPa, 20.0 GPa, and 21.6 GPa for the compounds Sm_6UO_{12}, Gd_6UO_{12}, and Dy_6UO_{12}, respectively. The pressure-volume data have been fitted to 3rd order Birch Murnaghan Equation of State (BM-EOS)[figure 6.4] [9].
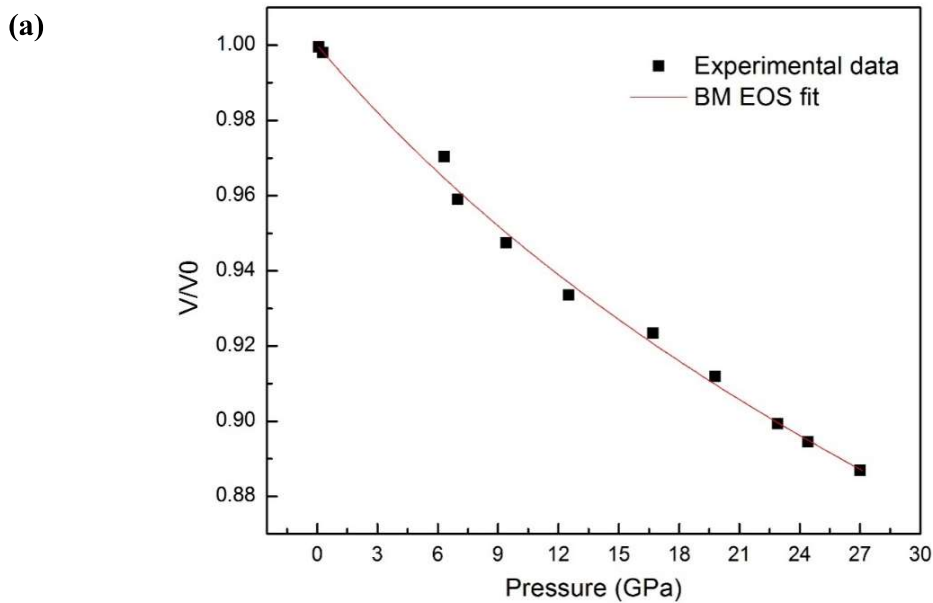

(a)

Figure 6.4: (a) P-V data and Birch Murnaghan Equation of state fit for Sm_6UO_{12}

167

Above table shows that $\left(\frac{dc}{dP}\right)$ is always greater compared to $\left(\frac{da}{dP}\right)$ stating that compression along c-axis is more compared to a-axis. Larger drop in the c-axis implies that c-axis compresses more readily and the ratio c/a decreases. This indicates that a-axis is more rigid under pressure as compared to c-axis. However, H. Jena *et al.* studied RE_6UO_{12} under high temperature showing that thermal expansion coefficient is more along a-axis (10.70×10^{-6} K^{-1}) than along c-axis (8.51×10^{-6} K^{-1}), which indicates that a-axis is more free to move 'under temperature' than c-axis. The reason for the rigidity of 'c' axis under temperature was ascribed to the large density of atoms along c-axis [6].

However, rigidity of the a-axis with respect to pressure can be addressed using the polyhedral representation of the unit cell and Pauling rule for ionic structures. The crystal structure of RE_6UO_{12} can be visualized using polyhedra representation wherein, two UO_6 polyhedra are separated by two REO_6 polyhedra along the c axis. A unit cell of the compound is shown in figure 6.3.
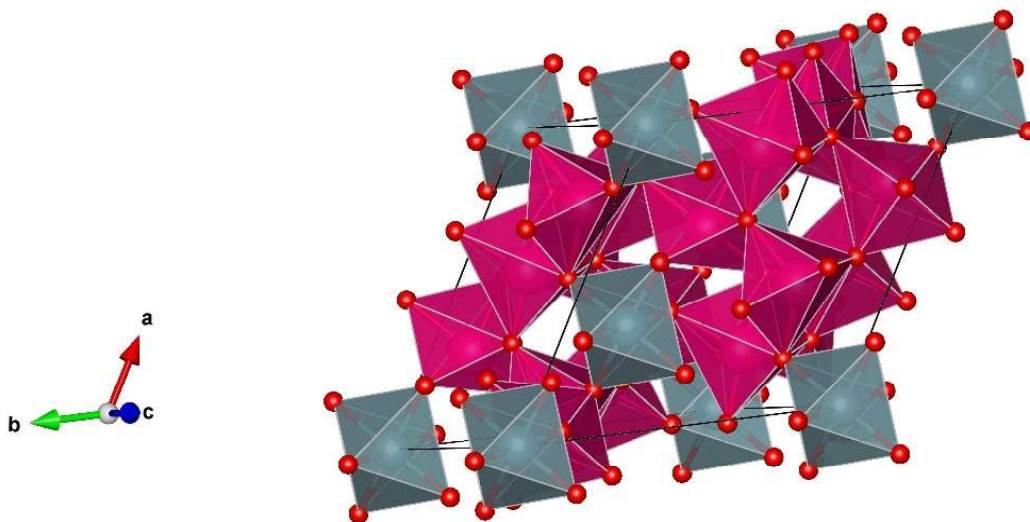

Figure 6.3: *Polyhedral representation of unit cell of RE_6UO_{12}*

(c)

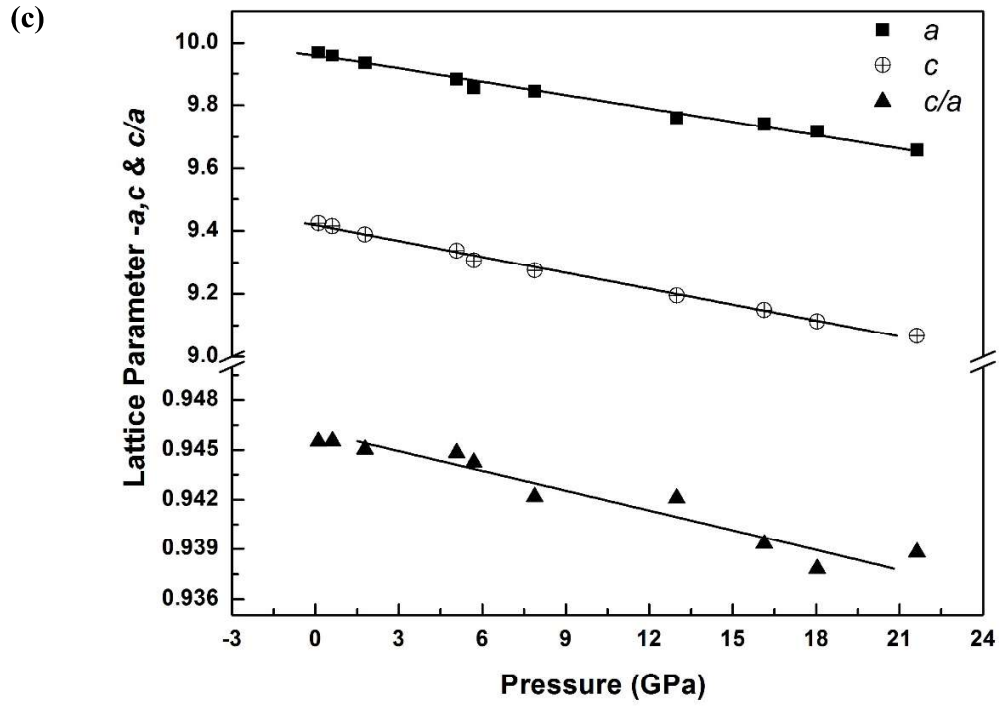*Figure 6.2: (c) Lattice parameters and 'c/a' variations of Dy_6UO_{12} with respect to pressure*

Apart from contraction of lattice parameters under pressure, different rates of change in the 'a' and 'c' values of the rhombohedral structure are observed i.e. the values of $\left(\frac{dL(a,c)}{dP}\right)$ are different for each of the compounds, which are list below in table 6.2.

Table 6.2: Rate of change in the lattice parameters with respect to pressure

Compound	$\left(\frac{da}{dP}\right)$ at 293K, (Å/GPa)	$\left(\frac{dc}{dP}\right)$ at 293K, (Å/GPa)
Sm_6UO_{12}	0.0145	0.0174
Gd_6UO_{12}	0.0190	0.0223
Dy_6UO_{12}	0.0150	0.0180
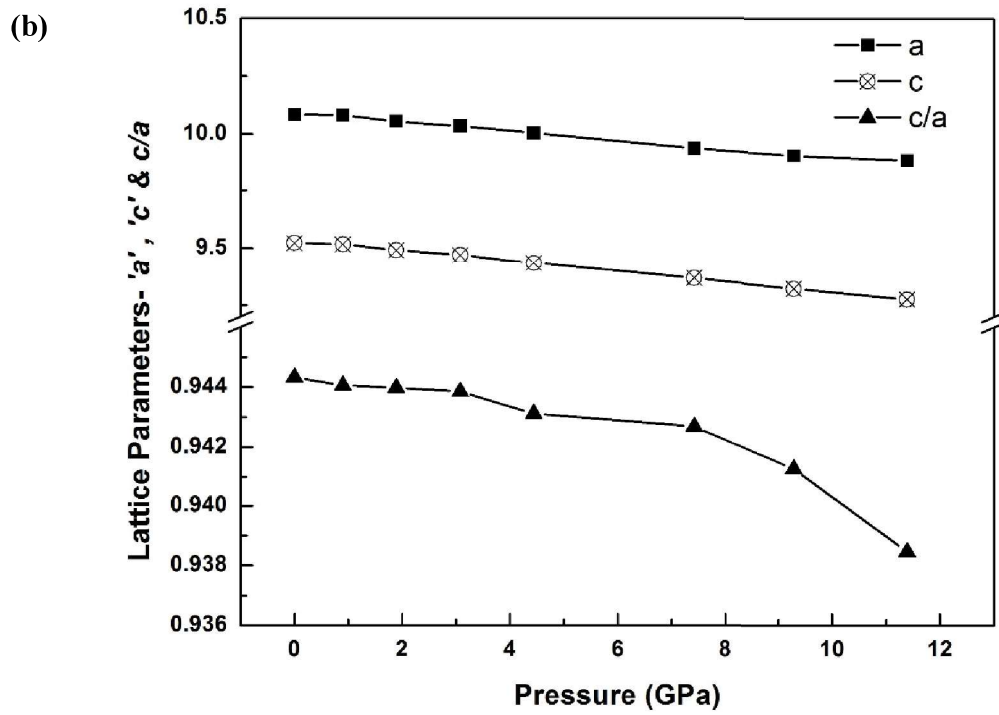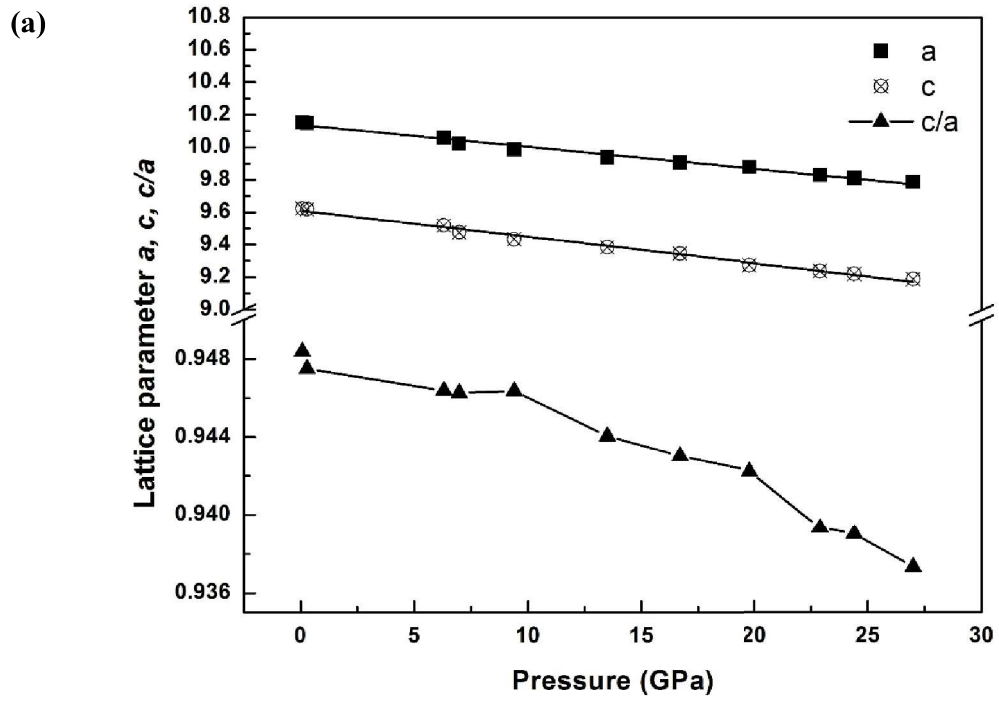
Figure 6.2: *Lattice parameters and 'c/a' variations of (a) Sm₆UO₁₂ (b) Gd₆UO₁₂*

with respect to pressure

164

(d)
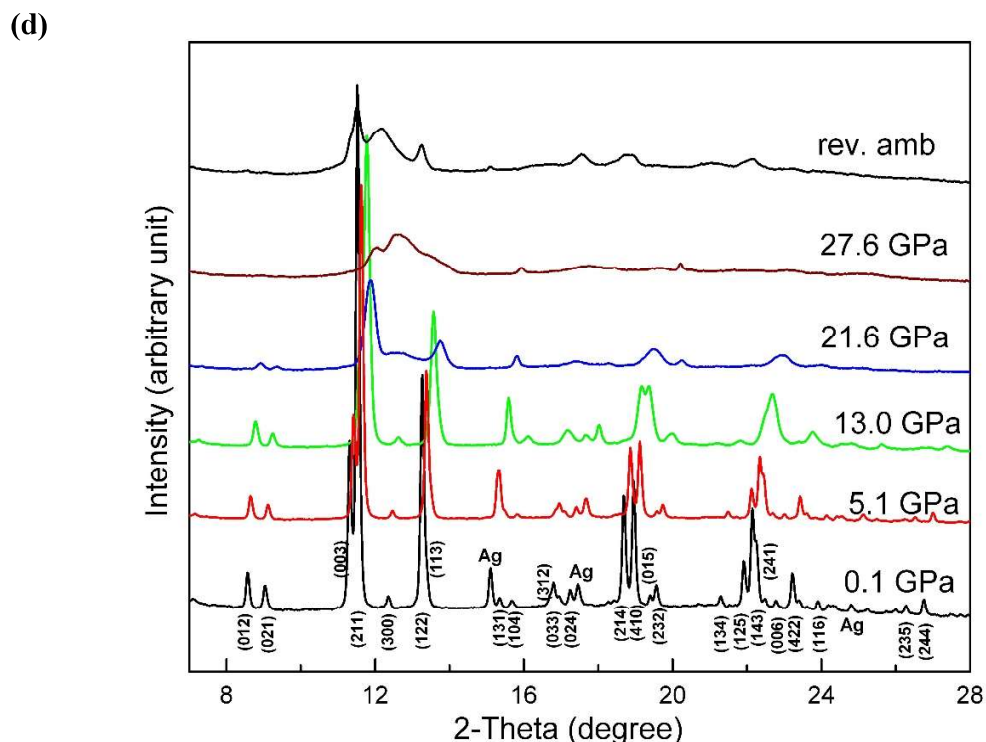
Figure 6.1: (d) HP-XRD plots of Dy_6UO_{12} using synchrotron source

Typical peak broadening due to pressure gradient is observed in the diffraction patterns under compression for all the compounds. The evolution of the reflections in the diffraction patterns show that materials remain in the rhombohedral structure. It is evident from the diffraction patterns that all the peaks are traceable up to pressure 28.0 GPa, 20.0 GPa, and 21.6 GPa for Sm_6UO_{12}, Gd_6UO_{12}, and Dy_6UO_{12}, respectively. The high-pressure diffraction data are mapped to the rhombohedral structure and lattice parameters have been obtained using NIST*AIDS-83 software. Lattice parameters a and c decrease in a linear fashion with increasing pressure which is due to the isotropic compression of the unit cell of the lattice. The lattice-parameter variations with respect to pressure are shown in Figure 6.2.

163

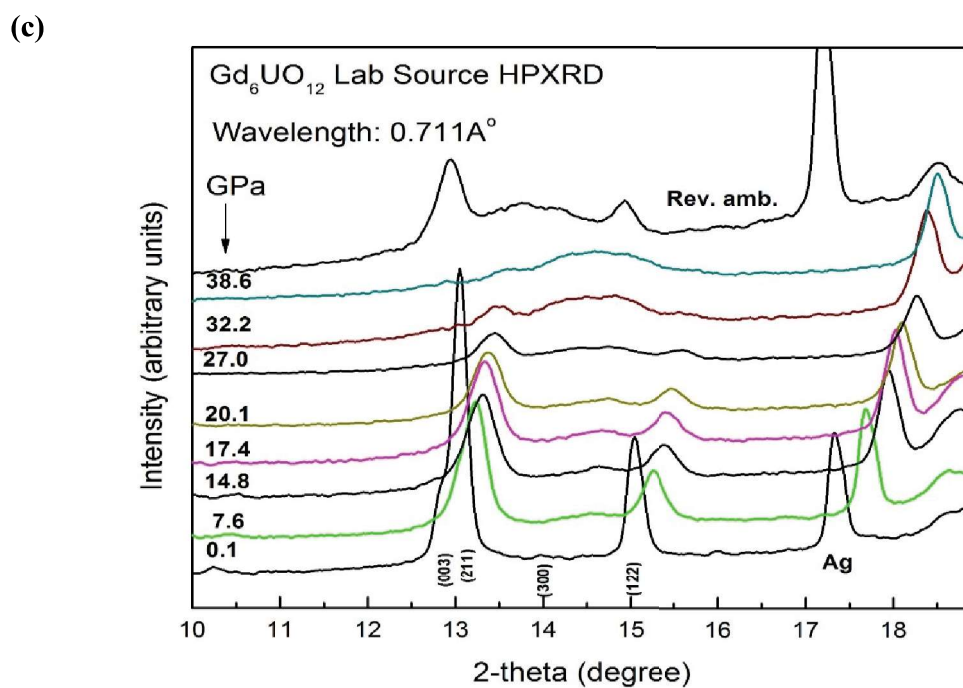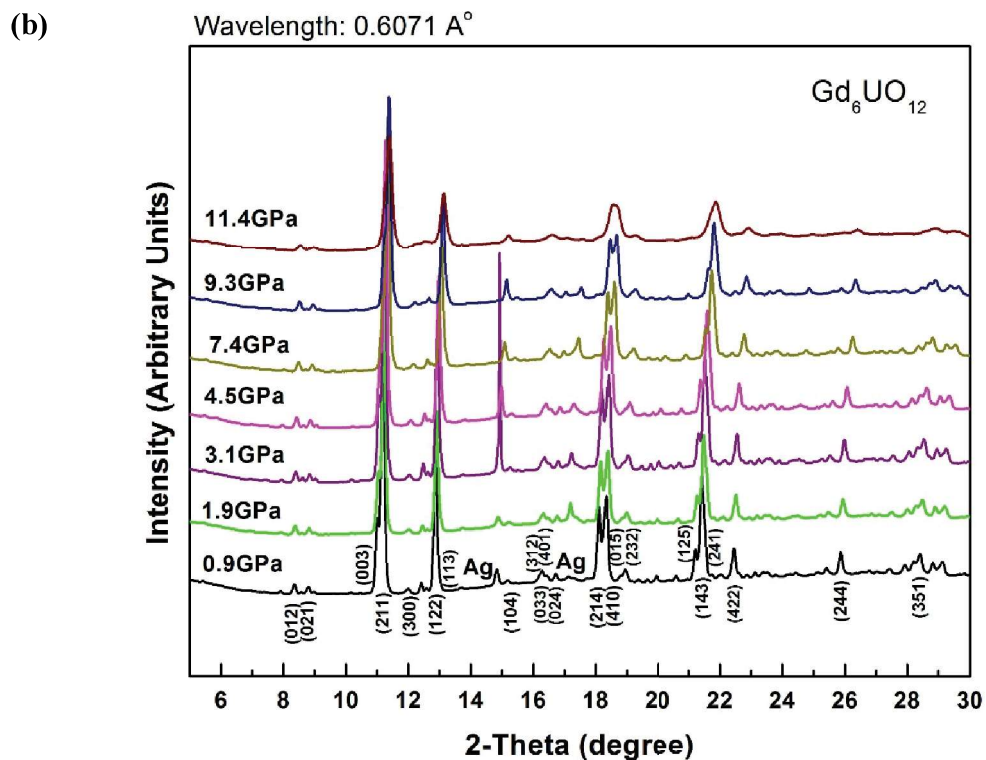**Figure 6.1:** HP-XRD plots of **(b)**. Gd$_6$UO$_{12}$ using synchrotron source **(c)**. Gd$_6$UO$_{12}$ using laboratory x-ray source

162

and (11.3 GPa, 673 K), respectively. For the compounds Sm_6UO_{12} and Gd_6UO_{12}, XRD patterns were collected in the angle dispersive mode for 1h with a relaxation time of 30 min between successive temperature intervals, however, for Dy_6UO_{12} the duration of data collection was 30 min. Finally, the data obtained from mar345 IP detector were analyzed using Fit2D image processing software. Least square analysis using NIST*AIDS-83 were carried out to estimate lattice parameters at various pressures and temperatures.

6.3 Results and Discussion

6.3.1 High-pressure study of RE_6UO_{12} (RE=Sm, Gd, Dy) at ambient temperature

The materials Sm_6UO_{12}, Gd_6UO_{12}, and Dy_6UO_{12} have been studied under high pressure up to ~42 GPa, ~39 GPa and ~28 GPa, respectively. Angle-dispersive X-ray diffraction patterns are shown in figure 6.1 at selected pressures.
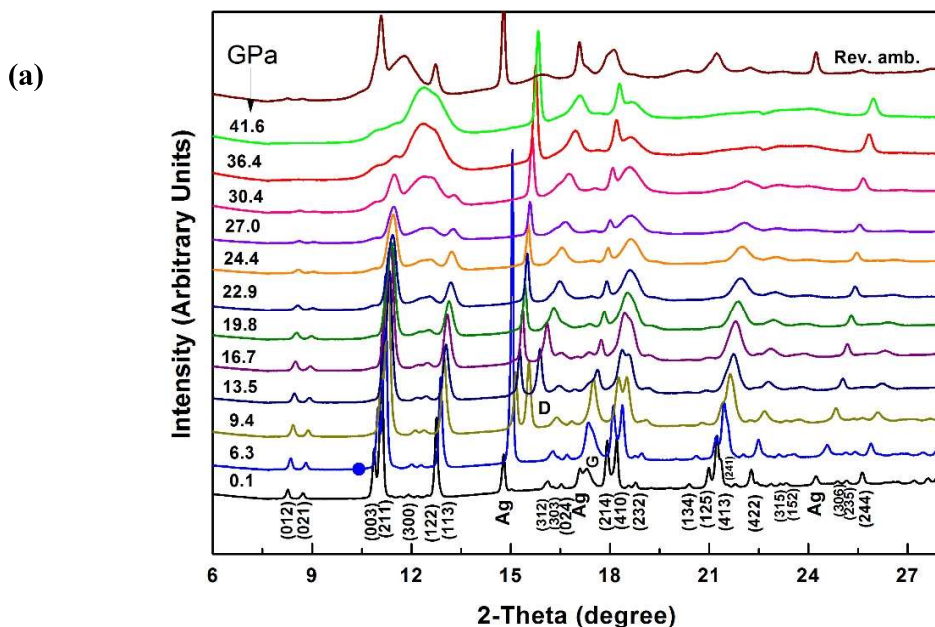

Figure 6.1: **(a)** HP-XRD plots of Sm_6UO_{12} using synchrotron source, 'G' and 'D' represents reflections from SS gasket and Diamond, respectively.

dispersive mode and transmission geometry. mar345 IP detector was used for collecting diffracted X-rays and obtained 2D data were converted to Two theta vs Intensity using Fit2D software [7]. NIST*AIDS-83 software was used to get the lattice parameters at various pressures. XRD study was carried out on compounds RE_6UO_{12} (RE=Sm, Gd, Dy) using synchrotron radiation up to a pressure of 42 GPa, 12 GPa, and 28 GPa, respectively. The pressure was dropped slowly in steps and diffraction patterns was taken after a relaxation time of 30 min at each step (reverse cycle).

Further studies on Gd_6UO_{12}, up to more higher pressures, was carried out using Rigaku ULTRAX18 (18 kW) rotating anode X-ray generator with wavelength 0.7107 Å. Mao-Bell type DAC with similar loading technique was used to carry out HP study up to a pressure of 39 GPa. A slit of dia ~100 μm was employed to stop stray portion of the X-ray beam and to pass X-rays only through the sample avoiding the SS gasket.

The details of the synchrotron beamline parameters, laboratory-based X-ray generator, and the high-pressure experimental procedure have been described in Chapter 2.

6.2.3 Techniques used for High-Pressure Experiment at High temperature

Helios membrane DAC (of M/s Almax easyLab, UK) has been used for generating high pressure and high temperature simultaneously. HP-HT XRD studies were carried out using a novel combination of membrane cell DAC coupled to a high flux micro-focus X-ray machine (of M/s XENOCS, France) [8]. Molybdenum target was used which results in X-ray of wavelength 0.711 Å. The details of the novel combination of *in-situ* HP-HT and the details of the novel experimental set up are described in Chapter 2 and 3.

HP-HT experiments were carried out on the compounds Sm_6UO_{12}, Gd_6UO_{12} and Dy_6UO_{12} up to a maximum pressure and temperature of (5.6 GPa, 673 K), (5.0 GPa, 673 K)

160

phase with rhombohedral structure. The lattice parameters were obtained by least square fitting of 2-theta reflections using NIST*AIDS-83 software. The analysis of the XRD pattern for RE_6UO_{12} results in the lattice parameters shown in table 6.1 and they are in agreement with the values quoted in the literature [6].

Table 6.1: *Lattice Parameters of various RE_6UO_{12} compounds studied in this thesis*

Compounds	Lattice Parameters
Sm_6UO_{12}	a=10.153 Å, c=9.625 Å
Gd_6UO_{12}	a=10.075 Å, c=9.534 Å
Dy_6UO_{12}	a=9.9806Å, c=9.4403 Å

6.2.2 Techniques used for High-Pressure Experiment at ambient temperature

High-pressure X-ray Diffraction (HP-XRD) experiments on the polycrystalline sample of RE_6UO_{12} (RE=Sm, Gd, Dy) were carried out using a Mao-Bell type Diamond Anvil Cell (DAC). Synchrotron X-ray source at Beamline-12, INDUS-2, RRCAT, Indore, was used for HP-XRD studies on RE_6UO_{12} (RE=Sm, Gd); whereas Beamline-11, at the same synchrotron, was used for HP-XRD study on Dy_6UO_{12}. The X-ray of wavelength 0.6071 Å was used to perform the high-pressure experiment on Sm_6UO_{12} and Gd_6UO_{12}. However, 0.6202 Å was selected for the HP-XRD of Dy_6UO_{12}.

Silver was used as the pressure calibrant as its peaks do not overlap with sample peaks. A mixture of Methanol: Ethanol: Water (MEW) in the ratio of 16:3:1 was used to obtain hydrostatic pressure environment inside the sample chamber of DAC. The compound was pressurized in steps to study the compressibility behavior at ambient temperature. XRD patterns were collected for 10 minutes, at each pressure, in angle

Chapter-6

Studies on Rare-Earth Uranates at HP & HP-HT

===

6.1 Introduction

Rare earth Uranates - RE_6UO_{12} type compounds - exist in the rhombohedral structure at ambient temperature. These compounds are studied for their importance in nuclear industry and from the fundamental physics point of view. As they show similarities with sesquioxides [1–3], therefore, interesting to study under High Pressure (HP) and High Pressure-High Temperature (HP-HT). In the present thesis, Chapter 4 and 5 dealt with the f-electron behavior in metallic and covalent bonded compounds, however, this chapter deals with the nature of 5-f electrons in ionic compounds such as rare-earth uranates. In this chapter three rare earth uranates, namely Sm_6UO_{12}, Gd_6UO_{12} and Dy_6UO_{12} have been chosen and studied under HP & HP-HT. These compounds are chosen so that it depicts the nature of rare-earth uranates as we move along the rare-earth series.

6.2 Experimental Methods

6.2.1 Sample Preparation and characterization

The sample was prepared using the urea–combustion method [4,5]. The details of the synthesis of these compounds are discussed in Chapter 2. X-ray diffraction (XRD) pattern was taken at ambient conditions using synchrotron X-ray source to affirm the phase formation. All the peaks in the diffraction pattern could be indexed to the rhombohedral structure with space group R-3 which confirms the formation of the compound in a single

see the movements of cation (RE^{3+}), but, oxygen (anions) atoms couldn't be refined, therefore, a study which can track oxygen atoms in the structure, is needed. Raman spectroscopy is an excellent tool to probe the bonding nature of light elements in the compound. The TEM observation of the recovered sample is required to realize the pressure induced amorphization on RE Uranates. Also, MEM analysis is needed for detailed discussion about the electronic structure.

analyzed structurally. Also, the origin of the low pressure phase transition in UOs_2 has to be probed, for which a computational DFT study can be carried out.

AlB_2 type compound UZr_2 shows a low bulk modulus, as expected, but does not show any phase transformation up to 20 GPa. As AlB_2 type UX_2 compounds are known for its phase transitions, the high pressure study can be extended to higher pressure. Furthermore, anomalies in the localization of the electrons, leading to the decrease in the metallization under pressure, have been found computationally, but, the result need to be confirmed experimentally for which high pressure resistivity experiments can be carried out. Another unexpected result in HP-HT study shows increase in the c/a ratio. The increase has been understood in term of the weakening of the U(1/3,2/3/1/2) and Zr(2/3,1/3/1/2) bonds. A confirmation for the probable weakening of the bonds is required through other experiments.

Isoelectronic UX_3 type compounds show dissimilar behavior in its compressibility because of increased hybridization. Therefore, more number of UX_3 compounds is to be studied to systemize the hybridization trend for other isoelectronic binary UX_3 compounds.

Rare-Earth Uranates are found to show very interesting results. Gadolium uranates show very sharp fall in the bulk modulus along the series. The reason for the decrease in the bulk modulus has been attributed to the localization of $4f$ electrons. Although localization of the $4f$ electrons are described in the literature due to half-filled $4f$ orbitals, a proof from computational details is absent. Therefore, computation effort is a requisite to establish the localization of the $4f$ electrons in the compound which lead to the subsequent weakening of the bonds, thereby, higher compressibility. Also, a disorder has been seen appearing in the structure under high pressure. A Rietveld refinement has been carried to

195

The disorder pressure in the system has correlation with the compressibility of the compound where disorder at lower pressure is seen in the high compressible compound. For the first-time pressure induced amorphization has been seen in the rare earth uranates and the reason was attributed to the possible anion disorder followed by cation disorder at high pressures.

High pressure studies at high temperatures reveal usual softening in the materials and they become more compressible at high temperature. Gd_6UO_{12} shows increased softening as compared to other uranates in the same temperature range. Also, it shows large volume thermal expansion coefficient at ambient pressure due to weaker bonding in the material resulting from localization of f-electrons in the compounds. Uranium is not found to play deciding role in the HP & HT properties of such ionic compounds.

7.2 Future Directions

The thesis studies the characteristics and the role of $5f$ electrons in uranium intermetallics & oxide compounds under extreme conditions. UX_2 type cubic compounds, UOs_2 and UIr_2, studied in the thesis show phase transitions to hexagonal and tetragonal phases, respectively, at different pressures but do not follow the structural sequence predicted either by the 2D structural maps or empirically structural sequence. Therefore to explore presence of systematics, the phase transition behavior of more number of binary uranium intermetallic compounds needs to be investigated.

UOs_2 & UIr_2 show phase transformation but the daughter phase structure could not be found out. Therefore, high pressure phase of both the compounds can be further

coefficient is observed with values of 4.6×10^{-5} K^{-1}, 3.7×10^{-5} K^{-1}, 2.7×10^{-5} K^{-1} at 1.2 GPa, 4.8 GPa and 6.6 GPa, respectively, for the temperature range of 300 K-473 K.

Despite being compounds of the same group the HP study on URh$_3$ and UIr$_3$ show abnormalities in their compressibility. Their bulk moduli are found to be widely varying, 133.0 GPa for URh$_3$ and 262.5 GPa for UIr$_3$, from each other. The reason for such a drastic increase in the bulk modulus can be attributed to the increased hybridization between uranium and iridium in UIr$_3$. The participation of the U-f states in the total density of states is found to be 61.3% more in UIr$_3$ at the Fermi level as compared to URh$_3$. Therefore, U-f states, rather than total DOS, are attributed to be responsible for such a large change in the compressibility of the compound.

Ionic compounds RE$_6$UO$_{12}$ (RE=Sm, Gd, Dy) have been studied under HP & HP-HT. The similarity, as expected, with the sesquioxide system are not observed under pressure in any of the rare earth uranates. Under Pressure, a-axis of the lattice is found to be more rigid as compared to c-axis because of the presence of corner sharing polyhedra along a-axis, in contrast to the temperature effect. A parabolic trend in the bulk modulus of the compounds Sm$_6$UO$_{12}$, Gd$_6$UO$_{12}$ and Dy$_6$UO$_{12}$ as a function of increasing atomic number of the rare-earth have been observed. An abrupt softening in Gd$_6$UO$_{12}$ is observed and can be ascribed to the localization of 4-f electrons of Gd. Further increase in the pressure results in setting up of disorder in the system. Rietveld refinement of the HP-XRD data reveals the origin of disorder could be oxygen anion. With increasing pressure, cations (RE^{3+}) also starts moving leading to increase in the (300) peak intensity and sharp decrease in the (211) and (122) intensity simultaneously. At very high pressures the compound is found to amorphize when both the anion and cation disorder take place simultaneously.

found to be 365.7 GPa which is the highest value known till now for UX_2 type compounds.

> HP-XRD studies on UIr_2 shows a phase transformation to a tetragonal lattice at 40 GPa. Computation reveals iridium tetrahedral network in the lattice to be more stable due to its shorter Ir-Ir bonding. However, U-Ir has metallic & covalent nature of bonding. The covalent nature is found to increase with pressure, thereby, strengthening the U-Ir bonds. Therefore, application of pressure directly affects uranium tetrahedra, resulting in the distortions in uranium tetrahedra and hence responsible for the observed phase transition. Total density of state plot also shows a dip at Fermi energy. Origin of pseudo gap in the calculated DOS indicates new structure to be more favorable and stable at higher pressures.

HP-XRD studies of UX_2 type compound with AlB_2 type structure i.e. UZr_2, show a different trend in bulk modulus as compared to the $MgCu_2$ type UX_2 structures. The material was found to be highly compressible, with a bulk modulus of 108.3 GPa. Different rates of contraction in c/a axial ratio in the unit cell of the compound has been observed as a function of pressure and it is attributed to the strengthening of U(1/3,2/3,1/2) & Zr(2/3,1/3,1/2) covalent bond along the 'a' axis at higher pressures. Also, the localization of charge density leads to the drop in the metallization of the material which can be clearly seen from the charge density plots. HP-HT study shows increase in c/a ratio as a function of pressure at higher temperatures. It is understood in terms of weakening of U(1/3,2/3,1/2) & Zr(2/3,1/3,1/2) bond at high temperatures. Softening in the material at higher temperatures and a pressure dependent decrease in the volume thermal expansion

at low power (50 W), aids to very good resolution X-ray diffraction pattern in HP-HT environment.

➢ A micro-heater for Helios membrane cell DAC has been designed & developed to carry out resistive heating around the sample area inside DAC. The indigenous micro heater have been tested inside the DAC. Higher values of temperatures from the fabricated heater were obtained as compared to the imported heater for the same current. It is an indicative of the better performance of the indigenous heater as higher current values lead to the melting of the coils and contacts.

7.1.2 Research Work

The motto of the thesis is to study the role of uranium's $5f$-electrons in deciding the stability of uranium compounds at high pressures and temperatures. Towards this aim, uranium intermetallic (UX_2 & UX_3) compounds with covalent & metallic nature of bonding and rare-earth uranates with ionic character have been studied in this thesis.

Uranium intermetallic compounds having $MgCu_2$ type structure: UOs_2 and UIr_2 have been studied under high pressure up to 35.5 GPa and 55.0 GPa resulting in the bulk moduli to be 261.0 GPa and 284.0 GPa at ambient pressure, respectively. These values indicate lesser compressibility of $MgCu_2$ type compounds. In spite of similar bulk moduli their physical properties are found to be much different at higher pressures which are described below-

➢ HP-XRD studies on UOs_2 shows a phase transformation at very low pressures i.e. 12 GPa to a hexagonal lattice. Bulk modulus of the high pressure phase has been

Chapter 7

Summary and Future Directions

7.1 Summary

7.1.1 Developmental Work

Some of the novel tools and techniques, useful for high pressure and high temperature experiments, have been developed in the laboratory during the period of the thesis. A brief description of the developed tool and techniques are given below:

- ➤ A Micro-Electric Discharge machine (micro-EDM) has been developed to drill holes of size varying from ~70 μm to ~300 μm in the gasket which is being used in Mao-Bell type Diamond Anvil Cell for high pressure experiments.

- ➤ Using the above mentioned micro-EDM a novel experiment has been carried out to perform LHDAC or optical spectroscopy experiment. This method is useful when pressure calibrant and sample reacts at high temperatures. It is also useful when spectra of pressure calibrant and sample overlaps each other. This technique facilitates a physical separation of pressure calibrant from the actual sample under study, thereby, avoiding any possibility of reaction or overlap of spectra.

- ➤ A novel combination of micro-focus high flux X-ray generator and Helios membrane cell DAC has been set up in the laboratory to perform High Pressure and High Temperature (HP-HT) experiment. The high flux and micro-focus X-ray,